

Evaluation of bacterial adhesion on carbon nanotube-poly(dimethylsiloxane) composite materials

Márcia Raquel da Silva e Sousa Vagos



U.PORTO
FEUP FACULDADE DE ENGENHARIA
UNIVERSIDADE DO PORTO

Mestrado Integrado em Bioengenharia

Supervisor: Prof. Filipe Mergulhão

Second Supervisor: Prof. Fernando Pereira

June 28, 2013

Evaluation of bacterial adhesion on carbon nanotube-poly(dimethylsiloxane) composite materials

Márcia Raquel da Silva e Sousa Vagos

Mestrado Integrado em Bioengenharia

Approved in oral examination by the committee:

Chair: Professor Artur Cardoso

External Examiner: Professor Cristina Freire

Supervisor: Professor Filipe Mergulhão

Abstract

The present work was focused on the evaluation of the effect of carbon nanotubes (CNTs) on the surface properties of carbon nanotube/poly(dimethylsiloxane) (CNT/PDMS) composite materials and on the initial bacterial adhesion.

In order to evaluate the effect of CNT structure and surface chemistry on its interaction and dispersion within the polymer matrix as well as their influence on the composite properties, different types of CNTs were used. Commercially available pristine CNTs (p-CNTs) were functionalized (f-CNTs) with a well-established oxidation treatment using nitric acid to introduce acidic groups at the surface. Then, these modified CNTs were subjected to heat treatments at three different temperatures, 400, 600 and 900 °C to selectively remove their functional groups and therefore obtain CNTs with controlled surface chemistry. For structural modification, the CNTs were mechanically ground using a ball milling machine(p-CNT-BM and f-CNT-BM). Thus, CNT/PDMS composites with different surface and bulk were produced. Besides, three different compounding methods were tested: bulk mixing in PDMS, solution mixing with dispersion agent and double-layer deposition. Composites produced by the bulk mixing process contained three different CNT loadings, 0.1, 0.5 and 1 wt%, and thin films were fabricated using the spin coating technique. With the solution mixing process CNT in 1 wt% loading were dispersed in tetrahydrofuran (THF) and the solution was mixed with PDMS. These coatings were deposited through manual spreading. The double-layer composites were produced by first depositing a thin film of dispersed CNTs and spin coating this film with a layer of PDMS. The various CNT samples produced were characterized by N₂ adsorption isotherms and Temperature programmed desorption (TPD). The composite materials were also characterized with contact angle (CA) measurements, Thermogravimetry, (TG)Scanning Electron Microscopy (SEM), X-ray Photoelectron Spectroscopy (XPS), Atomic Force Microscopy (AFM), Fourier Transform Infrared Spectroscopy (FTIR) and direct-current (DC) conductivity tests. Additionally, degradation assays in liquid media were also performed to evaluate chemical stability. The adhesion assays were conducted using a parallel-plate flow chamber in steady state flow with a shear stress of 0.01 Pa to simulate the conditions found in the urinary tract of the human body. *Escherichia coli* (*E. coli*) was used as model since it is a well-studied bacteria with a dominant presence in the human body and is the cause of many implant-related infections. The various surfaces were compared in terms of surface hydrophobicity and number of cells adhered after a 30 minute adhesion assay.

The results showed that there was an increase in thermal stability in the composites produced by bulk and solution mixing and that the coatings fabricated by solution mixing and double-layer deposition also showed an enhancement in electrical conductivity. Besides, all the produced surface showed hydrophobic character, with small differences in hydrophobicity. There was also a slight difference in cell adhesion on the various composites with different surface properties, although not statistically significant (one-way ANOVA, p>0.05), with an overall reduction in cell adhesion compared to PDMS (the control). There also seemed to be a tendency of p-CNTs to result in less cell adhesion than f-CNTs. Besides, some of the surfaces presented different rough-

ness which may possibly have had an effect on *E. coli* adhesion. The composites produced with dispersion of nanotubes in THF showed similar adhesion tendency.

This work provided an encouraging insight into the possibility of using CNTs to produce functional PDMS composites with enhanced thermal, electrical properties and suggested they may have a cell adhesive response, which could have important applications in the future.

Summary

Carbon nanotube (CNT) composite materials are rapidly becoming one the major focuses of current investigation on nanostructured materials due to their unique properties which allow them to find numerous applications in various fields of science and technology.

In the biomedical field, CNT composites have been widely studied and utilized to obtain materials with exceptional mechanical, electrical, thermal, chemical and structural properties. Most remarkably, these nano-composites have been utilized in biosensors, scaffolds for tissue engineering, bone grafts and cement, cardiac patches, cartilage, electrodes, stent coatings and artificial muscle.

Poly(dimethylsiloxane) (PDMS) has been the most widely used polymeric material the biomedical industry over the past decades. It has been employed in a variety of different medical devices, including catheters, artificial heart, tubes and drains, cardiac valves, sensors, intra-ocular and contact lenses, aesthetic implants, soft tissue expanders, finger joint implants among many others. It is a silicon-based elastomeric polymer with an attractive set of properties which make it such an interesting material for medical applications. It is inert, biocompatible, flexible, optically transparent, mechanically compliant and easily processable into a variety of materials. The preparation and characterization CNT/PDMS composites is well-described in the literature and there has been report of the remarkable improvements in mechanical strength, electrical conductivity and thermal stability achieved with the incorporation of CNTs in PDMS as nano-fillers.

In addition to the possibility of fabricating biomaterials with enhanced bulk properties, several studies have demonstrated the ability of these novel CNT composites to have a bioactive and cell-modulating response at the interface level. This fact has an immediate implication in the way biomaterials are designed since it brings new possibilities of combining their biological effect with high-performance materials. Examples of such applications would be materials with tunable surface hydrophobicity and nano-structure to provide implants with conductivity, anti-fouling properties or else to promote cell adhesion and proliferation for transplantation in tissue engineering applications.

In the present work, CNT/PDMS composite materials were prepared and characterized by various techniques. To prepare the composite materials, samples of CNTs were incorporated in the PDMS matrix. Since a good dispersion of the CNTs in the polymer is essential for an effective CNT-polymer bonding and is thus the major factor influencing the properties of the final composite, three different preparation methods were : bulk mixing, solution mixing and double-layer deposition. The bulk mixing method consisted in a combination of shear mixing, sonication and ultrasound assisted dispersion to improve the separation of the CNT aggregates directly in the PDMS matrix and to promote a uniform distribution. This method, however, has the drawback of causing damage and shortening of the nanotubes. Different types of CNTs were used: pristine CNTs (p-CNT), functionalized CNTs (f-CNT), oxidized with nitric acid, at 0.1, 0.5 1 wt%; as well as p-CNTs and f-CNTs mechanically ground in a ball millikng machine (p-CNT-BM and f-CNT-BM) at 1 wt%. These composite materials were then deposited as thin films on glass substrates by

spin coating.

A solution mixing method was also used, whereby an effective dispersion was achieved using only high-shear mixing of a CNT suspension in tetrahydrofuran (THF), a commonly used organic solvent, yielding the p-CNT-THF and f-CNT-THF samples. This way, the nanotubes were dispersed in a liquid phase with much lower viscosity than PDMS without the need for using ultrasound treatment. This method, however, has the disadvantage of employing a solvent to disperse the CNTs. This solution was then mixed with PDMS and the as-produced composites were deposited on glass substrates by manually spreading them until a uniform layer was obtained.

In order to produce materials with enhanced conductive properties, double-layer composite coatings were also fabricated. In this method, CNTs were first dispersed in a liquid phase using two different test solvents, sodium dodecylsulfate (SDS), a commonly used surfactant, and THF (samples p-CNT/f-CNT in SDS and p-CNT/f-CNT in THF). Then small volumes of the as-produced suspension were deposited on top of glass slides and left to evaporate. When all the solvent had dried out, a thin film of CNTs was formed on the substrate. The PDMS was then infiltrated into the CNT layer by spin coating.

The materials were characterized through contact angle (CA) measurements, which permitted to make a quantitative assessment of the surface hydrophobicity, as well as degradation assays in static (with citrate buffer and synthetic urine) and steady-state flow conditions (citrate buffer). X-Ray Photoelectron Spectroscopy (XPS) was done to obtain a chemical characterization of the composite coatings and Scanning Electron Microscopy (SEM) allowed for a morphological inspection. Fourier Transform Infrared (FTIR) was also used to analyse the chemical bonds present on the outermost layer of the composite material and therefore assess whether chemical bonding between nanotubes and polymer was observed. CNTs were directly characterized with N₂ adsorption isotherms to evaluate the textural properties of the various CNT samples and Temperature Programmed Desorption (TPD) to evaluate their surface chemistry. Thermogravimetric analysis (TG) was employed to evaluate the effect of the incorporation of CNTs in the thermal stability of PDMS. Finally, direct-current (DC) measurements were also performed to provide an electrical characterization of the developed materials.

Initial cell adhesion assays were performed using a parallel-plate flow chamber in steady state flow with a shear stress of 0.01 Pa to simulate the shear stress conditions observed in the urinary tract of the human body. Two types of adhesion assays were done, on-line and end-point assays, depending on the optical transparency of the coatings and with a duration of 30 minutes. Composites with 0.1 wt% CNT loading were sufficiently transparent for light transmittance microscopy, so they were tested with on-line cell adhesion assays. But the ones at 1 wt% CNT loading were not sufficiently transparent, so DAPI staining after a 30 minute run was used instead. Microscopy images were taken to perform cell countings and compare the number of cells adhered after 30 minutes exposure to the cell flux. Two different controls with PDMS were done for each type of assay.

The results were analysed and compared throughout the samples to seek a relation between the surface properties of the tested samples and the cell adhesion observed.

The results showed that the dispersion of CNTs with the bulk mixing method was only possible with mechanical treatment of the nanotubes and aggressive sonication. Microscopy and SEM images showed that even after that CNT aggregates still remained in the bulk of the composites, but with much smaller dimensions.

TG analysis showed an enhancement of the thermal stability of the composites comparing to pure PDMS, suggesting that effective bondings between CNTs and polymer chains were established, but the strength of these bonds depended also on the functionalization of the nanotubes.

TPD analysis revealed that the CNTs were successfully functionalized and that different acidic groups were introduced on the surface, which could be observed from the selective and progressive removal of CO and CO₂ content in the different samples. N₂ adsorption isotherms indicated that structural changes were induced by the nitric acidtion, heat and ball milling treatments from the increased surface areas of the nanotubes when compared to the pristine ones.

Contact angle measurements of the composites suggested that the introduction of CNTs in the polymer matrix had a slight effect on its surface hydrophobicity. All composite surfaces, except the PDMS/f-CNT 1%, showed a theoretical decrease in the adhesion energy with *E. coli* compared to PDMS, meaning that adhesion is more favourable in the composite surfaces.

The bacterial adhesion assays revealed that there was a statistical difference between the coatings containing 0.1 and more than 0.5 wt% of CNTs, with the former not being significantly different from the control, PDMS. Regarding the coatings containing more than 0.5 wt% of CNTs, there were no statistical differences between the various surfaces in terms of cell adhesion. However, it could be observed that there was a slight tendency of f-CNTs inducing more adhesion than p-CNTs, which could not be entirely explained in terms of surface hydrophobicity. Surprisingly, there was slightly less cell adhesion when the CNT loading was increased from 0.1 to 1 wt%. This may have been partially caused by the increased surface roughness induced by re-aggregation of the CNTs during the spin coating, even though the CA measurements did not show a significant difference in surface hydrophobicity. The samples with CNT-BM showed levels of cell adhesion more similar to of the 0.1 wt% samples. Since all these samples had similar surface morphologies (yet different from the PDMS/p-CNT 1% and PDMS/f-CNT 1 % surfaces), this seems to again suggest that the surface roughness, and having nanotubes closer to the surface, also has an effect on cell adhesion.

The PDMS/p-CNT-THF and PDMS/f-CNT-THF at 1 wt% surfaces also showed the same tendency of decreased cell adhesion with p-CNTs and otherwise with f-CNTs, but the difference between both were slightly more accentuated. Note that the fact that CNTs were better dispersed in these samples may have caused any possible effects induced by the direct contact of nanotubes with the cells to become more dominant. However, it has been suggested in other works that p-CNTs may be more adherent to bacteria then f-CNTs.

It is important to realise that when it comes to adhesion with biological systems there are many parameters to be considered and most adhesion theories fail to provide accurate predicts due to the complexity of the biological models used.

Morphological and chemical analysis of the composites with SEM, XPS and FTIR showe dthat CNTs were not visible on at the surface, with exception of some aggregates where some nanotubes sprouting out could be visible. So, these analyses suggested that there was a tendency for CNTs to be deposited at the bottom of the substrate rather than evenly distributed throughout the height of the coatings. This observation may indicate that the spin coating procedure used is not well suitable for preparing composite coatings where it is desirable to have the CNTs at the surface. These results also provided an explanation for why no major differences in surface hydrophobicity and cell adhesion were obtained with the introduction of both the p-CNTs and f-CNTs a 0.1, 0.5 and 1 wt%.

Electrical conductivity measurements showed that the composite coatings produced by the bulk mixing process with 0.1 wt% or 1 wt% of CNTs was not sufficient to increase its electrical conductivity. This results could be explained from the microscopy and SEM observations where it could be seen that the CNTs were still considerably bundled in small clusters and these aggregates were too separated to establish a percolative path across the matrix. However, the PDMS/p-CNT-THF and PDMS/f-CNT-THF samples showed a 7- and 5-fold increase in electrical conductance,

respectively, suggested that a better dispersion of the nanotubes had been achieved with the solution mixing process. The double-layer composite coatings, in turn, showed a remarkable increase in electrical conductance, reaching increases of 9 and 8 orders of magnitude for the ones produced with SDS and THF, respectively. This may suggest that the nanotubes were better dispersed in SDS than in THF. So, the composite coatings produced by the double-layer deposition method showed the greatest promise for electronic applications. This is not surprising since the bottom layer of the coating consisted of a mat of uniformly distributed CNTs with higher surface density. It was also noted that the values of conductance measured were dependent on the insulating PDMS layer which impeded an effective electrical contact between CNTs and measurement equipment.

The degradation assays suggested that the composite coatings remained stable when in contact with a citrate buffer solution both in static and steady-state flow conditions. The results of the degradation assay with synthetic urine showed a well-defined peak in the UV range, so further tests should be conducted to clarify this point.

In summary, this work allowed to conclude that there seems to be an effect in both the bulk and surface properties of PDMS with the introduction of CNTs.

There was a statistical difference in cell adhesion obtained with the composite coatings at 0.1 and >0.5 wt%, but these also corresponded to the two different adhesion assays. In general, the composite coatings showed less bacterial adhesion than the control, PDMS, and despite not statistically meaningful, there seemed to be a tendency of coatings with p-CNTs having less adhesion than the ones with f-CNTs. Besides, although further investigation would be necessary to obtain more conclusive results, it may be possible that other factors such as surface roughness and CNT dispersion inside the PDMS also have an influence in modulating adhesion of *E. coli*, as could be seen from the slight differences in the results. So, there is indication that the surface properties of the CNT/PDMS coatings may be tuned to yield an effect on bacterial adhesion depending on the desired application. Plus, the enhanced electrical behaviour of some of the composites may find interesting applications in the future in the implant industry once the biological interactions with these surfaces are fully understood.

Acknowledgements

My sincere acknowledgements to my supervisors, Professors Filipe Mergulhão and Fernando Pereira, for their constant support in the development of this work and for the motivation they gave me to keep exploring new possibilities and for setting the goals I sought to accomplish.

I would like to thank Joana Moreira, whose contribution, patience and support were so important for the realization and accomplishments achieved in this work and for keeping me focused all the way.

Thanks to all the researchers and colleagues of the Laboratory of Catalysis and Materials and of the Laboratory for Process, Environmental and Energy Engineering, where I developed all my work, for their constant help with the equipments and their availability whenever needed. A special thanks to Salomé Soares for all her support and important suggestions. I am also grateful to Jeyaraj Ponmozhi for her help and for providing me with materials needed for this work.

I would also like to kindly thank Professor Luís Melo for introducing me to these two research groups and helping me in a difficult time. Without him I would not had the chance to be part of this research.

Thanks to Professor Inácio Martins for his help and interest in my work.

Thanks also to Centi, especially to Dr. Carla Silva for allowing me to use their facilities to conduct analysis and José Fernando Silva for his kind help.

Márcia Raquel da Silva e Sousa Vagos

*“No man ever steps in the same river twice,
for it’s not the same river and he’s not the same man.”*

Heraclitus

Contents

1	Introduction	1
1.1	Context	1
1.2	Motivation and Objectives	1
1.3	Structure of the Dissertation	3
2	Carbon nanotube-based materials and their applications	5
2.1	Introduction	5
2.2	Carbon Nanotubes	6
2.2.1	Properties of Carbon Nanotubes	6
2.2.2	Biocompatibility and Bioactivity of carbon nanotubes	8
2.3	Poly(dimethyl siloxane) (PDMS)	9
2.4	Carbon Nanotube composites	11
2.4.1	Dispersion methods	13
2.4.2	Chemical functionalization of carbon nanotubes	14
2.4.3	Conductive behaviour of CNT-polymer composites	15
2.5	Biomedical Applications of Carbon Nanotube Composites	17
3	Bacterial adhesion on surfaces and their interaction with carbon nanotubes	19
3.1	Interactions between carbon nanotubes and bacterial cells	19
3.2	Adhesion on surfaces	21
3.3	Antifouling Surfaces	25
3.4	Parallel Plate Flow Chamber Bacterial Adhesion Assay	26
4	Materials and Methods	29
4.1	Chemical and Mechanical treatment of the MWCNTs	30
4.2	Preparation of CNT/PDMS composite coatings	31
4.2.1	Bulk Mixing	31
4.2.2	Solution Mixing with a Solvent	32
4.2.3	CNT-PDMS double-layer composites	32
4.3	Characterization Techniques	33
4.3.1	N ₂ Adsorption Isotherms	33
4.3.2	Thermogravimetric analysis	34
4.3.3	Temperature Programmed Desorption (TPD)	35
4.3.4	Contact Angle Measurements	35
4.3.5	Degradation Assay	35
4.3.6	Surface Analysis	35
4.3.7	Conductivity Measurements	36
4.4	Cell Adhesion Assay	37

CONTENTS

4.4.1	Cell Cultivation and harvesting	37
4.4.2	Parallel Plate Flow Chamber assay	37
4.4.3	On-line Cell Adhesion Assay	38
4.4.4	End-point Cell Adhesion Assay with DAPI staining	38
4.4.5	Image Analysis	39
5	Results and Discussion	45
5.1	Composite Coatings	45
5.1.1	Bulk mixing	45
5.1.2	Solution-mixing	46
5.1.3	Double layer coatings	46
5.2	Characterization Techniques	47
5.2.1	N ₂ Adsorption Isotherms	47
5.2.2	Thermogravimetric Analysis	48
5.2.3	Temperature Programmed Desorption	51
5.2.4	Fourier Transform Infrared Spectroscopy (FTIR)	53
5.2.5	Contact Angle Measurements	54
5.2.6	UV-Vis Spectroscopy	55
5.2.7	X-Ray Photoelectron Microscopy (XPS)	57
5.2.8	Scanning Electron Microscopy (SEM)	58
5.2.9	Atomic Force Microscopy (AFM)	62
5.2.10	Conductivity Measurements	62
5.3	Bacterial Adhesion	66
5.3.1	Kinetic Cell Countings	66
5.3.2	End-point Cell Countings with DAPI staining	68
6	Conclusions and Future Work	73
A	Experimental Set-up	79
B	Cell Adhesion Assay	81
B.1	Kinetic Adhesion Curves	82
B.2	Microscopy images	82
B.2.1	Optical Microscopy	83
B.2.2	Fluorescence Microscopy	83
C	CNT/PDMS composite coatings	85
D	Adhesion Energy Calculations	89
E	Spin Coating Theory	91
F	Theory of Temperature Programmed Desorption	97
References		101

List of Figures

2.1	Carbon nanotubes: a. single-walled carbon nanotubes (SWCNT) b. multi-walled carbon nanotubes (MWCNT) Reprinted from [1].	7
2.2	Schematic representation of a graphite sheet rolled to form a nanotube and its chiral vector. Reprinted from [2].	8
2.3	(a) Scanning Electron Microscopy (SEM) of SWCNTs showing a mat of entangled carbon fibers of 10 to 20 nm in diameter and several micrometers in length. Scale bar, 100 nm; (b) A single SWCNT rope with 100 nanotubes as it bends through the image plane of the microscope, showing uniform diameters and and triangular-patterned packing of the SWCNTs inside the rope. Scale bar, 10 nm; (c) Transmission Eelectron Microscopy (TEM) image of the side view of a rope segment. Scale bar, 20 nm. Reprinted from [3].	9
2.4	Chemical structure of poly(dimethylsiloxane). Reprinted from [4]	11
3.1	CNT nanocomposites activity in biofouling release (left) and biofilm promotion (right) applications in various stage of biofilm growth. Reprinted from [5].	20
3.2	Schematic example of the measurement of the angle between a liquid drop and a circular contact area on a planar solid surface. Reprinted from [6]	22
3.3	A flow chamber example and its velocity and shear stress profile in arbitrary units. (a) Diagram of a parallel-plate flow chamber of width b , height h , and length L , in its orientation in the x-y-z axes. The fluid is forced through the chamber by a steady pressure gradient along the x-axis. (b) and (c) show the calculated velocity profile u and the shear stress profile t , respectively, for an aspect ratio b/h of 80: The arrows indicate that the profiles were taken very near the right edge of the flow chamber. The shear stress has its maximum value at the plate surfaces and vanishes at the chamber corners. Parabolic velocity profile and homogeneous wall shear stress are characteristic for steady flow between parallel plates. Reprinted from [7].	27
4.1	Process Flow diagram of the procedures used for preparing the various CNT samples.	31
4.2	Process Flow Diagram of the set-up used for the on-line <i>E. coli</i> adhesion assays, drawn with Microsoft Visio® Software. The blue arrows indicate flow direction in the tubes.	39
4.3	Process Flow Diagram of the set-up used for the end-point <i>E. coli</i> adhesion assays, drawn with Microsoft Visio® Software. The blue arrows indicate flow direction in the tubes.	40
4.4	Process Flow Diagram of the set-up used for the end-point <i>E. coli</i> adhesion assays, drawn with Microsoft Visio® Software. The blue arrows indicate flow direction in the tubes.	43

LIST OF FIGURES

5.1	N ₂ Adsorption isotherms of the pristine CNTs (p-CNTs) and the CNTs prepared with the acid functionalization (f-CNT), heat treatment (f-CNT-400, f-CNT-600 and f-CNT-900) and ball milling (BM) treatment.	48
5.2	Thermogravimetric spectra of the: (a) pristine CNTs (p-CNT) and functionalized CNTs (HNO ₃ – CNT) samples; (b) PDMS, PDMS/p-CNT 0.1 wt%, PDMS/p-CNT 1 wt%, PDMS/p-CNT-BM 1 wt%, PDMS/f-CNT-BM 1 wt% and PDMS/p-CNT-THF 1 wt% samples.	50
5.3	Thermogravimetric spectra of the derivative of the PDMS, PDMS/p-CNT 0.1 wt%, PDMS/p-CNT 1 wt%, PDMS/p-CNT-BM 1 wt%, PDMS/f-CNT-BM 1 wt% and PDMS/p-CNT-THF 1 wt% samples.	50
5.4	TPD results: (a) CO and (b) CO ₂ spectra of the p-CNT, f-CNT, f-CNT-400, f-CNT-600, f-CNT-900 and p-CNT-BM samples.	51
5.5	(a) ATR-FTIR spectrum of PDMS, PDMS/p-CNT and PDMS/f-CNT composite membranes, taken between 650 and 4000 nm; (b) High resolution ATR-FTIR spectra of PDS, PDMS/p-CNT and PDMS/f-CNT composite membranes, between 650 and 950 nm.	53
5.6	Surface free energy and adhesion energy of: 1 - PDMS; 2 - PDMS/p-CNT 0.1%; 3 - PDMS/p-CNT 0.1%; 4 - PDMS/p-CNT 0.1%; 5 - PDMS/p-CNT 1%; 6 - PDMS/f-CNT 1%; 7 - PDMS/p-CNT-BM 1%; 8 - PDMS/f-CNT-BM 1%; 9 - PDMS/p-CNT-THF 1%; 10 - PDMS/f-CNT-THF 1%. Values of adhesion energy were divided by a factor of 10 for better visualization.	55
5.7	UV-Vis spectra of the citrate buffer solution (left side) and synthetic urine (right side) after 1, 4 and 8 days of immersion with the PDMS, PDMS/p-CNT 0.1% and PDMS/p-CNT 0.1% samples.	57
5.8	SEM images of the surfaces of the PDMS/p-CNT 1 wt%, (a) and (b); PDMS/p-CNT 0.1 wt%, (c); PDMS/f-CNT 1 wt%, (d); and (e) PDMS/f-CNT-BM 1 wt%, (e) and (f), coatings.	60
5.9	SEM images of the PDMS (a) and PDMS/p-CNT-BM 1% (b) cross-sections; PDMS/p-CNT in SDS (c) and PDMS/f-CNT (d) to (f) in SDS surfaces of the coatings (magnification, 2000x; scale).	61
5.10	Mean values of thickness of each sample thickness determined from SEM images represented in table (a) and bar chart (b) form.	62
5.12	(a) Conductance curves of the glass, PDMS, PDMS/p-CNT 0.1%, PDMS/f-CNT 0.1%, PDMS/p-CNT 1%, PDMS/f-CNT 1%, PDMS/p-CNT-BM 1% and PDMS/p-CNT-BM 1% samples measured from -100 Volt to +100 Volt; (b) (a) Conductance curves of the CNT-SDS, f-CNT-SDS, CNT-THF, f-CNT-THF samples measured from -1 Volt to +1 Volt. Values are in Siemans.	63
5.11	AFM images of the PDMS/p-CNT 1% ((a) to (c)) and PDMS/f-CNT 1% ((d) to (f)) coatings showing three different zones with distinct roughness.	65
5.13	Bar chart of the average cell densities in the PDMS (black bar), PDMS/p-CNT 0.1% (blue bar) and PDMS/p-CNT 0.1% (red bar) coatings, obtained with three independent tests. Error bars correspond to standard deviation.	66
5.14	Graphic of mean cell adhesion kinetic curves in the three samples: PDMS, p-CNT/PMDS 0.1% and f-CNT/PMDS 0.1%.	67
5.15	Bar graph of end-point cell adhesion countings of the various surfaces containing pristine CNTs (p-CNT, blue bars) and functionalized CNTs (f-CNT, red bars) at 0.5 and 1 wt% with or without ball milling treatments (BM) or dispersed with THF.	69

LIST OF FIGURES

5.16	Relative adhesion (RA) values for pristine CNTs (p-CNT, blue bars) and functionalized CNTs (f-CNT, red bars) at 0.1 and 1 wt% with or without ball milling treatments (BM) and for p-CNT at 0.5 wt% (green bar). The table on the right side indicates the surfaces corresponding to each numerical label on the bar chart. All surfaces were produced by the bulk mixing method except those produced with solution mixing (CNT/THF). Values were calculated by dividing cell countings obtained for a certain surface by those obtained with PDMS (control). Letters A and B indicate groups of mean values with statistically different RA (one-way ANOVA test, $p>0.05$).	71
A.1	Photographs of the experimental set-up.	79
B.1	kinetic adhesion curves obtained with the on-line adhesion assays.	82
B.2	Microscopy images of the various composite coating surfaces with adhered <i>E. Coli</i> after a 30 minute on-line adhesion assay visualized at the optical microscope (Nikon eclipse V100; magnification, 10x). These images were used for off-line image analysis to determine the number of cells adhered at each surface.	83
B.3	Fluorescence microscopy images with DAPI staining of the PDMS/p-CNT/THF composite coating surface with adhered <i>E. coli</i> after a 30 minute adhesion assay (magnification, 10x).	84
C.1	Photographs of the PDMS/p-CNT 0.1 wt% composite in three different processing stages.	86
C.2	Microscopy image of the various composite coatings in a bulk focal plane (magnification, 10x).	87
E.1	Graphical representation of the dependence of the final film thickness on three pin coating parameters: spin speed, spin time and exhaust volume and of the film uniformity on exhaust volume. Reprinted from [Spin coat theory].	93
E.2	Schematic representation of some of the issues commonly found in spin coating: (a) bubbles entrapped inside the film; (b) comets caused by particles and impurities deposited on the surface; (c) central circle result form an accumulation of non-dispersed mass; (d) uncoated areas resulting from insufficient dispensed mass or high viscosity. Reprinted from [Spin coat theory].	94

LIST OF FIGURES

List of Tables

4.1	List of the different carbon nanotube samples prepared and the methods used.	31
4.2	List of the different types of composites produced through the evaporation/infiltration method. All spin coating parameters were fixed (200 rpm/sec, 60 seconds) and the spin speed (ω_S) was varied between 2000 rpm and 5000 rpm.	33
5.1	List of the different types of composites produced through the evaporation/infiltration method. All spin coating parameters were fixed (200 rpms^{-1} , 60 seconds) and the spin speed was varied between 2000 and 5000 rpm.	47
5.2	S_{BET} determined from N_2 adsorption isotherm analysis of the samples ($\pm 10^\circ\text{C}$).	48
5.3	Total percentage mass loss of the samples obtained as the final mass loss divided by the initial mass.	50
5.4	Results of the TPD analysis of the f-CNT, f-CNT-400, f-CNT-600 and f-CNT-900 samples.	51
5.5	List of the functional groups released from the oxidized CNTs and the temperature range at which they typically decompose. Values adapted from [8].	51
5.6	Surface free energy and energy of adhesion with <i>E. coli</i> cell of each surface tested, calculated as described in chapter 3.	55
5.7	Elemental atomic percentages (At%) of carbon, oxygen and nitrogen at the surface of the coatings.	58
5.8	DC characteristic curves os the different composite coatings measured in a specified voltage interval (-1 to 1 Volt or -100 to 100 Volt).	63
5.9	Values of cell densities calculated from the previous Table and normalized to an area of approximately $4.9 \cdot 10^5 \mu\text{m}^2$ and respective Adhesion rates. Values are in cells $\mu\text{m}^2 \cdot 10^{-5}$ and in $\mu\text{m}^2 \cdot \text{min}^{-1} 10^{-5}$, respectively.	66
5.10	Cell densities of the end-point adhesion assays of the p-CNT/PDMS 1%, f-CNT/PDMS 1%, p-CNT/PDMS 0.5%, p-BM/PDMS 1% and f-CNT-BM/PDMS 1% coatings with DAPI staining. The results were obtained for two independent tests, Test 1 and Test 2. Values correspond to mean \pm standard deviation of the total cell counting divided by the area of the field of view, $4.7 \cdot 10^3 \mu\text{m}^2$. Values are in cells $\mu\text{m}^{-2} \cdot 10^{-4}$	69
D.1	Contact angles measurements of the different coatings (mean value \pm std error).	89
D.2	Surface tension of the liquids used for the CA measurements [9].	90
D.3	Calculations of surface energies of <i>E. Coli</i> in the various coating surfaces (0.1% wt of CNT).	90
D.4	Adhesion Energy of the various coatings with <i>E. coli</i>	90

LIST OF TABLES

Abbreviations

AFM	Atomic Force Microscopy
BM	Ball Milling
CA	Contact Angle
CNT	Carbon Nanotube
CSH	Cell Surface Hydrophobicity
CVD	Chemical Vapour Deposition
DAPI	4',6-diamidino-2-phenylindole
E. Coli	<i>Escherichia Coli</i>
f-CNT	Functionalized Carbon Nanotube
FTIR	Fourier Transform Infrared Spectroscopy
HNO ₃	Nitric Acid
p-CNT	Pristine Carbon Nanotube
PDMS	Poly(dimethylsiloxane)
ROI	Region of Interest
rpm	Rotations per minute
RT	Room Temperature
SDS	Sodium Dodecyl Sulfate
SEM	Scanning Electron Microscopy
TG	Thermogravimetry
TPD	Temperature Programmed Desorption
UV-Vis	Ultraviolet-Visible Absorption Spectroscopy
XPS	X-Ray Spectroscopy
γ^{AB}	Surface Tension due to acid-base interactions
γ^+	Surface Tension due to attractive charges
γ^-	Surface Tension due to repulsive charges
γ^{LW}	Surface Tension due to van der Waals forces
γ^{tot}	Total Surface Tension
ΔG_{AB}	Free Gibbs energy of Adhesion due to acid-base interactions
ΔG_{LW}	Free Gibbs energy of Adhesion due to van der Waals forces
$\Delta G_{adhesion}$	Total Free Gibbs energy of Adhesion

Chapter 1

Introduction

1.1 Context

The twenty-first century has seen a boom in the research for materials with novel functionalities and applications in the biomedical industry. This recent area of research has shown an exciting promise for the production of biomaterials capable of performing nano-scale functions, such as biosensing, tissue regeneration and smart implants. This enables the development of a more targeted and less invasive medical treatment as healthcare is becoming ever more demanding and application-specific. With the development of nanotechnology and its applications it has been possible to create novel nano-engineered materials that could have a huge impact in medicine and in the way implants are designed to interact with and operate inside the patient's body.

1.2 Motivation and Objectives

The main goals of this dissertation were to evaluate the influence of the incorporation of carbon nanotubes (CNT) in poly(dimethylsiloxane) (PDMS) matrices on the surface chemistry and hydrophobicity of the resulting composite materials as well as on their bacterial adhesive properties.

Bacteria are a common source of infections in medical devices implanted inside the human body, such as catheters, knee and hip implants, pacemaker leads, cardiac valves and dental prosthesis [4]. Upon implantation, any device causes micro-organisms to adhere to the implants' surface and eventually form a biofilm, in a process called biofouling. Their tendency to adhere to the implant surface is largely dependant on the chemical and physical properties of the materials at the interface. Therefore, there is a pressing interest in developing novel materials with anti-fouling properties and evaluate their behaviour in terms of cell-modulating response.

The motivation behind this work was based on recent observations that CNTs exhibit strong interactions with living cells and have a cell behaviour-modulation effect which can be either to

Introduction

increase cell adhesion, due to the large surface area and surface energy of CNT aggregates, or to decrease it through bio-functionalization and inhibition of protein adsorption [5].

On the other hand, different effects of CNTs on cells have been reported depending on whether nanotubes were suspended with cells or incorporated in polymer matrices. As a result, there is a necessity to make a more careful assessment of the interactions between cells and CNTs in that a better understanding of these phenomena can bridge the gap between the more fundamental investigation of CNTs and their biological applications. Note that the notion of beneficial or undesirable effect is relative and depends on what the specific goals of the application are. Different situations may require promotion of cell adhesion and proliferation, such as in biofilm formation, *in vitro* cell culture or *in vivo* cell transplantation, whereas others seek to obtain an anti-fouling effect to avoid infections, as for example in medical implant coatings.

Many bacterial strains are responsible for infections in humans, including *Staphylococci*, *Streptococci*, *Escherichia coli* (*E. coli*), and *Salmonella* among many others [4]. For the cell adhesion evaluation, a simple *E. coli* model was used since this bacteria is the most widely used organism for biological studies and has a well-known life-cycle and adhesion behaviour. Besides, the strain used in this work is non-pathogenic and is quite stable in laboratory conditions. Although the results drawn from bacterial models cannot be directly correlated with animal cells, they do often offer an insight into some of the basic mechanistic aspects underlying cellular interactions and thus give a support for further *in vitro* studies.

A composite CNT-polymer system was used as study material rather than the CNTs alone because composite materials have long shown to hold promise for the future of the high-property materials. Furthermore, employing CNTs in a polymer matrix has the further advantage of opening up new ways of applications since their filamentary nature and difficult handling usually hinder many practical implementations.

Another important issue in this work was CNT biocompatibility. Many studies have been published on the citotoxic effects of CNTs on living organisms, which pose further complications to their direct usage for biological and biomedical purposes. This factor can be minimized or even bypassed if the nanotubes are delivered inside a stable biocompatible material which prevents their toxic effects from manifesting but are still able to make use of their exceptional properties to accomplish the desirable functionalities. In this regard, PDMS was chosen as it is a widely used biomaterial with well-known properties and testified biocompatibility and has already been used for the fabrication of the CNT composites.

Due to the complexity of such materials, a more detailed characterization is required to underpin the results obtained and provide a more theoretical explanation of the experimental observations. The evaluation of the cell-adhesion properties of the composites was accomplished through initial adhesion using a well-established parallel-plate flow chamber assay to better approach the real conditions observed inside the human body, such as in the urinary tract, and thus give a more solid result in view of its implications for medical implants. In this work, initial adhesion rather than biofilm formation was studied since the main interest was to assess the ability of the developed surfaces in modulating bacterial adhesion which will impact on biofilm maturation.

1.3 Structure of the Dissertation

In chapter 2 an overview of the state of the art on carbon nanotube-polymer composites with an emphasis on their biomedical applications is given alongside some illustrative examples of achievements in this area. Topics such as the most relevant properties of CNTs, their production and modification methods and broad applications are discussed. Furthermore, methods for preparing CNT/polymer composites and some challenges faced in achieving high quality incorporation are also reviewed. A briefing on biomedical materials and the applications of PDMS is also provided and lastly some notions on bacterial adhesion and its experimental measurement are also highlighted.

Chapter 3 presents a more detailed description of the implementation procedures of the aforementioned goals, such as the strategies adopted for the preparation of the composite materials and for the assessment of their properties and bacterial adhesion.

In chapter 4 all the practical procedures, characterization techniques, experimental set-ups and cell visualization methods are thoroughly described.

All the results obtained and their discussion can be found in chapter 5. When appropriate, a comparison with literature results and theories is also included.

Finally, chapter 6 summarizes the contents of the previous chapters and presents the most important conclusions drawn from this work. Additionally, some topics regarding improvements and future work are discussed to finalize this dissertation.

Introduction

Chapter 2

Carbon nanotube-based materials and their applications

2.1 Introduction

Since carbon nanotubes (CNTs) were first discovered there has been a growing interest among the scientific community to explore their peculiar properties. CNTs have been shown to have exceptional mechanical, electric, thermal and optical properties when compared to other materials [10]. More recently, the biological properties of CNTs have also begun to be evaluated with encouraging results [11]. Great advances have been achieved in understanding the mechanisms of their production and purification processes, as well as in their potential applications in novel nanostructured materials. Of particular interest is the investigation of the use of CNTs in the development of polymer composites. Over the past decade, a growing effort has been put into the study of CNT/polymer systems to discover how their remarkable properties can be harnessed to produce composites with enhanced characteristics [12].

The science of CNTs has also evolved to find new applications of these materials in the biomedical field. CNTs have been widely used in combination with a variety of biomaterials for such diverse purposes as bone and cardiovascular implants, scaffolds for tissue engineering, as well as in biosensors, drug delivery systems, nanoparticle-based therapies and nuclear magnetic resonance spectroscopy [13, 14, 15]. More recently, there has been some reports regarding the evaluation of the direct interaction between CNTs and living cells as well as the biological effects promoted by their incorporation in biomaterials. Biocompatibility and bacterial fouling studies have open up new perspectives on the potential beneficial applications of CNTs in biomedical and biological engineering.

2.2 Carbon Nanotubes

Carbon nanotubes (CNTs) were first discovery by Iijima in 1991 while working for NEC Corporation. He demonstrated the production of graphitic tubular structures mixed with other forms of carbon through the arc discharge method. Carbon nanotubes are allotropes of carbon which can be seen as a graphene sheet rolled into a cylinder with the ends capped with half fullerene balls. This carbon structure of hexagonal networks is therefore closely related to fullerenes, but with an elongation in one dimension [16].

Carbon nanotubes are presently at the focus of intensive research activity due to their exceptional high aspect ratio (i.e., length to diameter ratio), ultra-light weight, structural, chemical, mechanical, thermal, optical and semi- or metallic-conductive properties, which allow them to find applications in a wide variety of technological fields. Although the chemical composition and bonding of CNTs is quite simple, their structure-property relationships are not so straightforward. Besides, CNTs often present many structural defects due to variations in their atom bondings, which results in twists and bends of the tubes and thus altered properties [2]

The main methods used to synthesize CNTs include thermal or plasma-assisted chemical vapour deposition (CVD), arc discharge, pulsed-laser ablation, high pressure CO decomposition and gas-phase catalytic growth methods [12, 2]. The advantage of using the CVD technique is the ability to synthesize well aligned arrays of CNTs on a variety of substrates with controlled diameters and lengths. CNTs have to be sequentially purified to remove catalyst particles, amorphous carbon and other impurities formed in the production process.

CNTs can be classified into two categories: single-wall CNTs (SWCNT) and multi-wall CNTs (MWCNT). The former have this designation because they contain only one graphite sheet rolled onto itself forming the nanotube, whereas the latter are composed of several concentric single walled nanotubes, with varying chiralities (the chiral angle between the hexagons orientation and the nanotube axis (see Figure 2.2)), held together through relatively weak van der Waals forces. MWCNTs in general present more structural defects than SWCNTs. Figure 2.1 shows a schematic representation of SWCNTs (left) and a MWCNT with two sheets (right).

SWCNTs are also classified according to their chirality. The diameter and chirality of the nanotubes depend on the relation between the (m,n) indices shown in Figure 2.2, and according to it CNTs present three different geometrical configurations: armchair (chiral angle = 30°), zigzag (chiral angle = 0°) and chiral (chiral angle between 0 and 30°) [13].

Typically, as-produced MWCNTs have a range of from 2.5 to 30 nm in diameter and from a few of nanometres to some micrometers in length [10], with a density in the range $1.4 - 2 \text{ g cm}^{-3}$. SWCNT, on the other hand, were reported to have diameters of about 1 nm and lengths of 1 μm , but these values vary largely with production and purification methods [16].

2.2.1 Properties of Carbon Nanotubes

Theoretical predictions and experimental measurements have demonstrated the unique properties of CNTs. Iijima *et al.* [17] examined the compression behaviour of single- and multi-walled nan-

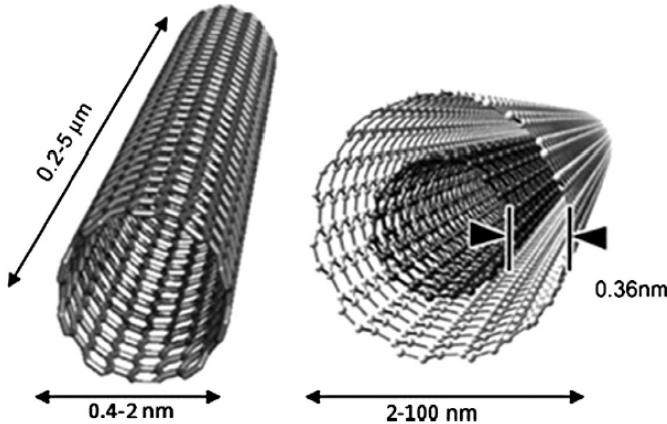


Figure 2.1: Carbon nanotubes: a. single-walled carbon nanotubes (SWCNT) b. multi-walled carbon nanotubes (MWCNT) Reprinted from [1].

otubes and showed that they are very flexible with reversible bending angles as large as 110° . Carbon nanotubes possess high elastic modulus, comparable to that of diamond, and tensile strength ranging from 60 to 150 GPa [12], 10 to 100 times greater than that of steel. Studies have determined that CNT bundles have elastic modulus as high as 1 TPa [10], but it has been suggested that MWCNTs can have Young's modulus as high as 2.24 TPa [18], which is beneficial for their use as reinforcements in high-property composite materials [16]. Other works have also investigated the elastic modulus of isolated MWCNTs coming to values of 1.26 to 1.8 TPa [2].

Moreover, CNTs are stable in temperatures up to 2800°C in vacuum, have a reported thermal conductivity of $3000 \text{ W}/(\text{m K})$ [19], about twice as high as that of diamond, and a current carrying capacity far greater than that of copper wires [2]. Interestingly, CNTs have the peculiar characteristic of presenting different electrical behaviour depending on their chirality, being either metallic conductors or semiconductors, which make them desirable for microelectronic applications.

The high aspect-ratio, typically higher than 1000 [12], and nano-scale dimensions of pristine CNTs gives them high surface energy density of 45.3 mJm^2 [20] and therefore a hydrophobic character by interacting through attractive van der Waals forces. The binding energy between two parallel CNTs have been estimated through atomistic models based on a van der Waals potential model and from calculations based on beam theory with reported binding energies between 0.32 and 0.39 nN [21].

Besides, due to their high flexibility, CNTs tend to get closely entangled into bundles or ropes with a van der Waals binding energy of about 500 eV [22], which results in very low solubility and dispersibility. In general, each CNT aggregate can contain up to hundreds to thousands of nanotubes [16, 23]. These bundles exhibit very different characteristics than individual carbon nanotubes, such as decreased mechanical strength.

Interestingly, an early study by Smalley *et al.* of SWCNTs produced by laser vaporization showed that high-purity SWCNTs deposited after sonication with methanol consisted of a mat of randomly oriented self-organized SWCNT fibers of 10 to 20 nm in diameter and several mi-

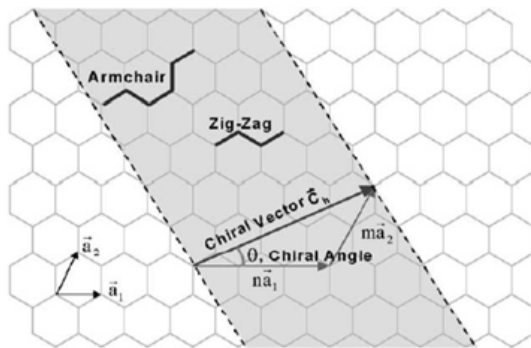


Figure 2.2: Schematic representation of a graphite sheet rolled to form a nanotube and its chiral vector. Reprinted from [2].

crometers in length (Figure 2.3-(a)). These rope-like crystallites of SWCNTs were organized in a 2-dimensional triangular lattice (Figure 2.3-(b) and -(c)) with the individual nanotubes in each rope terminating at the end of the rope within a few nanometers of each other.

Furthermore, CNTs also have near infrared fluorescence properties which can be used in many biomedical applications such as biosensors and radiation-based cancer therapy [24].

2.2.2 Biocompatibility and Bioactivity of carbon nanotubes

The intrinsic hydrophobicity of CNTs is responsible for the strong interactions observed between them and living cells. This fact reveals the potential of CNTs for applications where interactions with cells are an important asset. Therefore, since the potential of CNTs for biomedical applications was first realised, there has been much interest in studying the interactions of CNTs with living cells to assess their biological effects on the host tissue.

The biocompatibility of CNTs refers to the adverse effects on cell viability caused by their interactions with cells. There has been much controversy regarding the cytotoxic effects of CNTs on animal cells, with various contradictory reports stating that CNTs elicited adverse immunologic responses both in *in vitro* and *in vivo* tests [25], while others report more optimistic results with no significant biotoxic effect detected and even show that polymeric matrices modified with CNTs are more biocompatible for cell culture than the pure polymers [26]. For example, a comparative assessment of the *in vivo* immunologic reaction to both SWCNTs and MWCNTs has observed that MWCNTs formed large aggregates within the living tissue whereas SWCNTs, consisting of smaller particles, were easily phagocytosed by macrophages and transported to local lymph nodes. This fact rendered the MWCNTs more toxic than SWCNTs [25]. Besides the needle-like effect of CNTs and tendency to aggregate, other factors have also been suggested to be the cause of the toxic effects of CNTs, such as their shape and size as well as presence of catalytic residues, which also play an active role in their interactions with cells and toxicity [27]. In contrast, other successful achievements in tissue engineering and controlled drug delivery constitute a hallmark for their beneficial application [28].

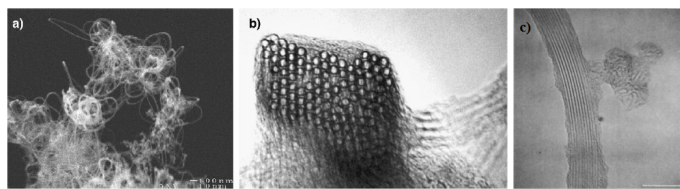


Figure 2.3: (a) Scanning Electron Microscopy (SEM) of SWCNTs showing a mat of entangled carbon fibers of 10 to 20 nm in diameter and several micrometers in length. Scale bar, 100 nm; (b) A single SWCNT rope with 100 nanotubes as it bends through the image plane of the microscope, showing uniform diameters and triangular-patterned packing of the SWCNTs inside the rope. Scale bar, 10 nm; (c) Transmission Eelectron Microscopy (TEM) image of the side view of a rope segment. Scale bar, 20 nm. Reprinted from [3].

However, until this point is clarified the observed undesirable side effects of CNTs should not be disregarded, which implies that the implantation of “free-standing” CNTs in the living tissue may not be the best strategy for their application, but rather a controlled delivery of CNTs anchored to a surface or embedded in a matrix may be a better approach.

It is also known that there are some strategies whereby the biocompatibility of CNTs can be greatly improved, such as chemical functionalization or polymer-grafting. These procedures can not only increase their solubility but also alter their interfacial properties thus having an active role in enhancing their dispersability in the medium and reducing protein fouling with an effect on cell toxicity [5].

One of the main perspectives envisaged by the bio-functionalization of CNTs is the possibility to attach all sorts of bio-active molecules, such as enzymes, proteins or therapeutic drugs to enhance the CNT uptake efficiency by the cells, or whenever used in a polymeric matrix, to render this matrix more suitable for cell proliferation [14] or platelet adhesion resistance [29].

Besides, it has been shown that functionalized CNTs are internalized by both phagocytic and non-phagocytic cells through either by an energy-independent translocation mechanism, with important application in drug delivery systems and targeted therapeutics, or by an endosomally-mediated uptake mechanism [30]. But this also implies that when CNTs are implanted in a living organism, they migrate across the cell membranes through the skin, respiratory or gastrointestinal tracts and eventually end up lodged in the tissues.

Nevertheless, despite these uncertainties there is no doubt that biomodified CNTs show great potential for bionanotechnology applications such as tissue engineering scaffolds, biosensors and drug delivery systems. The examples presented in section 2.5 are just a small sample of all the advances in CNT-based composite materials for tissue regeneration and medical devices.

2.3 Poly(dimethyl siloxane) (PDMS)

Silicones comprise a general category of synthetic elastomeric polymers. Their basic repeating unit is the siloxane molecule, with a peculiar chemical structure consisting of silicon atom bound

Carbon nanotube-based materials and their applications

an oxygen atom with hanging radical group. The most common silicone is poly(dimethylsiloxane) (PDMS), which contains methyl groups anchored along the chain of silicon-oxygen atoms as shown in Figure 2.4.

The combination of an inorganic backbone and organic side groups gives silicones unusual properties with potential usage as fluids, emulsions, compounds, resins, or elastomers.

Among the large variety of biomedical polymer materials, poly(dimethylsiloxane) (PDMS) is the one most widely used for medical implants and materials [31, 32].

PDMS is an elastomeric material with rubber-like properties which makes it extremely versatile for a broad range of applications. It has a very low glass transition temperature around -120 °C and so is less sensitive to temperature and more thermally stable than other rubbers. Besides, it is optically transparent, a characteristic beneficial in many applications [4]. More interestingly, being an elastomer it is extremely flexible with very easy processability. Applications such as insulator materials, flexible electronics, and medical implants have made use of the characteristic.

However, its elastomeric nature means that it has very poor mechanical strength, and therefore PDMS usually needs to be reinforced with fillers for practical applications. Traditionally, PDMS have been formulated with silica particles to obtain enhanced properties, but more recently, there has been a growing trend in using CNTs as fillers instead.

A very important aspect is that PDMS is biocompatible and biologically inert. PDMS decomposes by depolymerization with the formation of linear and cyclic oligomeric products [33] which can be easily eliminated from the body, or decomposed in the natural environment [34, 35].

Regarding biomedical applications, PDMS has found use in such varied areas as in catheters, drains and tubings, orthopedic prostheses, dialysis membranes, cardiac valves, aesthetic implants, heart-bypass implants, stent grafts, ECG electrodes, finger joint implants, contact lenses, scar treatments, bandages and dressings, soft tissue expanders and dental implants [4, 31]. In particular, the hydrophobic character of PDMS gives it interesting applications in coatings with antifouling properties [5], a topic that will be discussed in the chapter 3.

In the field of implantable bioelectronics, the integration of flexibility and stretchability into the devices is becoming an ever more important paradigm to realize human compatible electronic components such as sensors, electrodes and actuators. As far as flexibility is concerned, elastomeric materials have been recognized to be the best candidates due to their better processability [36], so intensive research has been conducted to impinge electrical conductivity to biomedical elastomers by adding electrically conductive fillers.

A more extensive review on PDMS properties, synthesis methods and applications can be found in [4].

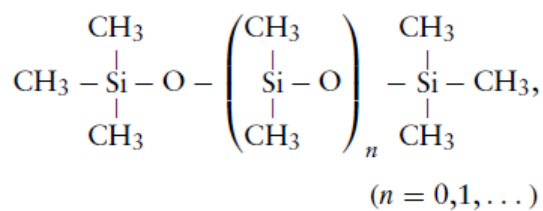


Figure 2.4: Chemical structure of poly(dimethylsiloxane). Reprinted from [4]

2.4 Carbon Nanotube composites

CNTs are undoubtedly a new class of material that sprouted a revolution in nanotechnology with a whole new world of possibilities. They find applications in so diverse areas such as field-emission transistors [37], nanoelectronics [38], chemical and physical sensors [39], biosensors [11], actuators, composites and microelectromechanical systems to nanoprobes for high-resolution AFM imaging [40]. But what makes CNT most attractive is their capacity to be used as reinforcing fillers in polymer matrices to produce novel composite materials with an outstanding improvement in mechanical, thermal and electrical properties for a wide range of applications [12].

The high aspect-ratio of CNTs and their flexibility make them the ideal filler material for polymeric composites since the nanotubes are able to form networks and meshes within the polymer chains thus providing better interconnection between the two materials. Simulations have suggested that nano-fillers with rod-like shape like CNTs are more effective in forming networks with the polymer chains through direct contact among each other or through polymeric chain bridging than other spherical or sheet-like nano-particles [41].

Many different methods have been reportedly used for the fabrication of CNT/polymer composites. These include, solution mixing, bulk mixing, melt blending, hot pressing, extrusion and *in situ* polymerization [12].

When developing any composite material, an important issue is to achieve homogeneous dispersion of the filler inside the matrix to obtain uniform properties and a strong interfacial interaction between both, thereby minimizing the filler loading and obtaining good performance and improved mechanical, conductive, thermal and durability properties. In the same manner, in order to effectively incorporate the advantageous properties of CNTs, disaggregation and uniform dispersion are critical steps in producing high property CNT/composite materials [42]. At the micro- and nano-scale, the surface chemistry of the filler becomes even more important for the quality of dispersion, therefore determining the properties of the final composite [43]. Ineffective dispersions of CNTs in the polymer matrix result in poor performances, far below the theoretical predictions. In the literature, very different results have been reported on the properties of CNT-based composites, showing that the parameters that influence their behaviour depend on many factors, such as the strength of CNT-polymer interfacial interaction, the quality of CNT dispersion, the aspect ratio and extent of preservation of CNT structure after disaggregation treatment. In general, better

dispersions and thus reinforcement of polymers have been achieved with MWCNTs rather than with SWCNTs [43].

Another characteristic of CNT/polymer composites worth mentioning is that the orientation of the nanotubes within the matrix plays a very important role in the bulk mechanical and electrical properties of the composite [44]. In fact, alignment is necessary for the axial load carrying characteristic of CNTs to be utilized. So, several lines of investigation have been devoted to producing composites with the CNTs more or less aligned using various methods such as CVD alignment [45], melt spinning [44], mechanical stretching [46], shear spinning [47], strong magnetic fields [48, 49], electric fields, molecular combing [50] and dielectrophoresis [51]. Other methods, however, have been reported [52].

The major challenges still faced in developing new CNT composite are therefore achieving uniform dispersion, CNT alignment and effective load transfer, since CNTs and polymer materials have drastically different strengths [16]. The structural strength of a composite material is largely dependent on nature of its constituents, the bonding strength and load transfer between matrix and filler. Weak interfacial bondings result in the propagation of fractures and slippage, which leads to failure under applied loads [53]. Successful fabrication of CNT/polymer composites is largely dependant on maintaining stable mixtures of nanotubes inside the polymer matrix and achieving strong interfacial bonding.

The dispersion of the CNTs is a critical issue for maximizing the aspect ratio of CNTs available to bind with the matrix and therefore achieving effective nanotube/polymer adhesion and load transfer. CNTs show a reduced elastic modulus when embedded in a composite which can be a result either of the structural defects or deficient stress transfer. This is not surprising since that in the absence of chemical bonding the load transfer between the CNTs and the matrix arises from weak electrostatic and van der Waals forces. Therefore, careful mixing of the components is essential for separating the CNT bundles and preventing re-aggregation. To achieve that, each CNT has to form an adsorbed layer of polymer to prevent it from interacting with other nanotubes again. This way, the adsorbed polymer layer acts as a stabilizing agent allowing for the formation of a perfectly interpenetrating network instead of two segregated phases [54]. To take full advantage of the potential of CNT application in polymer composites, it is therefore imperative to fully understand the interactions at the nanotube/matrix interface. Many works have been reported that make an attempt to elucidate the mechanisms by which CNT behave inside the host polymer matrix and interact with them to combine their properties to yield materials with enhanced properties [12].

In particular, CNT/PDMS composites are also well reported, with applications mostly in the development of composites with enhanced mechanical and electrical properties [19, 55, 56, 57, 23, 58, 59, 60]. In the work of Beigbeder *et al.* [61], MWCNT/PDMS with various percent loadings were prepared via shear mixing at 1200 rpm, and characterized through tensile stress and DMA tests, static contact angles and swelling measurements to estimate cross-linking density and interaction parameter between polymer and solvent. Their results indicated that the tensile modulus was not affected by the incorporation of MWCNTs up to 0.2 wt%, with an average value of 2.6 + 0.2 MPa. Similarly, no significant alteration of the strain at break was detected for the CN-

T/PDMS in comparison to the control. The swelling measurements for the MWCNT-filled PDMS also showed no significant difference between each loading tested, meaning the cross-linking density was not hampered.

It has also been shown that in order to achieve enhanced properties CNTs must form a physical network both prior and after the cross-linking of PDMS chains. Rheological measurements (complex viscosity, storage elastic modulus and loss viscosity modulus) were used to evaluate the dispersion state of CNTs inside the polymer matrix, since the rheological parameters of a nano-composite can be related to the distribution of the filler. It has been observed that CNTs form an elastic network within PDMS prior to cross-linking, and that the physical liquid-solid transition and dynamic viscoelastic properties of PDMS are strongly affected by this CNT network since it provides additional cross-links. The dispersion of CNTs increase the viscosity of the composite and act as cross-linking agents, accelerating the cross-linking process and increasing cross-linking density. Besides, higher dispersion times promotes better homogeneity and thus accentuates the effect on liquid-solid transition of PDMS [62].

In the work Lordi *et al.* [63] the mechanics of nanotube-polymer binding were analyzed and it was found that the binding energies and frictional forces between both were not so important in determining the strength of interaction, but rather a molecular-level entanglement of the two phases provided by the helical conformation of the polymer chains around the CNTs were the key factor in having a strong bond.

2.4.1 Dispersion methods

It is difficult to control the dispersion mechanism of CNT in a solvent or polymer solution due to the strong van der Waals interactions within the CNT aggregates. These interactions allied to the complex structure of CNT bundles make it hard to establish theoretical models that correlate the microstructure of the composite to its physical properties.

Many attempts have been made to improve the dispersibility of CNT. One common approach is to alter the surface energy of the solids by promoting the formation of covalent or Coulombic type bondings between CNTs and polymer through covalent functionalization of the CNTs with the polymer matrix [64] and surfactant assisted processing through formation of a colloidal suspension [43]. Other involve mechanical methods, as for example, high shear mixing [43, 62], high energy sonication [23], solvent-evaporation methods [65, 57, 56]. Another trend of CNT composite research has been focused on chemical modification of the nanotubes with functional side groups bound to their surface as a feasible and effective means of improving their dispersion in organic solvents and the interfacial bonding between the matrix and nanotubes [19].

Mechanical dispersion methods such as ultrasonication and high shear mixing are effective in separating the nanotubes but have the undesirable effect of fragmenting the nanotubes and therefore decreasing their aspect ratio. With mechanical shear-mixing or ultrasonication the transfer of local shear stress delivers enough energy density for the separation of the aggregates by overcoming the binding energy of the CNT (activation energy barrier). This exfoliation procedure promotes the adsorption of interfacial molecules at the surface of CNTs which assists in their stabilization

and dispersion. However, when the external shear stress is removed, the attractive van der Waals forces drive the CNTs to re-aggregate again into bundles to reach a new equilibrium state of low energy since the dispersion state of CNTs in a solution is thermodynamically unfavourable. This process is further promoted by sedimentation of the aggregates. To prevent this, sonication can be used in conjunction with other techniques to enhanced dispersion through nanotube cutting, since shorter lengths makes the nanotubes less energetically favorable to re-aggregate and sediment.

On the other hand, surfactants can be added to stabilize the CNTs through steric hindrance or static charge repulsion. Different substances can be used to achieve this effect, such as surfactants [43], compatible solvents [66] or polymers [52]. Besides, calculations of the shear-stresses based on solvent viscosity and cylinder geometry strain rates suggested that shear mixing is only suitable for dispersion of MWCNT clusters in high-viscosity polymer melts, reaching fluid strain rates as high as 4000 s^{-1} . For example, using uncross-linked PDMS as mixing medium ($\eta = 5.6\text{ Pa}\cdot\text{s}$), a shear stress imparted below 20 kPa was reported [67].

Ultrasonication, on the other hand, uses cavitation, i.e. the formation and implosion of bubbles, to deliver shear stress for dispersing the aggregates. The cavitation process forms an inhomogeneous distribution of bubbles in the solvent, creating strain rates as high as 10^9 s^{-1} . Although good dispersion states are typically achieved through ultrassonication and high shear-stress mixing, these high energy input methods impart an undesirable tensile force on the CNTs resulting in fracture and breakage [52]. This represents a major drawback since most of the unique properties of CNTs are directly related to their structural integrity.

2.4.2 Chemical functionalization of carbon nanotubes

At the micro- and nano-scale, surface chemistry plays an increasingly important role in determining the dispersibility quality and the degree of interaction between matrix and polymer. As such, surface functionalization by chemical treatments of CNTs has been recognized to be an effective dispersion strategy.

Chemical functionalization consists of creating electrically reactive sites on the defects present on the surfaces of CNTs where other functional moieties or molecules can be covalently fixed. Examples of groups commonly introduced in this manner are hydroxyl, carboxyl and amine groups, or else more complex molecules such as carbonated and polymeric chains. This is also the working principle behind grafting of CNTs with polymers, a technique used to produced water soluble CNTs [12].

A well-established chemical functionalization procedure involves the reaction of CNTs with a high-molarity acid, such as nitric acid or sulfonic acid, followed by filtration and washing with deionized water [12]. Chemical groups, such as carboxylic groups, can be introduced in the defects present in the side-walls and end caps of CNTs through sp^3 hybridization to add new functionalities and improve their solubility [68].

Chemical dispersion involves dispersing the CNTs directly in the polymer solution or using an intermediate solvent [66], such as THF or DMF, which is then mixed with the polymer and removed by evaporation. CNTs have been shown to have negative surface charge in water but

CNTs can be dispersed in water by adding a proper surfactant to help stabilize the tubes through electrostatic interactions. Surfactants are liquids that contain both a polar and an apolar group, thus adsorbing at the interface between immiscible bulk phases. The amphiphilic nature of surfactants has been widely utilized to promote stable dispersions of solids in different media [43]. Since the surfactant molecules are non-covalently adsorbed on the nanotube surfaces, this method of dispersion is non-destructive.

The important parameters to take into account in such a system affecting the surfactant-CNT interaction are the type of surfactant (anionic, cationic or non-ionic), its concentration and the surface functionalization of the CNTs [43]. So far, various different surfactant systems have been employed to coat nanotubes, such as sodium dodecylsulfate (SDS) [69] and sodium dodecyl-benzene sulfonate [70]. There is no obvious evidence regarding which one has better performance, but SDS has been widely used due to its higher efficiency in the interaction of the π -stacking interactions of the benzene rings with the CNT surface [68]. Non-covalent dispersion through the physisorption of a surfactant is an attractive approach since it allows tuning the surface energy of the CNTs without disrupting the π bondings or introducing defects. For a more detailed description on this topic refer to [43].

2.4.3 Conductive behaviour of CNT-polymer composites

Several studies have already highlighted the improvements in electrical conductivity of polymer composites achieved through the incorporation of CNTs, with increases of as much as 14 orders of magnitude reported [20]. This conductive behaviour of CNT-polymer composites has been extensively described in terms of the Percolation theory [71, 72, 73, 74, 20]. Percolation theory is so useful because it is able to predict the universal behaviour of the electrical conductivity and dielectric properties of the composites which does not depend on the matrix and filler *per se*, but only on the spatial dimension of the system, that is, the way the filler is distributed inside the matrix [75]. For a deeper understanding of the basis of Percolation Theory please refer to [76].

According to this model, the DC electric conductivity of a composite as a function of filler load, the so-called percolation scaling law, is described as [65]:

$$\sigma = C(f - f_c)^t \quad (2.1)$$

where σ is the composite conductivity, f is the weight percentage of CNTs, f_c is percolation threshold, C is a constant and t is the critical exponent, a universal value of 2.0 for 3-dimensional systems.

In a CNT-polymer composite system, the very low percolation thresholds achieved are explained in light of the high aspect ratios of CNTs, the type of nanotubes used (usually SWCNT are more conductive than MWCNT) and on the size of CNT bundles [73]. In fact, high aspect ratio nanoparticles act as effective chains inside the polymer, bridging electrical contacts across

the matrix. In the percolative model, interconnectivity of the CNTs and the formation of a closed network is the most important factor [75].

On a more theoretical basis, electrical conductivity in nanocomposites arise from the formation of conductive paths inside the polymer matrix through the filler contacts. The mobility of electrons in CNTs is much higher than in polymers but due to the large surface area of CNTs and their high electron affinity there is a charge transfer phenomenon from the polymer (donor) to the acceptor (CNT), thus allowing for charge carriage across neighbouring without the need for physical contact [73].

Two types of electric conduction between polymer and filler have been hypothesized: resistive conduction and capacitive conduction. The former is establish between neighbouring nanotubes and depends mainly on the number of CNT-CNT contacts whereas the latter relies on the capacitive interactions between the nanotubes, but both depend on the relative amount of CNTs in the composite. Resistive conduction can also be decomposed in two fractions: contact-resistivity, which is the resistance imposed to charge transfer between two distinct nanotubes, and nanotube-resistivity, which is the intrinsic resistivity of the nanotubes [75]. At lower CNT concentrations, the contacts are mainly capacitive, since the CNTs are too disperse in the matrix to come into direct contact. However, as the concentration is raised, the CNTs eventually become more closely packaged and resistive contacts begin to occur, resulting in a remarkable decrease in the impedance magnitude [65]. This phenomenon has been well described by the Percolation Theory and different percolation models have been applied to CNT/polymer composites of various types. This model also introduces the notion of percolation threshold, which is the lowest filler content needed for macroscopic conductivity to increase dramatically through the formation of a conductive path.

The electrical and electronic properties of these composites can be tested using various methods, such as DC conductivity, AC conductivity and impedance spectroscopy. The latter also allows determining the impedance response and dielectric constant of the composites [75]. The physical relationships between impedance, conductivity and dielectric constants for an RC model are well described in [77]. For more profound understanding on Impedance spectroscopy with more complex models refer to [78].

Studies have shown that above the percolation threshold, resistive conduction dominates. Since resistance is independent of frequency, the bulk impedance of the composite therefore depends only on the total number of resistive paths. Below the percolation threshold, however, capacitive conduction takes place, so the total impedance is more dependent on frequency [65]. Besides, above the percolation threshold AC conductivity measurements reveal two distinct regions: a frequency-independent region at low frequencies, and a frequency-dependant region at higher frequencies [75]. That is, the effective conductivity of the materials is mostly constant at low frequencies, and increases at higher frequencies. Regarding CNT/PDMS composites, percolation thresholds from 0.6 wt% [58] to 2.45 wt% [65] have been reported.

2.5 Biomedical Applications of Carbon Nanotube Composites

The applications of CNTs in biomedical engineering are countless. Extensive examples of the biomedical applications of CNTs can be found in the literature [11, 13, 79, 14]. Applications in tissue engineering, cell tracking, biosensing, drug delivery, cell behaviour modulation and polymer matrix enhancement are just a few of them [27]. Regarding tissue engineering, there are reports on applications such as bone grafts using, for example, poly(l-lactide) [80], poly(methyl methacrylate)/hydroxyapatite [81] and polypropylene [82], tissue engineering scaffolds using polycaprolactone [83], poly(3-hydroxybutyrate) [84], chitosan [28, 20], collagen [85] for artificial cartilage, bone cement for prosthesis fixation with acrylic composites [86], as well as cardiovascular tissue engineering using (PLGA) [29, 87] and polyurethane [88]. Other examples include resorbable implants, such as bone screws and fixations plates have also been developed based on CNT composites [80], stent coatings [89], monitoring sensors [39, 40] and neural electrodes [36]. In the sensors category, the advantage of using CNT as nanostructuring fillers becomes clearly obvious in light of their electric properties, which can be harnessed to render widely used polymeric biomaterials electrically conductive for biosignal transmission and transduction.

Carbon nanotube-based materials and their applications

Chapter 3

Bacterial adhesion on surfaces and their interaction with carbon nanotubes

3.1 Interactions between carbon nanotubes and bacterial cells

CNTs have found potential applicability in both preventing biofouling and promoting biofilm formation. Their biofilm modulating response arises mainly from their surface chemistry, state of dispersion of the CNTs in the medium and also from the micropore/mesopore relation of the aggregates [5].

Reduction in biofouling can be accomplished by either imparting bio-modulating activity to the CNTs through the modification with biocidal substances, mediating protein adsorption through chemical functionalization or increasing surface hydrophobicity of a material.

Thus far, the interactions between CNTs and living cells have shown that there are complex mechanisms involved and that CNTs can have very distinct effects depending, for example, on how they come in contact with the cells and on the type of organism. In general, all types of carbon nano-materials show high adhesion affinity with bacterial cells because of the van der Waals forces that arise from their surface energy [90], with pristine CNTs showing a larger adhesive character than functionalized CNTs [20].

The studies conducted on the interactions between “*free-standing*” CNTs and bacterial cells raise evidence of a cell capturing effect. In the work of Kang *et al.* [91] *Escherichia coli* (*E. coli*) K2 cells were incubated with SWCNTs and cell viability assays demonstrated that the highly purified SWCNTs exhibited strong antimicrobial activity due to severe damage caused to the cell membranes through the direct contact with the nanotube aggregates. The nanotubes were able to pierce the cells walls and the damaged cells were deposited with the aggregates.

Other studies have also reported on the formation of CNTs/cell aggregations. In [92] it was demonstrated that SWCNTs have antimicrobial activity to both Gram-negative and Gram-positive bacteria regardless of the surface charge of functional groups present in the CNTs surface and bacteria shape. MWCNTs, on the contrary, did not show significant antimicrobial activity to

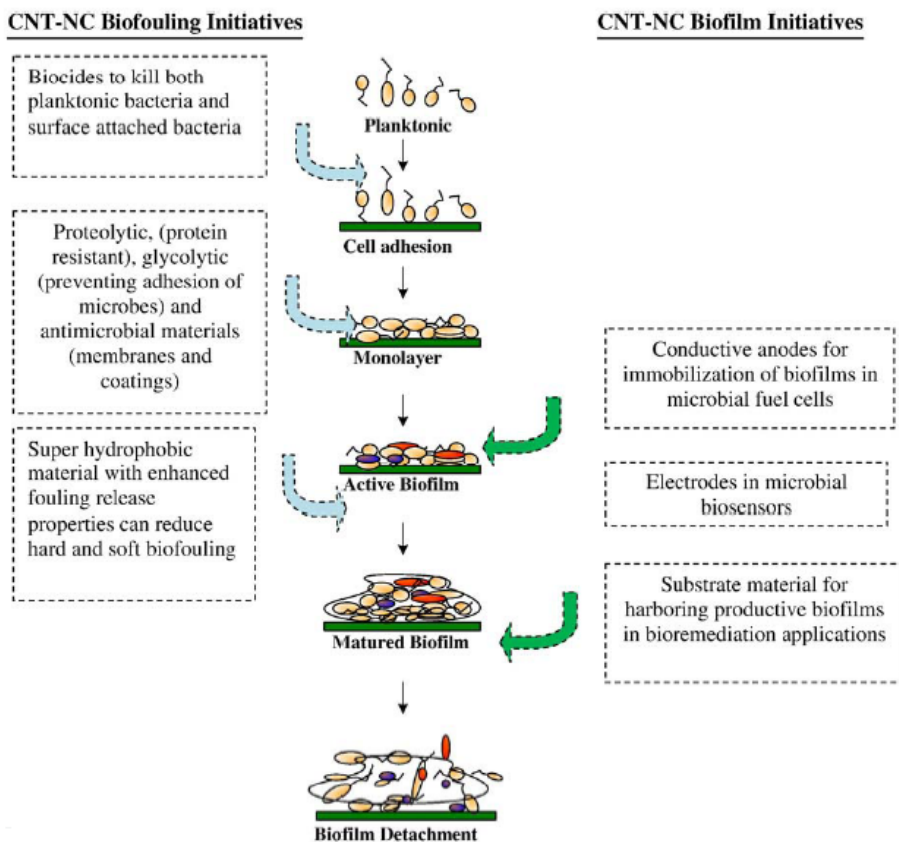


Figure 3.1: CNT nanocomposites activity in biofouling release (left) and biofilm promotion (right) applications in various stage of biofilm growth. Reprinted from [5].

either type of bacteria. The authors also pointed out that SWCNT' antimicrobial activity was buffer-dependent and increased with increasing concentration and treatment time.

In the work of Young *et al.* [93], the authors tested cell viability of *E. coli* after shaking and incubation with carbon nanoparticles, functionalized SWCNT and MWCNTs and verified that both the nanoparticles and SWCNTs had no significant effect on cell viability. It was also noted that the functionalized SWCNTs had a tendency to wind around the curved surface of the *E. coli* cells due to their higher flexibility, resulting in lower toxic effects. MWCNTs, on the other hand, had a visible decrease in cell viability as it was observed that they not only perforated the cells membranes but also caused them to break and thus have a greater cytotoxic effect. Additionally, they concluded that even though carbon nanoparticles and SWCNTs did not have a significant effect on cell viability, their tendency to adhere to the cell surface still has an impact on cell proliferation. However, contrary to these results, Kim *et al.* [94] reported no significant differences in adhesion between bacteria and SWCNTs or MWCNTs clusters.

Further studies supported the idea that individually dispersed SWCNTs in solution are able to form networks on the cell surface and cause the disruption of bacterial membranes [94]. But more interestingly, these results also indicated that collisions between single nanotubes and a

bacterial cells are unlikely to induce the observed physical damages, so the antimicrobial activity of SWCNTs is only possible with interaction of the bacteria with a network of nanotubes.

Akasaka *et al.* [95] have shown that the effects of CNTs in the precipitation efficiency of captured *Streptococcus mutans* cells was much higher for MWCNTs than for SWCNTs due to their larger diameters, more adequate dispersibility and aggregation activity. So, the manners in which they captured the cells was also different which depended on their flexibility. Plus, the authors suggest that there may be differences in the interaction affinity between CNTs and Gram-negative and Gram-positive bacteria.

All these studies hint on some of the possible mechanisms of CNT-cell interaction, suggesting a dependency on such factors as concentration, length, diameter, dispersion or aggregation, stiffness, aspect ratio and exposure duration. But despite all these major advances in understanding the fundamental interactions between CNTs and living cells, the basic mechanisms governing cell adhesion are still poorly understood. SO, it can be concluded that further studies must be conducted to test the influence of all these parameters and validate the aforementioned observations.

Although pristine CNTs exhibit a natural antimicrobial nature, two main issues must be addressed to fully realise their potential. Firstly, there is the concern in preventing the adverse cytotoxic effects of CNTs in the living tissue, and secondly, in devising their implementation in practical applications, such as medical implants with antifouling properties.

Albeit all the work done on CNT-mediated cell adhesion in liquid media, so far little work has been reported on the study of the influence of CNTs on bacterial adhesion when incorporated in the surface of composite materials. It seems, however, clear that CNTs should be made available on the surface for establishing interactions with the cells without causing their systemic release into the organism. Thereafter, CNTs incorporated inside a polymer coating or firmly anchored to a substrate hold great promise for these purposes.

3.2 Adhesion on surfaces

The tendency of two surfaces to adhere to each other, or of a particle to adhere to a surface can be described in terms of its wettability. The wettability of a surface is its wetting behaviour in contact with a liquid phase, that is a measure of a surface's hydrophobicity, which in turn depends on the surface free energy. The surface energy or tension is influenced by both its chemical nature at the interface and its roughness [96].

In fact, the micro- and nano-sized structure of the surface impacts not only on its wettability but also on its mechanical properties [97]. Wettability of a surface is the phenomenon described by the contact between three phases, two of them being gaseous or liquid. The most typical situation and the one applied in this study is a liquid wetting a solid surface in gaseous environment [6]. The wetting properties of a surface are in direct relation to its surface energy and hydrophobicity, thus it is of great importance to measure this property.

The contact angle measurement is a common technique used to determine of the hydrophobicity and surface tensions of a solid surface. Several techniques have been used to measure contact

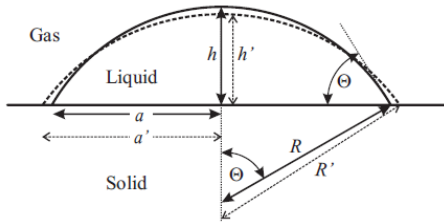


Figure 3.2: Schematic example of the measurement of the angle between a liquid drop and a circular contact area on a planar solid surface. Reprinted from [6]

angles based on Young's equation [98]. The most common technique used for measuring the Contact Angle (CA) is the Sessile Drop technique, which was the method used in this work to determine the surface free energy of the fabricated composite materials. In this method, a light source is placed behind a falling drop and a picture of the drop as it touches the surface is taken. The contact angle is then outlined from the contour of its cross section [6]. The contact angle formed depends not only on the surface tension but also on the liquid used.

A quantitative description of wetting phenomena occurring at a three-phase interface line has been theorized by Young's equation, based on the spreading of a drop of liquid on a solid surface. This equation relates the contact angle (ϕ) formed by the drop to the interfacial tensions γ_s , γ_L and γ_{SL} :

$$\gamma_{LV} \cos \phi + \gamma_{SL} = \gamma_{SV} \quad (3.1)$$

where γ_{SV} is the tension (or interfacial free energy) of the solid-vapor interface; γ_{LV} is that of the liquid-vapor interface; and γ_{SL} is that of the solid-liquid interface.

If $\phi > 10^\circ$ then the spreading coefficient $\$ = \gamma_s - \gamma_{SL} - \gamma_L$ can be neglected and equation 3.1 becomes:

$$\gamma_L \cos \phi + \gamma_{SL} = \gamma_s \quad (3.2)$$

where γ_s is the tension (or interfacial free energy) of the bare solid surface; γ_L is the interfacial tension of the liquid surface; and γ_{SL} is the interfacial tension of the solid-liquid interface. θ is the angle measured between the solid-liquid interface and the line tangent to the liquid interface at the contact point with the solid surface, as show in Figure 3.2.

If ϕ is smaller than 90° then $\cos \phi$ is positive and $\gamma_s > \gamma_{SL}$. Thus, the liquid partially wets the solid and vice-versa. Young's equation can be derived considering the differential change of Gibbs free energy (dG) with spreading area. From the thermodynamic point of view, the spreading of the drop is spontaneous if the change in Gibbs free energy is negative. Doing some mathematical manipulation considering constant drop volume and spherical geometry, as well as negligible

Laplace pressure and gravitational force acting on the drop, the following equation can be derived:

$$dG = (\gamma_{SL} - \gamma_S)dA_{SL} + \gamma_L dA_L \quad (3.3)$$

$$= 2\pi a(\gamma_{SL} - \gamma_S)da + 2\pi a\gamma_L \cos\phi da \quad (3.4)$$

In thermodynamic equilibrium, $dG/da = 0$, so $\gamma_S - \gamma_{SL} = \gamma_L \cos\phi$. Using Dupré equation for the work of adhesion (equation 3.5) of a sessile drop to the solid surface that is in equilibrium with the vapour phase and combining with Young's equation (equation 3.1) yields the Young-Dupré equation 3.6 [99]:

$$W_{SL} = \gamma_S + \gamma_L - \gamma_{SL} \quad (3.5)$$

$$\gamma_L(1 + \cos\phi) + S = W_{SL} \quad (3.6)$$

In the present study, the sessile drop method was used to measure the CA between the fabricated composite thin film coatings and three different liquid phases: water, 1-bromonaphthalene and formamide. The reason for choosing these liquids is their different polarity, which allows one to determine the surface energy of the substrate according to the Thermodynamic theory, presented next for sake of clarity. The equations that follow and a more detailed explanation can be found in [9].

The Thermodynamic theory of adhesion energy of a surface aims at proving a quantification for the free Gibbs energy of that surface, which in turn relates to the probability of another surface or material adhering to it. It takes into account two types of interactions: the Acid-Base interactions (AB) and van der Waals forces (LW). These two types of interaction are related to the intrinsic properties of the material. Another type of interactions, the electrostatic forces, also contribute to the total surface energy but are not taken into account by the electrostatic theory since these are also related to the medium that the surface is in contact with.

So, the free Gibbs energy of adhesion can be determined based on the following equations [9]:

$$\gamma^{tot} = \gamma^{LW} + \gamma^{AB} \quad (3.7)$$

where

$$\gamma^{LW} = 11.1(1 + \cos\theta_{br})^2 \quad (3.8)$$

with γ_s^{LW} being the surface energy due to the van der Waals forces and θ_{br} the contact angle

measured with 1-bromonaphthalene (apolar liquid). And,

$$\gamma^{AB} = 2\sqrt{\gamma^+\gamma^-} \quad (3.9)$$

Where γ^{AB} is the surface energy due to the Acid-Base interactions and γ^+ and γ^- are the contributions of the positive and negative charges, respectively:

$$\sqrt{\gamma^-} = 9.485(1 + \cos \theta_{water}) - 8.402(1 + \cos \theta_{br}) - 6.063(1 + \cos \theta_{form}) \quad (3.10)$$

$$\sqrt{\gamma^+} = 7.209(1 + \cos \theta_{water}) - 3.080(1 + \cos \theta_{br}) - \sqrt{\gamma_s^-} \quad (3.11)$$

$$= -2.276(1 + \cos \theta_{water}) + 5.322(1 + \cos \theta_{br}) + 6.063(1 + \cos \theta_{form}) \quad (3.12)$$

where θ_{water} and θ_{water} are the contact angles with water (at 22 °C) and formamide, respectively. So,

$$\gamma_s^+ = \begin{cases} \sqrt{\gamma_s^+} & : \sqrt{\gamma_s^+} > 0 \\ 0 & : \sqrt{\gamma_s^+} < 0 \end{cases}$$

$$\gamma_s^- = \begin{cases} \sqrt{\gamma_s^-} & : \sqrt{\gamma_s^-} > 0 \\ 0 & : \sqrt{\gamma_s^-} < 0 \end{cases}$$

Which gives:

$$\gamma^{tot} = \gamma^{LW} + \gamma^{AB} \quad (3.13)$$

Then, the Gibbs energy can be determined through:

$$\Delta G_{lw}^{LW} = -2(\sqrt{\gamma_s^{LW}} - \sqrt{\gamma_{water}^{LW}})^2 \quad (3.14)$$

$$\Delta G_{lw}^{AB} = 4(\sqrt{\gamma_s^+ \gamma_s^-} + \sqrt{\gamma_{water}^+ \gamma_{water}^-} - \sqrt{\gamma_s^+ \gamma_{water}^-} - \sqrt{\gamma_s^- \gamma_{water}^+}) \quad (3.15)$$

$$\Delta G_{lw}^{tot} = \Delta G_{lw}^{LW} + \Delta G_{lw}^{AB} \quad (3.16)$$

Note that these parameters only refer to the nature of the surface itself. But in the present study the interest is in determining the probability of *E. coli* adhering to the coatings, or the Gibbs Energy of Adhesion, so it is necessary to calculate the free energy of interaction between surface and *E. coli*. Since there are three phases in this system (surface (s), water (w) and bacteria (b)),

three components have to be determined: γ_{sb} , γ_{sw} and γ_{bw} . γ_b^{LW} , γ_b^+ and γ_b^- refer to the cell surface hydrophobicity (CSH) parameters. Equations 3.8 and 3.8 determine γ^{AB} and γ^{LW} .

$$\gamma_{sb}^{LW} = (\sqrt{\gamma_s^{LW}} - \sqrt{\gamma_b^{LW}})^2 \quad (3.17)$$

$$\gamma_{sb}^{AB} = 2(\sqrt{\gamma_b^+ \gamma_b^-} + \sqrt{\gamma_s^+ \gamma_s^-} - \sqrt{\gamma_s^+ \gamma_b^-} - \sqrt{\gamma_b^+ \gamma_s^-}) \quad (3.18)$$

$$\gamma_{sb}^{tot} = \gamma_{sb}^{LW} + \gamma_{sb}^{AB} \quad (3.19)$$

And the same applies for γ_{bw} and γ_{sw} .

Therefore, the free energy of adhesion between a solid substrate and *E. coli* is:

$$\Delta G_{adhesion} = \gamma_{sb} - \gamma_{bw} - \gamma_{sw} \quad (3.20)$$

$$\Delta G^{AB} = \gamma_{sb}^{AB} - \gamma_{bw}^{AB} - \gamma_{sw}^{AB} \quad (3.21)$$

$$\Delta G^{LW} = \gamma_{sb}^{LW} - \gamma_{bw}^{LW} - \gamma_{sw}^{LW} \quad (3.22)$$

As mentioned before, this theory only takes into account the acid-base and van der Waals interactions, which is a somewhat simplified assumption. More elaborated theories that also consider the electrostatic interactions, such as the (Derjaguin-Landau-Verwey-Overbeek) DLVO theory and the Extended DLVO (XDLVO) [100, 101, 102], which combines both, have already been applied for this type of studies. The latter would be of particular interest for this work since it would allow a better approximation to the system in use. However, that would require the measurement of Zeta-potentials [101] which is a time-consuming technique. Thus, the approach of using the simplified Thermodynamic theory was chosen.

3.3 Antifouling Surfaces

In the industry of medical implants it is desirable to have materials with strong antifouling properties is to minimize device-related infections.

Since biofilm formation on a surface depends on the capacity of cells to initiate adhesion, assessing initial adhesion on surfaces is an important step to estimate the tendency of a surface to form biofilm [103]. Therefore, tuning surface properties to reduce or inhibit initial cell adhesion may result in biofilm-resistant surfaces.

Superhydrophobic surfaces are well-known for their antifouling properties. Some materials have an intrinsic fouling release character. Some examples are PDMS, chitosan and iodinated polymers such as polyurethane-iodine [5], but silicone elastomers have been suggested to be the most promising fouling-release coatings.

PDMS has high performance in fouling-release of attached organisms, which has been imparted on its low surface energy and high hydrophobicity and high local chain mobility.

An example of the use of a CNT/PDMS composite material for antifouling purposes is the composite silicone elastomer/MWCNT surfaces prepared by Beigbeder *et al.* previously mentioned [61]. Interestingly, the static contact angles of their CNT/PDMS composites surfaces increased after immersion in demineralised water for 7 days, meaning that the surface became slightly more hydrophobic. They reported evidence that these composite containing 0.05% of CNTs enables significant reduction on the adhesion strength of adult barnacles, despite the fact that the bulk properties of PDMS were not altered with the filling.

Another important approach in developing materials with antifouling and fouling-release properties is by designing their surfaces at the nano-scale level, as it has been realised that the nano-roughness effect on cell adhesion and biofilm formation is perhaps more important than the hydrophobicity [96]. The very low wettability of nanostructured surfaces has long been recognised with the discovery of the well-known “Lotus effect” of the leafs of the lotus flower. Their self-cleaning and superhydrophobic properties are very attractive and have inspired scientists to seek new ways of mimicking that effect in synthetic surfaces. Other examples of nano-structured surfaces with exceptional anti-fouling and wettability properties are known [104].

Approaches to designing integrated biomimetic composite surfaces using CNTs are still scarce, but this area will surely become one of the leading forces on the development of high-performance surfaces in the near future.

3.4 Parallel Plate Flow Chamber Bacterial Adhesion Assay

The parallel-plate flow chamber is a device used for flow simulations with cells suspensions to subject the cells to fluid shear stresses similar to those found in a particular environment, say the human body.

In a parallel plate flow chamber (PPFC) there are two mass transport phenomena, namely convection (parallel to the substrate surface) and diffusion (towards the substrate surface). The flux of cells in the flow chamber can be controlled by the flow rate of the passing medium, and the optical density of cells in the suspension. The attractive van der Waals forces between bacteria and the surface are balanced by the hydrodynamic drag forces experienced near the interface [105].

There are also electrostatic forces, which can be either attractive or repulsive depending on the surface and micro-organism used.

For steady state laminar flow between infinite parallel plates, the wall shear stress, τ_w , as a function of the flow, Q , is given by the following expression:

$$\tau_w = \mu \frac{6Q}{bh^2} \quad (3.23)$$

where μ is the viscosity of the fluid and b and h are the width and height of the chamber, respectively.

For a real finite length flow chamber, the flow is assumed to be laminar with a parabolic velocity profile within a range of Q at the middle portion of the chamber. The distance from the entry at which the velocity profile approaches the theoretical profile, with a difference by 1%, is given $L_{entry} = 0.04hR_e$, where $R_e = Q\rho/(\mu b)$ is the Reynolds number. At the boundaries, the flow assumes turbulent regimes. So, the effective surface exposed to laminar flow (homogeneous shear stress) depends on the ration b/h [7]. According to equation 3.23, the shear stress is maximal at the plate surfaces.

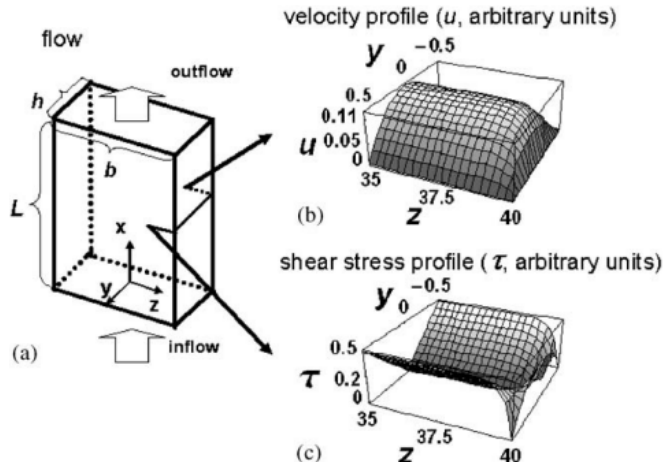


Figure 3.3: A flow chamber example and its velocity and shear stress profile in arbitrary units. (a) Diagram of a parallel-plate flow chamber of width b , height h , and length L , in its orientation in the x - y - z axes. The fluid is forced through the chamber by a steady pressure gradient along the x -axis. (b) and (c) show the calculated velocity profile u and the shear stress profile τ , respectively, for an aspect ratio b/h of 80: The arrows indicate that the profiles were taken very near the right edge of the flow chamber. The shear stress has its maximum value at the plate surfaces and vanishes at the chamber corners. Parabolic velocity profile and homogeneous wall shear stress are characteristic for steady flow between parallel plates. Reprinted from [7].

As mentioned, the Thermodynamic theory of adhesion accounts for cell adhesion on a surface in terms of the surface energy of the material and properties of the medium. But it has been reported that shear stress of the medium also plays an important role in governing bacterial adhesion.

These reports, however, show that there is not a defined relation between cell adhesion and shear, with some reporting an increase of cell adhesion with increasing shear, and other reporting the opposite [103]. Besides this contradictory behaviour, the tendency for bacteria to adhere seems to be non-linear with shear stress, with a drop in cell attachment when shear stress increases to a critical value [103, 100]. The reasons that have been pointed out to explain these observations is that there is a critical shear stress above which cells detach from the surfaces, so that when shear is increased beyond that value, cells are no longer able to adhere to the surface.

From all these pbservations, it seems that adhesion seems is also species dependent. Even within the same organism, different values of critical shear stress were determined, which suggested that the critical shear stress was also dependent on the medium, with the pH having a great impact. Further investigations suggested an hysteresis effect of shear stress on cell attachment and that there were two different values of critical shear, one for cell detachment and other for preventing cell attachment, which was much lower since the van der Waals and acid-base interactions responsible for initial attachment were also much lower than strong receptor-ligand interactions that oppose cell detachment [103].

Additionally, there are still some biological factors affecting adhesion kinetics in biologic systems. It has been suggested that there is a time dependency in adhesion strength driven by phenotypic changes that trigger the development of adaptive traits in bacteria [102] and by the presence of a flagellum (in the case of *E. coli*). Moreover, another limitation of the systems used for measuring initial cell adhesion comes with the fact that bacterial strains grown in batch cultures in the laboratory are subjected to different selection pressures than the ones found in their natural environment (in this case the human body), as well as varying nutrient status and growth stage which may lead to changes in their cell surface [102].

Chapter 4

Materials and Methods

This chapter presents the techniques used in this work for the preparation of the CNT/PDMS composite materials and their characterization as well as for the bacterial adhesion assays.

MWCNTs were used because they are more readily available and are more easily processed. The analytical methods employed to characterize the CNTs included thermogravimetry (TG), Temperature Programmed desorption (TPD) and N₂ adsorption isotherms. The CNT/PDMS composite films were fabricated using three different methodologies: a bulk mixing process, whereby the CNTs were directly incorporated in the PDMS matrix through shear mixing combined with sonication; a solution mixing process using an intermediate dispersing agent and shear mixing; and double-layer deposition of a CNT thin film through solvent evaporation covered with a PDMS layer.

The composites were characterized by Thermogravimetric analysis (TG), contact angle (CA) measurements, Scanning Electron Microscopy (SEM), Atomic Force Microscopy (AFM), X-ray Photoelectron Microscopy (XPS) and Fourier-Transform Infrared Microscopy (FTIR). Additionally, optical Transmittance Microscopy images of the composite films were also taken to obtain a more direct assessment of the distribution state and agglomeration degree of the CNTs inside the polymer. Some of the samples were also immersed in liquid media to assess their degradation behaviour. The various composite coatings were also characterized in terms of surface conductivity with a two-probe DC conductivity test.

Bacterial adhesion on the coatings was studied with a parallel-plate flow chamber (PPFC) in steady state flow conditions with laminar regime using *Escherichia coli* as model organism. The number of cells adhered was determined using two different cell counting methods: on-line imaging with optical microscopy and end-point fluorescent imaging with DAPI staining.

Materials and Methods

4.1 Chemical and Mechanical treatment of the MWCNTs

For the preparation of CNT samples with different surface chemistry and textures, commercially available pristine MWCNTs (p-CNT) (NanocylTM NC3100) produced by catalytic CVD with an average length and diameter of $1.5\mu\text{m}$ and 9.5 nm, respectively, were used. It has been shown that these CNTs have average inner and outer diameters of 4 and 10 nm, respectively, and that they contain only residual traces of growth catalyst impurities, mainly Fe (0.19%) and Co (0.07%), S(0.14%) and Al(0.03%) [106].

In order to introduce acidic groups on the surface of the p-CNTs, they were chemically functionalized by a well-established oxidation treatment with HNO_3 . The procedure was done as described in [8]. Briefly, a sample of p-CNTs was oxidized in reflux with HNO_3 in a Pyrex round-bottom flask containing 300 mL of HNO_3 7 M and 3 g of p-CNTs, connected to a condenser. The liquid phase was heated to boiling temperature (130°C) with a heating mantle for 3 h. Oxidized CNTs were obtained (f-CNT). After this process, the f-CNT were washed with distilled water to neutral pH and dried in an oven at 110°C overnight.

The samples of f-CNT were subsequently submitted to thermal treatments under N_2 flow at different temperatures, 400°C , 600°C and 900°C , to produce different MWCNTs with a successively lower amount of oxygen-containing groups and thus lower acid character. This is possible because heating the f-CNT causes the chemical groups to be selectively decomposed from the surface, depending on the final temperature. The thermal treatments were conducted as described in [106]. A fused-silica tubular reactor was heated to the final temperatures of 400, 600 and 900 $^\circ\text{C}$ at a heating ramp of $5\text{ }^\circ\text{C min}^{-1}$ under flow of N_2 ($100\text{ Ncm}^3\text{min}^{-1}$) and remained at that temperature for 1 h. At the end, f-CNT-400, f-CNT-600 and f-CNT-900 were obtained.

Pristine CNTs (p-CNTs) were ground using a ball milling (BM) machine (Retsch MM200) at 15 krpm for 180 min and functionalized CNTs (f-CNT, f-CNT-400, f-CNT-600 and f-CNT-900) were ball milled at 15 krpm for 90 min. Different ball milling times (180 and 90 min) were used due to limitations in time.

All the CNTs samples prepared and methods used are summarized in Table 4.1 and a schematic overview of the various procedures used for preparing the samples is shown in Figure 4.1.

Previous studies where the point of zero charge of similar samples of CNTs (both with chemical and heat treatments) have verified that the p-CNTs have a neutral pH (7.0), whereas the HNO_3 -CNT, HNO_3 -CT-400, HNO_3 -CNT-600 and HNO_3 -CNT-900 CNTs have an acidic character due to the presence of the acidic groups at their surfaces, namely carboxilic acids and lactones, with pH values of 3.0, 3.8, 5.9 and 7.3, respectively [106, 107]. Since the oxygenated groups are partially removed with the thermal treatments, the CNTs heated at higher temperatures have a successively less acidic character, and the HNO_3 -CNT-900 samples even showed a slightly basic character. The pH of the different types of CNTs is an important factor to consider in their dispersion in a non-neutral solvent or in a polymer matrix, since their surface charge may influence the bonding force with the polymer chains.

Materials and Methods

Table 4.1: List of the different carbon nanotube samples prepared and the methods used.

Sample	Treatment
f-CNT	Oxidation treatment with HNO_3 7M at 130 °C for 3h
f-CNT-400	Thermal treatment under N_2 flow at 400 °C for 1h
f-CNT-600	Thermal treatment under N_2 flow at 600 °C for 1h
f-CNT-900	Thermal treatment under N_2 flow at 900 °C for 1h
p-CNT-BM	Ball-milling treatment for 180 min at 15 krpm.
f-CNT-BM	Ball-milling treatment for 90 min at 15 krpm
f-CNT-400-BM	Ball-milling treatment for 90 min at 15 krpm
f-CNT-600-BM	Ball-milling treatment for 90 min at 15 krpm
f-CNT-900-BM	Ball-milling treatment for 90 min at 15 krpm

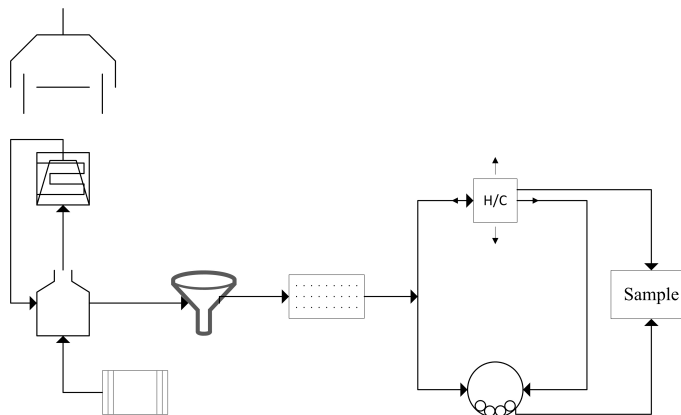


Figure 4.1: Process Flow diagram of the procedures used for preparing the various CNT samples.

4.2 Preparation of CNT/PDMS composite coatings

This section describes the procedures used to prepare the composite thin layers. In the present work, MWCNTs with different surface chemical and structural properties were used for the preparation of the composite materials in order to assess the role of these characteristics in the dispersion state and properties of the final composite, namely p-CNT, f-CNT, and p-CNT-BM and f-CNT-BM.

4.2.1 Bulk Mixing

The first step in the dispersion of the CNTs in the PDMS (Sylgard 184 Part A, Dow Corning; viscosity = $1.1 \text{ cm}^2\text{s}^{-1}$; specific density = 1.03) matrix was shear mixing with a magnetic bar at 500 rpm for 30 minutes. This stage allowed for a rough dispersion of the CNTs, without breaking the aggregates apart, which facilitated the subsequent dispersion steps. In this phase, the composite

Materials and Methods

presents a rather heterogeneous composition, with the large aggregates clearly distinctive from the PDMS. With the ball milled CNTs, it was observed that a much better dispersion could be obtained by shear mixing alone.

The CNT/PDMS mixture was then subjected to a sonication procedure (Hielscher UP400S, at 200 Watt and 12 kHz) for at least 1h, until the CNTs were all macroscopically dispersed. At this point, the composite acquires a perfectly homogeneous appearance with a back opacity (see Figure C.1 of the Appendix C). However, even after sonication there were some clusters of CNTs suspended in the composite that failed to disperse.

After that, since some bubbles were detected in the bulk material, a 30-minute ultrasound bath (Selecta Ultrasons) step was added for their elimination. The curing agent (Sylgard 184 Part B, Dow Corning) was then added in a proportion of base-polymer to curing agent of 10:1 and carefully stirred to homogenize the two components without re-introducing bubbles. The calculation of weight percentage of CNTs took into account the cross-linking agent.

Thin film coatings were then deposited on microscope glass slides using the spin coating technique (Spin150 PolosTM). A briefing on spin coating theory can be found in appendix E. Two different rotation speeds were used depending on the viscosity of the final composite. When the viscosity of the material is too high, the speed is increased. For this procedure, two spin speeds were used: 2000 and 6000 rpm. The composites with 0.1 wt % CNT content or with the CNTs with BM treatment were spun at a lower speed of 2000 rpm, whereas the ones with 1 wt% of CNTs were spun at 6000 rpm to allow for coverage of the entire slide surface since these were more viscous.

4.2.2 Solution Mixing with a Solvent

Based on the reports stating that better dispersions could be achieved using a proper solvent as intermediate dispersing agent (refer to section 2.4 of chapter 2), in particular ionic surfactants and organic solvents, two different solvents were chosen to test the CNT dispersion: sodium dodecylsulfate (SDS) 10% v/v and tetrahydrofuran (THF).

However, due to the poor miscibility of PDMS in SDS only CNT suspension in THF was used to fabricate the composites through this method. Uniform dispersions of CNT in THF were achieved through magnetic stirring at 1200 rpm for 6 h and the suspensions were then mixed with PDMS at 500 rpm for more 16 h. During this process, THF was partially evaporated but the remaining solvent resulted in lower viscosity of the composite solution, so spin coating was not the best option to produce the films. Alternatively, the mixture was manually spread on the glass substrate to form a thin layer as uniform as possible. Table 4.2 summarizes all the composites and the conditions used.

4.2.3 CNT-PDMS double-layer composites

In order to further investigate the electric properties of the CNTs, another type of coatings was produced through a different technique. CNTs were first dispersed in a liquid phase, SDS 10%

Materials and Methods

Table 4.2: List of the different types of composites produced through the evaporation/infiltration method. All spin coating parameters were fixed (200 rpm/sec, 60 seconds) and the spin speed (ω_S) was varied between 2000 rpm and 5000 rpm.

Composite	Type of CNT	Solvent	ω_S (rpm)
PDMS/p-CNT 0.1 wt%	Pristine	PDMS	2000
PDMS/f-CNT 0.1 wt%	HNO ₃ -Functionalized	PDMS	2000
PDMS/p-CNT 1 wt%	Pristine	PDMS	6000
PDMS/f-CNT 1 wt%	HNO ₃ -Functionalized	PDMS	6000
PDMS/p-CNT-BM 1 wt%	Pristine Ball Milled	PDMS	2000
PDMS/f-CNT-BM 1 wt%	HNO ₃ -Functionalized Ball Milled	PDMS	2000
PDMS/p-CNT-BM-THF 1 wt%	Pristine	THF/PDMS	-
PDMS/f-CNT-BM-THF 1 wt%	HNO ₃ -Functionalized	THF/PDMS	-

v/v and pure THF, at a mass concentration of 5 mg·mL⁻¹ for 6 h under magnetic stirring at 1200 rpm to obtain a stable suspension, as in the previous method. After that, 1mL of CNT suspensions were deposited in glass slides and gently rocked until all surface was covered.

Then, the liquid was left to evaporate overnight at room temperature (RT) and at atmospheric pressure. When all the solvent dried, the slides were covered in a PDMS layer through spin coating. Two speeds, 2000 and 5000 rpm, were used to produce PDMS layers of different thickness. The coatings were then cured in a stove at 80 °C for 1.5 h as described in the previous section. With this evaporation technique, the goal was to have a layer of individual CNTs and CNT bundles forming a continuous network and therefore a closed conductive path. The pores could then be filled with polymer to obtain a consistent composite. With this method the polymer disperses into the vacant areas on the nanotube film giving structural support and consistency at the same time, as previously reported [108, 109]. The fraction of CNTs in this type of double-layer composite is solely dependent on the concentration of the CNT dispersion and the volume of dispersion deposited onto the slides. Due to in time limitations, it was not possible to assess the adhesion strength between the CNT and PDMS layers.

4.3 Characterization Techniques

4.3.1 N₂ Adsorption Isotherms

The N₂ Adsorption Isotherms technique is based on the analysis of the partial pressure of an adsorbant gas to describe the surface coverage of that gas as a function of its pressure, thus giving the rate of adsorption r_{ad} or rate of desorption r_{des} . This information can be used for a textural characterization and to compared the surface area of the samples. If the samples has porosity, this technique allows determining the volume of micro-porous.

The Langmuir adsorption isotherm assumes several assumptions, namely that the adsorption is localized and that only the first monolayer of non-interacting molecules is bound to the surface

Materials and Methods

(i.e. immobile on the surface); that the sample surface is saturated when all sites are covered, forming a monolayer; and that there are no interactions between the adsorbed particles [110].

The surface area covered by the adsorbant gas can be determined from the *Brunauer–Emmett–Teller* (BET) isotherm, which applies the principles of *Langmuir* isotherm to multilayer adsorption and is described as [110]:

$$\frac{\frac{p}{p_0}}{(n_a(1 - \frac{p}{p_0}))} = \frac{1}{n_m^a * C} + \frac{C - 1}{n_m^a * C} \frac{p}{p_0} \quad (4.1)$$

where p and p_0 are the equilibrium and the saturation pressure of the adsorbates at the temperature of adsorption; C is the BET constant; n_a is the adsorbed gas quantity; and n_m^a is the mono-layer adsorbed gas quantity.

$$S_{BET} = n_m^a N_A a_m \quad (4.2)$$

In the present work, N_2 Adsorption Isotherms of the acid and heat treated CNT samples (f-CNT, f-CNT-400, f-CNT-600 and f-CNT-900) were determined at $-196\text{ }^\circ\text{C}$ with a Quantachrome NOVA 4200e apparatus. The Brunauer–Emmett–Teller (BET) surface area of the various materials was then computed and compared to evaluate their textural characteristics.

4.3.2 Thermogravimetric analysis

Thermogravimetric (TG) analysis is an analytical technique used to measure the amount and rate of mass loss in a material as a function of temperature or time in a controlled atmosphere. In this technique a sample is continuously heated from a given starting temperature to a final temperature with a constant heating rate, in the presence of a gas flow, and the weight loss of the sample and a result of the decomposition process is monitored over time as a function of temperature [111].

This method allows the assessment of its composition from the various steps of the weight loss process as well as its thermal stability from the onset temperature of the decomposition of the material. The higher the temperature at which the decomposition starts, the more stable the material is. The decomposition temperature depends on the chemical nature and structure of the sample, so this type of measurement allows for an inspection of structural differences in the conformation of the polymer chains induced by the introduction of a filler [112].

In this work, PDMS, PDMS/p-CNT 0.1%, PDMS/p-CNT 1%, PDMS/p-CNT-BM 1%, PDMS/f-CNT-BM 1% and PDMS/p-CNT-thf 1% were analysed to assess the effect of the incorporation of the CNTs on the thermal stability of PDMS and therefore evaluate the extent of bonding between matrix and filler. p-CNTs and f-CNTs were also analysed as comparison. The heating program used was $T(t) = 700t + 50$, where T is the temperature in $^\circ\text{C}$ and t is time. The total amount of weight loss of the samples was determined from the integration of the area below the mass-time curve and the on-set temperature of decomposition were compared among the various tested samples to evaluate their thermal stability.

4.3.3 Temperature Programmed Desorption (TPD)

In the present study, TPD analysis was carried out with the p-CNT, p-CNT-BM, f-CNT, f-CNT-400, f-CNT-600 and f-CNT-900 samples. The experimental procedure was followed as previously reported [106]. In brief, TPD profiles were obtained by heating the samples from room temperature to 1100 °C at a heating rate of 5 °C·min⁻¹ with a total flow rate of the helium carrier gas of 25 Ncm³ min⁻¹ in an AMI-200 (Altamira Instruments) apparatus. About 0.09 g of each sample was analyzed by tracking the signals of 18 (H₂O), 28 (CO) and 44 (CO₂) with a Dymaxion mass spectrometer (Ametek Process Instruments). The signals were then processed and analysed to obtain the total mass of CO and CO₂ released from the samples.

Further information on the theory of TPD analysis and the calculations used to analyse the results are included in Appendix F.

4.3.4 Contact Angle Measurements

To characterize the composites in terms of surface energy and adhesion energy with *E. coli*, static contact angle (CA) measurements were performed directly on the coatings with a CA apparatus (Dataphysics Contact Angle System OCA) using the sessile drop method. Calculations of the surface energy were based on the termodynamic theory, as described in chapter 3.

4.3.5 Degradation Assay

The degradation assays were conducted to assess the chemical stability of the composite films in a liquid environment. Two types of tests were conducted. Firstly, a 30 minute-assay in citrate buffer with the PPFC using the same flow conductions as the adhesion assays was done to allow for an assessment of whether there was any degradation of the composites during the adhesion assays. Then, contact angle measurements were taken to compare the surface energy of before and after the degradation assays.

Secondly, in order to assess long term degradation, another assay in static flow conditions was performed. The static degradation assays were performed as follows: coatings of three different types, PDMS (control), PDMS/p-CNT 0.1 wt% and PDMS/p-CNT 0.1 wt% were placed on petri dishes and immersed in either citrate buffer and synthetic urine for 1 day, 4 days and 8 days inside a flow chamber. The extracted liquid was analysed by UV-Vis spectrometry (Jasko V-530). This technique was chosen since it allows for the inspection of a wide range of wavelengths and it was more suitable for analysing small amounts of sample over time. Besides, this techniques has been previously used to analyse PDMS [113]

4.3.6 Surface Analysis

The fabricated composite films were characterized with Scanning Electron Microscopy (SEM), Atomic Force Microscopy (AFM) in tapping mode, X-ray Photoelectron Microscopy (XPS), all

Materials and Methods

performed at CEMUP (Centro de Materiais da Universidade do Porto), and Fourier-Transform Infrared Microscopy (FTIR).

These techniques allow surveying the surface of a material to extract information on morphology (SEM), topographical features (AFM), elemental composition (XPS) and chemical bonding environment at the outermost layers (XPS and FTIR). The aim was to probe the surface in order to gain better understanding of the interactions occurring between the CNTs and PDMS polymer chains, as well as of the distribution profile of the CNTs across the surface and along the height of the film.

XPS is an analytical technique based on the localized emission of an X-ray beam into a sample's surface to survey its chemical composition. XPS analysis was performed in a Kratos AXIS Ultra HSA using an Al K α monochromatic X-ray source (1486.7 eV) at 15kV (40 eV for the regions spectra and 80 eV for the surveys). XPS spectra data was analysed with XPSPeak software. Four regions of interest were specified in the analysis: C 1s, O 1s, N 1s and Si 2p since these are the main elements composing the samples. The main goal was to evaluate the amount of these elements present at the outermost layer of the various samples so as to make a comparative assessment of distribution of the CNTs near the surface. The samples were prepared by cutting small sections of each composite coating.

SEM images of the different coatings were taken to allow for a more detailed inspection of the surface morphology and roughness of the coatings and to see whether the introduction of CNTs and the amount introduced had a major effect on the surface structure. Moreover, samples of the coatings in glass slides were fractured along the cross-section in order to visualize the cross section and estimate the thickness of the coatings. Ten pictures of each cross section were taken to calculate the average thickness. Another objective was to complement the XPS analysis in assessing the differences in carbon content at the surface of the various coatings to evaluate the distribution of the CNTs along the depth of the coatings. Additionally to SEM, Energy Dispersive X-ray Spectroscopy (EDS) analysis was also simultaneously performed to examine the chemical composition of the regions analysed and thus complement XPS analysis.

FTIR analysis (Perkin–Elmer 1710) was done in Attenuated Total Reflectance (ATR) mode since in transmittance mode a significant saturation was observed. Composite membranes were fabricated by mould casting on petri dishes to a small thickness so that the laser could better penetrate on the samples.

4.3.7 Conductivity Measurements

To assess the effect of the introduction of CNTs in the PDMS matrix on the conductivity properties of the composites, DC conductivity tests were performed. A DC voltage (V) signal in the range -100 to +100 Volt or -1 to +1 Volt was applied on each sample, depending on the conductivity of the samples, and the corresponding current (I) was measured at 21 points in 10 runs. The current-voltage curves were obtained and an average value of conductance (I/V) was calculated from a linear fit of the curves.

Materials and Methods

The electrical characterization was conducted at Centi (Centre for Nanotechnology and Smart Materials). In brief, two copper contacts were placed on top of the coating with a separation of 2 cm and then connected to a power source (Keithley Programmable Single Channel DC Power Supplier). DC voltages in the range -10 to 10 Volt or -100 to 100 Volt were applied to the terminals, depending on the conductivity behaviour of the coating (higher range for lower conductivities) and the superficial current between the two terminals was read into a costume LabView® application. The characteristic current-voltage curve for each sample was registered and analysed. Glass cover slides and PDMS coated slides were used as controls.

4.4 Cell Adhesion Assay

4.4.1 Cell Cultivation and harvesting

In this work, *E. coli* JM109(DE3) was used as biological model since it is a well-studied micro-organism of a non-pathogenic strain [114]. A starter cell culture was obtained using the same procedure as described in [114]. In brief, the cells were collected from a cryo-preserved batch (1 mL aliquots in glycerol stock kept at a constant -80 °C) and thawed at room temperature (RT). Then, 200 mL of culture medium, prepared as previously described [115], was inoculated with 500 µL of cells suspension and incubated for 24 h at 30 °C with a constant orbital agitation of 150 rpm. A volume of 10 mL of the cultured bacteria were centrifuged (Eppendorf Centrifuge 5810R) at 25 °C in 4000 rpm rotation for 10 minutes, re-suspended in sterile citrate buffer at pH 5 and centrifuged again in the same conditions. The final cell suspension was then diluted in citrate buffer until an optical density (OD) of 0.1, corresponding to a cell density of $7.6 \cdot 10^{-7}$ cells per mL, was achieved. This OD density was used since this *E. coli* strain has optimal adhesion

4.4.2 Parallel Plate Flow Chamber assay

Cell adhesion assays were performed using a parallel-plate flow chamber (PPFC) (see Figure A.1-(b) of the appendix A), with a height, width and length of 0.8, 1.65 and 25.4 cm, respectively, and entry/exit diameters of 0.2 cm. The PPFCs contained a bottom and top opening for the introduction of the test surfaces and the coated slides were mounted in the bottom plate at the exit end of the PPFC. The opening at top plate was covered with an uncoated glass slide to allow for real-time visualization at the microscope. A schematic overview of the experimental set-up used is shown in Figures 4.2 and 4.3.

The flow cell was coupled to a reactor connected to a centrifugal pump and tubing system through which circulated a steady flow of *E. coli* suspended in citrate buffer at an OD of 0.1. A valve at the exit of the pump allows for flow rate control. The equipment was also coupled to a water bath to keep a constant temperature of 37 °C throughput the experiments. This temperature was used since it is the normal temperature of the human body. Appendix A contains illustrative photographs of the experimental set-up.

Materials and Methods

The shear stress in the human urethra has been estimated in values from 0.001 Pa up to 0.3 - 0.5 Pa in the course of urination. Plus, *E. coli* adhesion is reportedly dependent on the shear stress conditions [116]. However, in the present work, it was impractical to test various different shear stresses, so a constant value was used since the purpose was to evaluate the dependence of bacterial adhesion on the surface characteristics of the coatings and not on the flow conditions. Therefore, all the tests were conducted using a constant shear stress of 0.01 Pa in laminar regime. This intermediate value was chosen to best mimic the flow conditions of shear stress in the human urinary tract in normal physiological conditions. The shear stress in the system was adjusted by tuning the flow rate in the tubings. According to equation 3.23 and considering the viscosity of water at 37 °C as an approximation, the flow corresponding to a shear stress of 0.01 Pa was calculated as 2.5 mLs⁻¹.

Citrate buffer was used as cell medium in the adhesion assays since it is a simple solution deprived of nutrients, thus minimizing the interference of the medium in cell adhesive behaviour. Besides, its saline composition keeps the osmotic pressure of the cells stable, thus ensuring their integrity during the assay. Besides, buffer solutions neutralize the charge alterations driven by substances excreted by the bacteria. In previous work, various buffers at different pH were tested and it was found that citrate buffer at pH 5 had the best performance in potentiating the cell adhesion, which is necessary for this type of studies with this strain of *E. coli* to obtain a reliable cell countings.

4.4.3 On-line Cell Adhesion Assay

Online adhesion assays were performed with the PDMS, PDMS/p-CNT 0.1% and PDMS/f-CNT 0.1% since these were optically transparent. In the on-line adhesion assays the flow cells were placed on the microscope support and real-time optical microscopy (Nikon Eclipse LV100) images were taken with a magnification of 10x for 30 minutes at a time cadence of 30 seconds. This allowed for acquisition of a time series of images that correspond to the initial adhesion of *E. coli* in the coating inside the flow cell. Bacterial adhesion was assessed by performing cell countings on the acquired time-series images from light transmittance microscopy. This procedure allowed off-line data and the construction of kinetic adhesion curves. Image analysis was performed as explained in the next section. A schematic representation of the set-up described in the previous topic is shown in Figure 4.2.

4.4.4 End-point Cell Adhesion Assay with DAPI staining

In the case where the coatings were not optically transparent or the background of the images produced had too much interference from the carbon nanotubes, it was not possible to use the image analysis procedure described in the previous subsection. For that reason, another cell counting strategy had to be adopted. Cell adhesion assays with similar set-up as the one used in the previously section but with a series flow cell configuration (see Figure 4.3) were conducted and

Materials and Methods

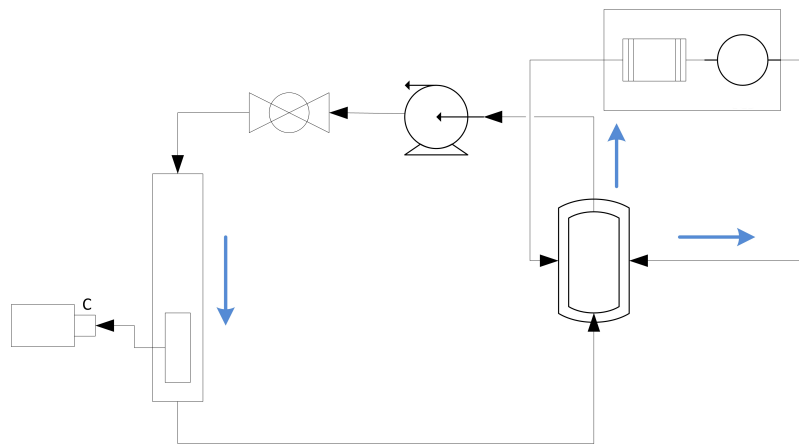


Figure 4.2: Process Flow Diagram of the set-up used for the on-line *E. coli* adhesion assays, drawn with Microsoft Visio® Software. The blue arrows indicate flow direction in the tubes.

end-point cell countings were performed with DAPI cell staining. The samples were then visualized under fluorescence microscopy (*Nikon H600L*) with a 100x magnification. About 20 images of three non-overlapping areas of the coating were taken using *NIS AR v4.13.04* Software, taking care to avoid those areas that were pinched by the flow cell. Two repeats were done for each different type of coating.

4.4.5 Image Analysis

The microscopy images recorded during the on-line cell adhesion assays were then analysed with costume Matlab code in order to obtain the number of adhered cells and cell surface density over time (30 minutes assay). For that purpose, each image was analysed separately in order to eliminate effects of varying contrast and luminosity as well as camera movement and jitter during the experiment.

The algorithm was implemented using *Matlab* (MathWorks®) programming environment and the pseudo-code is presented at the end of this subsection. The reason for choosing this application development platform is that *Matlab* offers a fully-fledged and stable set of tools, called Image Processing Toolbox, that contains built-in functions for most of the image processing techniques used in routine image analysis. For more information on Image Processing with Matlab refer to [117].

The image processing flowchart is presented in Figure 4.4. The algorithm developed was focused on three main processing steps:

1. Contrast enhancement and background subtraction;
2. Top-hat Transform;
3. Image segmentation through binarization.

Materials and Methods

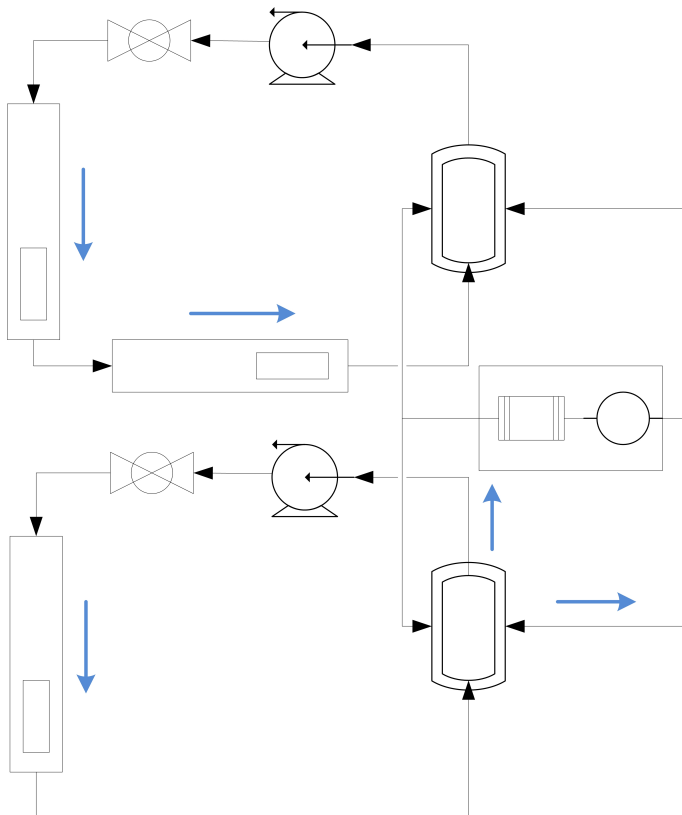


Figure 4.3: Process Flow Diagram of the set-up used for the end-point *E. coli* adhesion assays, drawn with Microsoft Visio® Software. The blue arrows indicate flow direction in the tubes.

The reasoning behind this process flow is based on the notion that the cells are treated as image objects in a background, which contains no information and can thus be removed. Therefore, these objects present enough contrast to be segmented from the background and are the only relevant objects in the images. Of course, the latter condition is only ideal and light optical microscopy images often contain various undesirable objects (artefacts) that should not be accounted for but cannot be easily segmented from the objects of interest. A way to circumvent this problem is to find features that differentiate them, but often at the expense of excessive computational cost. Two main simple features often used are object size and morphology [118], which are also the easiest ones to implement. In this sense, morphological operations were chosen to perform this task, through the implementation of a top-hat Transform and subsequent opening operation.

The two basic morphological operations are Dilation and Erosion. Dilation is a morphological operation that has the effect of enlarging the areas of the foreground (complement to the background) such as white pixels and shrinking areas of the background. It corresponds to the logical OR operator of binary images. It is symbolically defined as [118]:

$$g(j,k) = f(j,k) \oplus b(j,k) \quad (4.3)$$

Materials and Methods

where f is a gray-scale image and b is a structuring element, composed of a set of pixels with a certain size and shape. That is, Dilation of f by b is the set of all pixels such that f and b overlap by at least one non-zero element. On the other hand, Erosion on an image erodes away the boundaries of foreground pixels such that those areas of foreground pixels shrink in size and "holes" within those areas become larger. Conversely, Erosion corresponds to the set of all pixels that overlapped by H are still contained in f , that is, the logical AND operator. The definition is [118]:

$$g(j,k) = f(j,k) \ominus b(j,k) \quad (4.4)$$

Opening is another morphological operation that is defined as an erosion followed by dilation. Its effect is that it tends to decrease the spatial extent of an object, so it can be used to extract objects with a specified shape and smaller than a given size from the segmented binary image.

$$f \circ b = (f \ominus b) \oplus b \quad (4.5)$$

where again f is a gray-scale image and b is a structuring element. Top-hat Transform is mathematically defined as a gray-scale f minus its opening by a structuring element b , so a kind of background subtraction. It is used for yielding an image with only the objects removed using a structuring element and is particularly helpful to correct uneven lightening in the background [119].

$$f = f - (f \circ b) \quad (4.6)$$

However, it may be the case that certain artefacts present in the image still remain after morphological operations because they have similar size and shape from the objects. To prevent these artefacts from contributing to the final cell countings, the strategy implemented was to subtract the number of objects counted at the initial time instant from the resulting countings. This heuristic was based on the idea that all the objects present in the image at time zero are artefacts (things that were already adhered to or embedded in the surface of the coating before the assay was started) and therefore their presence remains unchanged throughout the entire assay.

Binarization is the operation of transforming a grayscale image, that is an image defined by gray-level pixel values within a certain dynamic range, into a binary (purely black and white) image, thereby segmenting the objects from the background.

In order to maximize the information extracted from each image sequence, 12 non-overlapping regions of interest (ROI) inside each image were defined and again analysed independently. This way, 12 different countings can be determined from each sequence and their mean calculated to decrease the error of the algorithm inherent to the nature of the images and improve the confidence on the results.

Materials and Methods

```
1 initialize empty variables
2
3 k=1;
4 for i = 1:12 % define subregions
5     for j = 1:61 % image of time point i
6         im <- read image
7         im2double(); % convert to double
8         imadjust(); % adjust dynamic range
9         bkg <- imfilter(); % smoothing with gaussian to produce background image
10        im - bkg; % subtract background
11        im(x:x+299,y:y+299); % extract subregion
12        imresize(im,[1200 1200]); % resampling
13        imtophat(); % top-hat transform
14        im2bw(); % binarize gray-lebel image with graythresh()
15        imopen(); % Open transform with 3 pixel-radius structuring element
16        bwareaopen(); % remove small objects from image
17        bwconncomp(); % connected components to obtain number of objects
18    end
19 end
```

Listing 4.1: Matlab pseudo-code of the image analysis script used for the cell countings of the kinetic cell adhesion assays.

Finally, a step of feature extraction can be used to evaluate certain properties of the objects, such as area, perimeter, axis length, orientation, eccentricity.

Materials and Methods

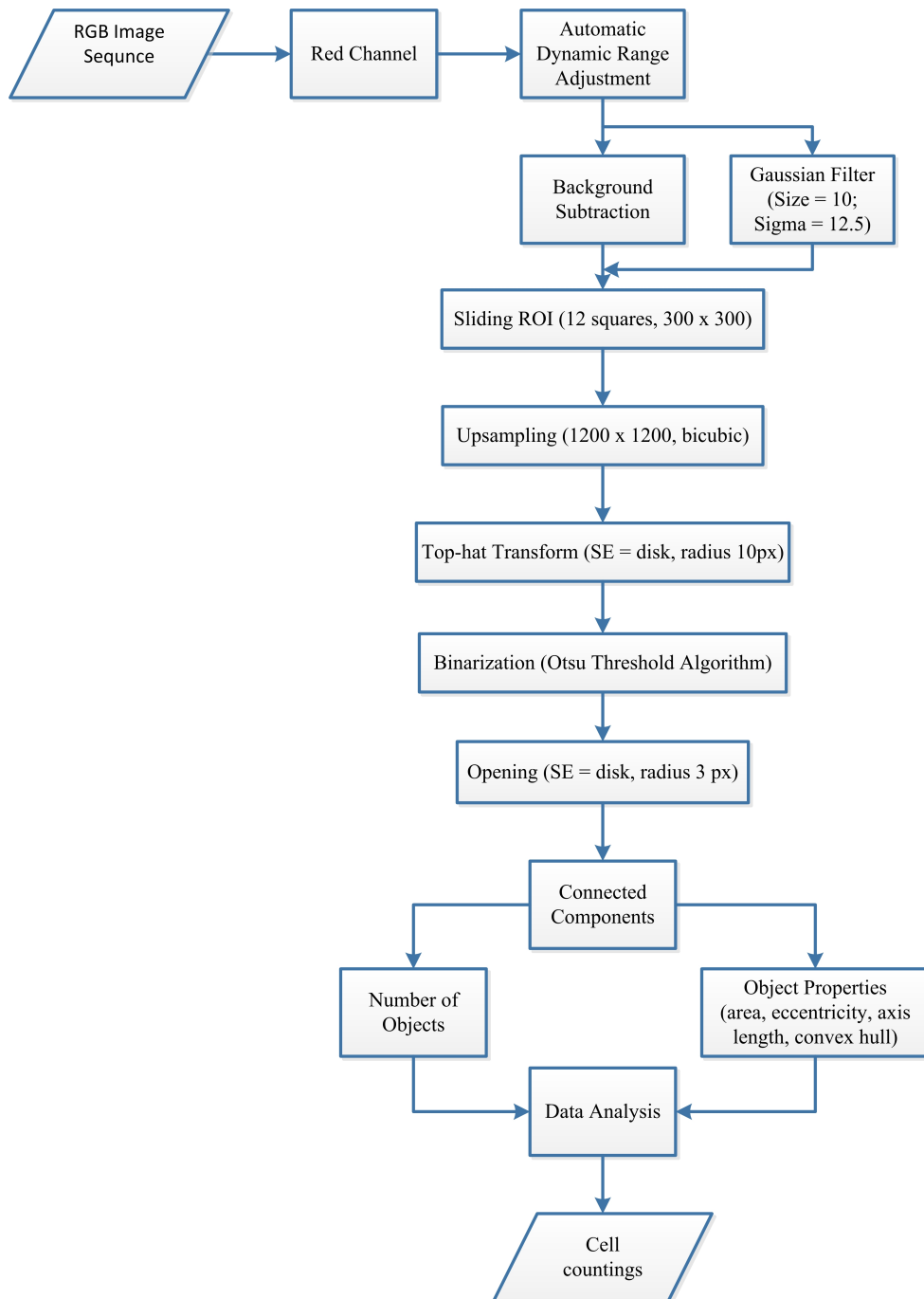


Figure 4.4: Process Flow Diagram of the set-up used for the end-point *E. coli* adhesion assays, drawn with Microsoft Visio® Software. The blue arrows indicate flow direction in the tubes.

Materials and Methods

Chapter 5

Results and Discussion

5.1 Composite Coatings

5.1.1 Bulk mixing

The composite coatings fabricated by the bulk mixing process with 0.1 wt% CNT loading showed a black opaque appearance after sonication, but when they were cast on thin films, they showed a light grey colour with good optical transparency, with some small punctual CNT aggregates visible to the naked eye. Despite this minor content of non-dispersed nanotubes the coatings had a uniform appearance with no macroscopic roughness.

The composites with 1 wt% of CNTs also had a black opaque appearance after sonication, but when spin cast they revealed some re-aggregation of the nanotubes. This happened in part due to the higher content of aggregates present in the composite, which were not dispersed with sonication, but also possibly due to some extent of segregation of the CNTs from the PDMS matrix. It is possible that the centrifugal force pushed the smaller well-dispersed nanotubes against the aggregates that were deposited on the substrate during the spinning and eventually became incorporated in the aggregates, which acted as nucleation sites, instead of being uniformly distributed throughout the film. Thus, the matrix and CNTs were eventually in two phases and the CNT content outside the aggregates was lower than 1 wt% in the end.

The composite films produced with the ball milled (BM) nanotubes at 1 wt%, however, showed an overall uniform aspect, much more similar to the 0.1 wt% coatings. This was due to the better dispersion of CNTs in the matrix and to the much smaller size of the remaining aggregates. Again, the films were more or less optically transparent, though still more opaque than the ones with lower content of CNTs, with a uniform grey colour and no observable roughness.

Illustrative images of the interior of each coating described in this section, taken with optical microscopy, are presented in the appendix C. A simple binarization procedure of the images of the 1 wt% coatings yielded 2-dimensional percentage coverages with CNTs of a random plane inside

Results and Discussion

the bulk of the materials of 27%, 33%, 29% and 21%, for the p-CNT 1%, f-CNT 1%, p-CNT-BM 1% and f-CNT-BM 1%, respectively.

5.1.2 Solution-mixing

The composites produced through the solution mixing process using THF as dispersing agent had a completely uniform appearance without aggregates, showing that THF was effective in promoting the disaggregation of the CNTs and steric stabilization during mixing with PDMS. Besides, the fact that THF has a low boiling point of 66 °C (but still high enough for the solvent to evaporate slowly) contributes for an effective mixture of the CNT suspension within the PDMS matrix.

It has been reported that the use of intermediate solvents can have a negative impact on the matrix-CNT interactions due to their coating effect [43]. However, THF is an organic solvent with a simple molecular structure (a cyclopentane ring with one of the carbon atoms substituted by an oxygen atom). Besides, PDMS has good solubility on THF [120], which also contributes for an effective integration between polymer and CNTs.

Despite partial evaporation of THF, the resulting mixture was still more fluid than the ones previously prepared, so the films were deposited on the glass slides using a manually spreading method. As a consequence, the surface roughness was higher than that of the films produced by spin coating.

5.1.3 Double layer coatings

It could be observed that a uniform mat of CNTs was deposited on the glass slides after solvent evaporation, and that this mat was sufficiently consistent for the nanotubes to remain attached to the surface. The PDMS layer deposited on top by spin coating was well-adhered on the nanotubes and had different thickness depending on the spin speed. Here, the spin speed was varied between 2000 and 5000 rpm and from the appearance of the surface texture of the final coatings it could be seen that the films produced with 5000 rpm presented a rougher surface.

A list of the different double-layer coatings produced along with the corresponding mass of the CNT layer are shown in table 5.1. Note that the ones fabricated with SDS have a much great mass than the ones made with THF, which shows that the salt content of the SDS solution was mostly retained in this layer during the evaporation process and was deposited on the spaces between the nanotubes.

Since the mass fractions of CNTs and PDMS in the final coatings depend on several parameters, namely the dispersibility state of the suspension, the precise volume of suspension poured into the glass substrates, the amount of PDMS dispensed in the spin coater and the spin speed, it is a difficult task to obtain films with exact and reproducible weight fractions of CNT/PDMS. For that reason, the masses of CNT and PDMS were measured with analytical scales in order to determine the weight fractions of each composite film individually and compare between the different films. These results also are shown in table 5.1.

Results and Discussion

Table 5.1: List of the different types of composites produced through the evaporation/infiltration method. All spin coating parameters were fixed (200 rpm^{-1} , 60 seconds) and the spin speed was varied between 2000 and 5000 rpm.

CNTs	Solvent	m_{CNT} (mean \pm std)(mg)
p-CNT	SDS	52.9 ± 28.5
f-CNT	SDS	45.7 ± 16.7
p-CNT	THF	6.2 ± 0.9
f-CNT	THF	5.9 ± 1.3

5.2 Characterization Techniques

5.2.1 N₂ Adsorption Isotherms

The MWCNTs samples prepared through the various chemical, heat and ball milling treatments were analysed by N₂ adsorption isotherms to determine their surface area and make a qualitative assessment of their textures. Surface area (S_{BET}) is an important parameter for the characterization of modified CNTs since it is known that chemical or mechanical treatments may result in structural modifications.

The results are presented in Figure 5.1 and in Table 5.2 and Figure 5.1. The pristine CNTs yielded the lowest surface area (S_{BET}), as would be expected since the pristine CNTs were not submitted to any kind of chemical or structural modifications. The p-CNT-BM, on the other hand, have a significantly higher surface area due to the cleavage and nanotube opening provoked by the milling treatment. In accordance with the other results, all the functionalized CNTs showed increased S_{BET} when compared to the pristine nanotubes. Note that the CNTs treated 600 °C have higher S_{BET} than the ones treated at 400 °C, and that the f-CNT-900 had the lowest S_{BET} of the three, but these small differences lie within the experimental error of ± 10 °C, so it can be considered that these samples have comparable textural properties.

Regarding the ball milled (BM) functionalized CNTs, the surface area of the f-CNT-BM sample is slightly smaller than that of the f-CNT-400-BM, f-CNT-400-BM and f-CNT-400-BM samples, which cannot be accounted for by the experimental error. This may be justified by procedural errors since the milled f-CNT sample presented an S_{BET} much lower than the others where the heat treatment was also applied. As expected, the surface area of the milled HNO₃-CNTs increases with increasing temperature of the thermal treatment, with the milled heat-treated CNT samples showing the highest surface areas of all samples.

These results were important to show that there is an alteration of the CNTs at the structural level after the functionalization and ball milling, which may influence the bulk and surface properties of the fabricated composites. One must bear in mind that the interactions between nanotubes and polymer matrix are largely influenced not only by the chemical nature of the CNTs, but also by the surface available for the establishment of non-covalent interactions. Furthermore, shorter CNTs are also easier to disperse in a medium since the nanotubes have less tendency to aggregate.

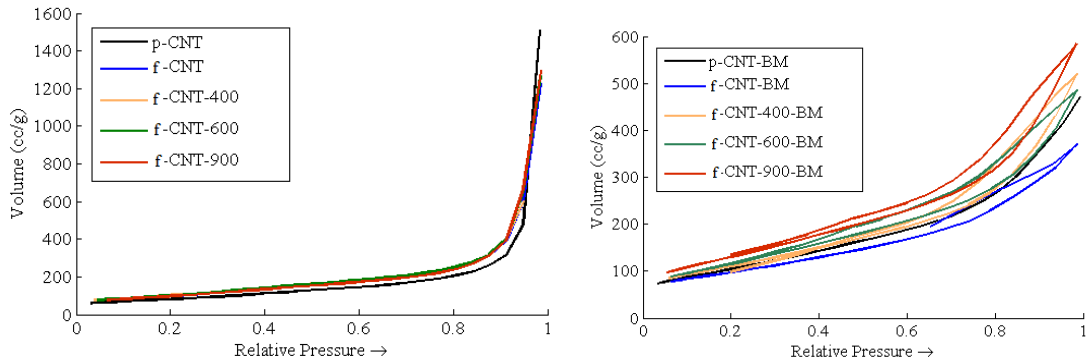
Results and Discussion

However, despite the improvement of the dispersability, the shortening and wall opening induced by these treatments affect the aspect ratio of the CNTs, which may have a major impact on the interconnectivity of the nanotube networks that are formed within the polymer matrix and thus on the establishment of electrical contacts and formation of a percolative path.

Table 5.2: S_{BET} determined from N_2 adsorption isotherm analysis of the samples (± 10 °C).

Sample	$S_{BET} (\text{m}^2\text{g}^{-1})$
p-CNT	289
f-CNT	361
f-CNT-400	366
f-CNT-600	374
f-CNT-900	352
p-CNT-BM	375
f-CNT-BM	348
f-CNT-400-BM	403
f-CNT-600-BM	428
f-CNT-900-BM	479 ¹

¹ Value likely to be unreal due to loss of sample mass.



(a) N_2 Adsorption isotherms of the p-CNT, f-CNT, f-CNT-400, f-CNT-600 and f-CNT-900 samples. (b) N_2 Adsorption/desorption isotherms of the p-CNT-BM, f-CNT-BM, f-CNT-400-BM, f-CNT-600-BM and f-CNT-900-BM samples.

Figure 5.1: N_2 Adsorption isotherms of the pristine CNTs (p-CNTs) and the CNTs prepared with the acid functionalization (f-CNT), heat treatment (f-CNT-400, f-CNT-600 and f-CNT-900) and ball milling (BM) treatment.

5.2.2 Thermogravimetric Analysis

To evaluate the effect of the incorporation of CNTs on the thermal stability of the PDMS matrix, thermogravimetry (TG) analysis was performed. The CNTs were also individually analysed for comparison. The resultant spectra of the p-CNT, f-CNT, f-CNT-400, f-CNT-600 and f-CNT-900

Results and Discussion

samples is shown in Figure 5.2-(a), and the spectra of the PDMS, PDMS/p-CNT 0.1%, PDMS/p-CNT 1%, PDMS/p-CNT-BM 1%, PDMS/f-CNT-BM 1%, PDMS/p-CNT-THF 1% samples in Figure 5.2-(b).

This graph shows the percentage of mass retained during the analysis. The corresponding percentage mass loss at 700 °C (end temperature of the analysis) are shown in Table 5.3. The total mass loss was obtained by normalizing the final mass loss by the initial mass of the samples.

The TG spectra of PDMS showed that it starts pyrolysing at around 450 °C, with a rapid mass loss until 600 °C. At this temperature, the polymer reaches a plateau and begins to stabilize. At 600 °C, a mass loss of 60% was obtained. The PDMS/p-CNT at 0.1 wt% showed a very different thermal behaviour, with the decomposition onset around the same temperature as PDMS, but with a less abrupt mass loss and resulting also in a lower percentage of mass loss (40 %). Comparing this with the curve of the PDMS/p-CNT 1% composite, it can be seen that a higher amount of CNTs in the polymer results in higher thermal stability, with the curve showing even less mass loss than with a CNT loading of 0.1%.

Surprisingly, with the p-CNT-BM nanotubes, the composite had a similar decomposition as with the p-CNTs, suggesting that the structure and texture of the nanotubes is not a critical factor in the thermal stability of the composite. However, with f-CNT-BM, there is a significant difference in the decomposition. Even though the curve of the PDMS/f-CNT-BM follows the same smooth mass loss as the PDMS/p-CNT-BM, the mass loss at 700 °C approached that of PDMS, about 60%. This may indicate that the surface chemistry of the CNTs, unlike their structure, plays an important role in the filler-polymer interactions. The oxygen-containing groups of the functionalized CNTs introduce polar moieties in the matrix which probably have low affinity for the PDMS chains due to sterical and electrostatic repulsions. Comparing with the TG curves of the CNTs (Figure 5.2-(a)), it can be seen that the f-CNT also pyrolyzed more rapidly than the p-CNTs, suggesting that they have lower thermal stability, possibly due to the presence of oxygenated surface groups and higher defect density. Note that the analysis was performed in N₂ atmosphere, so this difference cannot be imparted on the reactivity of the oxygen-containing groups but only structure of the nanotubes at the molecular level. So, this difference may be also the reason why the bonding with the polymer is not so effective with f-CNTs.

Interestingly, the addition of THF in the fabrication of the composites through the solution mixing method, apparently did not have a negative impact on the polymer-CNT bondings, as can be seen from the TG curve of the PDMS/p-CNT-THF 1% sample, which is almost the same as the PDMS/p-CNT-BM sample.

The derivatives of the curves in Figure 5.2 were also determined to compare the temperatures at the highest rates of decompositions that were observed for each samples, shown in Figure 5.3. From this graph, it seems more clear that the onset of the region of instability of the composites is retarded in comparison with PDMS, but varies in each sample. The PDMS/p-CNT 1% appeared to be the most stable composites.

In general, from these results it could be concluded that there are effective interactions between the PDMS matrix and the nanotubes, resulting in an enhancement of the thermal stability of all

Results and Discussion

the composites.

Table 5.3: Total percentage mass loss of the samples obtained as the final mass loss divided by the initial mass.

Sample	% Mass loss
p-CNT	2.0
f-CNT	4.0
PDMS	60.1
PDMS/p-CNT wt%	48.1
PDMS/p-CNT 1 wt%	31.4
PDMS/p-CNT-BM 1 wt%	35.7
PDMS/f-CNT-BM 1 wt%	58.9
PDMS/p-CNT-THF 1 wt%	39.7

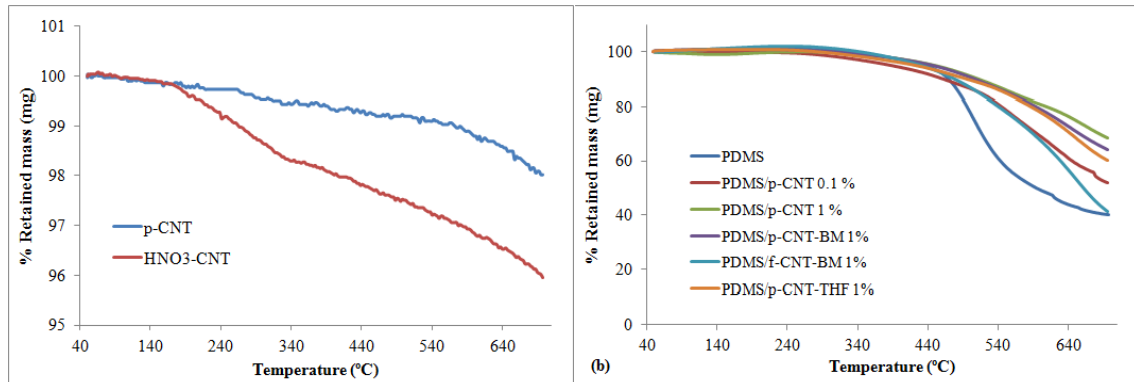


Figure 5.2: Thermogravimetric spectra of the: (a) pristine CNTs (p-CNT) and functionalized CNTs (HNO₃ – CNT) samples; (b) PDMS, PDMS/p-CNT 0.1 wt%, PDMS/p-CNT 1 wt%, PDMS/p-CNT-BM 1 wt%, PDMS/f-CNT-BM 1 wt% and PDMS/p-CNT-THF 1 wt% samples.

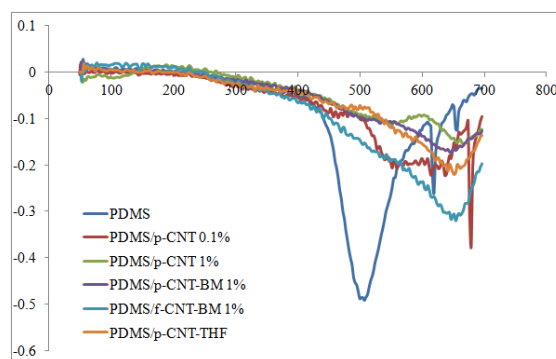


Figure 5.3: Thermogravimetric spectra of the derivative of the PDMS, PDMS/p-CNT 0.1 wt%, PDMS/p-CNT 1 wt%, PDMS/p-CNT-BM 1 wt%, PDMS/f-CNT-BM 1 wt% and PDMS/p-CNT-THF 1 wt% samples.

Results and Discussion

5.2.3 Temperature Programmed Desorption

The results of the TPD analysis are presented in Fig. 5.4 and Table 5.4.

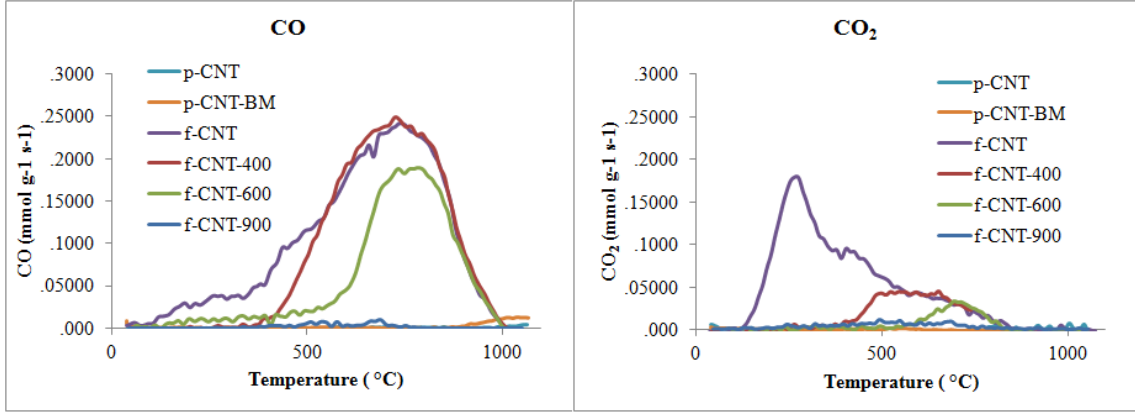


Figure 5.4: TPD results: (a) CO and (b) CO₂ spectra of the p-CNT, f-CNT, f-CNT-400, f-CNT-600, f-CNT-900 and p-CNT-BM samples.

Table 5.4: Results of the TPD analysis of the f-CNT, f-CNT-400, f-CNT-600 and f-CNT-900 samples.

Sample	$m_{CO} (\mu\text{mol g}^{-1})$	$m_{CO_2} (\mu\text{mol g}^{-1})$
p-CNT	0	0
p-CNT-BM	0	0
f-CNT	1171	566
f-CNT-400	1013	153
f-CNT-600	661	67
f-CNT-900	22	45

Table 5.5: List of the functional groups released from the oxidized CNTs and the temperature range at which they typically decompose. Values adapted from [8].

Chemical group	Temperature range	Gas released
Carboxilic	100 - 400 °C	CO ₂
Lactone	190 - 650 °C	CO ₂
Phenol	600 - 700 °C	CO
Carbonyl	700 - 980 °C	CO
Anhydride	400 - 600 °C	CO and CO ₂
Ether	700 °C	CO
Quinone	700 - 980 °C	CO

From the curves shown in Figure 5.4-(a) it can be concluded that the CO₂-containing groups are released from the surface in the temperature range below 400 °C (first peak) and that further heating of the sample causes the other groups to be gradually released until 900 °C, at which point

Results and Discussion

all the CO₂-containing groups have been purged from the nanotubes' surface. Regarding CO-containing groups, it can be seen in Figure 5.4-(b) that these components are decomposed at higher temperatures. The curves obtained for the f-CNT and f-CNT-400 samples are in good agreement with results previously reported using the same type of CNTs and the same functionalization procedure with nitric acid and heat treatment at 400 °C, respectively [107]. The amount of CO and CO₂ gases released from the samples reflects the amount of oxygenated groups present at their surfaces, which in turn depends on the type of treatment they received. The HNO₃-CT sample is the one with highest surface density of groups, and thus is also the most acidic one since it was not submitted to heat treatment. The f-CNT-400, f-CNT-600 and f-CNT-900, on the other hand, show significantly less density of surface groups, with decreasing amount of groups with increasing temperature of the heat treatment. This result was expected since the heat removed most of the groups introduced with the acid treatment. The spectra of the pristine CNTs with or without ball milling treatment showed no surface groups at all, as expected. These results are in good concordance with the ones previously reported [106, 107]

In the analysis previously done on the TPD spectra of activated carbon samples functionalized with the same procedure as in this work, the TPD curves were decomposed through deconvolution methods with multiple gaussian functions to yield the underlying components of the spectra [8], each component corresponding to a chemical group, such as carboxylic acids, lactones, carbonyl groups, anhydrides and quinones. The temperatures at which each of these groups are decomposed are presented in Table 5.5 for clarity.

Here, the same analysis can be applied by observing the evolution of the curves and therefore see if the same components as the ones previously reported can also be present in these samples. The CNTs that were heat-treated showed a significant loss of surface groups, so only the HNO₃ sample can be inspected. From the CO₂ spectra of the f-CNT sample, it seems that the first peak appears at 260 °C, corresponding to the decomposition of carboxilic acids, while the second local peak is located around 420 °C and therefore possibly corresponds to anhydrides. In the CO spectra of the same sample, the first component appears centred around 500 °C, thus corresponding to carboxylic anhydrides and phenols; the second peak, and maximum of the curve, is located around 700 °C and so corresponds to carbonyl groups.

This analysis is important to understand the surface chemical composition in terms of functional groups of the treated CNTs and their percentage coverage. This has an influence on the interaction between the functionalized CNT and the PDMS polymer matrix, since the interactions established by the functional groups and the PDMS chains are easier than the ones provided by the bare CNT surface.

5.2.4 Fourier Transform Infrared Spectroscopy (FTIR)

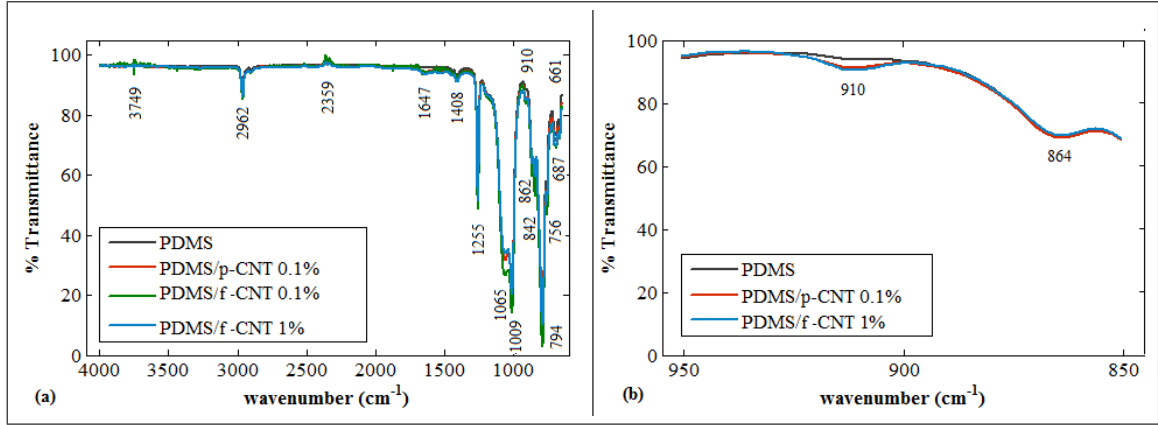


Figure 5.5: (a) ATR-FTIR spectrum of PDMS, PDMS/p-CNT and PDMS/f-CNT composite membranes, taken between 650 and 4000 nm; (b) High resolution ATR-FTIR spectra of PDS, PDMS/p-CNT and PDMS/f-CNT composite membranes, between 650 and 950 nm.

The FTIR spectra shown in Figure 5.5 represents all the characteristic peaks of the PDMS product used, with a morphology comparable to literature data [121]. From Figure 5.5, it can be noted that the spectra of the pristine PDMS and the CNT/PDMS composite are all identical, with no visible characteristic peaks of the CNTs. The CNT characteristic peaks are located in the range 900 - 3500 cm⁻¹, with strong peaks defined around 1200, 1402, 1550, 1700 and 3444 cm⁻¹ [122, 123].

As reported, the functionalized CNTs, when compared with the pristine CNTs, present accentuated peaks at 1200, 1500 and 1700 cm⁻¹, associated with the C=O stretching, and at 1200, corresponding to C–O stretching, of the -COOH groups [123]. A peak at 3500 cm⁻¹, corresponding to the -OH stretching frequency, and at 1365 cm⁻¹, the CH mode of vibration, have also been reported [26].

From the comparison of the spectra of the three samples, it is evident that they are all identical. A reason pointed out to explain this fact is that the CNTs are all mainly embedded deep inside the matrix, being covered by a layer of PDMS which impedes the IR light to excite the nanotubes. The penetration depth of the IR laser depends on the wavelength of the excitation light, the angle of incidence (in this case, 90 °) and refractive indexes of the prism and sample, but typical values are from 0.1 to a few micrometers [124]. This means that the CNTs are probably even below that level. However, when both sides of the membranes were used for the analysis, identical spectra were obtained, which shows that the CNTs were completely embedded inside the bulk of the membranes, and not exactly deposited at the bottom. This may suggest that PDMS tends to engulf the nanotubes by forming cross-linked networks around them in order to minimize steric repulsions. On the other hand, CNTs suffer some form of re-aggregation after the shear force of the mixing process is removed. So, it is also possible that a certain amount of re-aggregation caused the CNTs to migrate towards the bulk of the membranes.

Results and Discussion

5.2.5 Contact Angle Measurements

According to the thermodynamic theory, if ΔG is positive, the surface is hydrophilic, and otherwise, if it is negative, the surface is hydrophobic and a negative energy of adhesion with *E. coli* indicates that cell adhesion is a favourable process.

The data from the contact angle measurements, shown in Figure 5.6 and in Table 5.6 revealed that all the surfaces produced retained the hydrophobic character of PMDS. But in general the surface with p-CNTs showed a slightly more hydrophobic character than the ones with f-CNTs. This result is in good accordance with the chemical nature the CNTs used. The pristine CNTs are very hydrophobic, thus raising the overall hydrophobicity of the composite, whereas the funcitonalized CNTs have an acidic character, and thus are more hydrophilic.

The fact that the two of the most hydrophobic surfaces are the ones with the highest content of pristine CNTs is not surprising given the hydrophobic nature of these nanotubes. But it would be expectable that these two surfaces had a greater hydrophobicity than the the PDMS/p-CNT 0.1% surface, contrary to what was obtained. The most likely explanation for this result is that the value of the surface energy determined through this method is very sensitive to small errors in the measurements, since the values are still quite close.

Interestingly, the PDMS/f-CNT 0.1% coating had a highly negative value of surface energy, but oppositely a positive energy of adhesion with *E. coli*, the highest of all samples, corresponding to highly unfavourable interaction between both.

When the nanotube content is 1 wt%, the impact on surface hydrophobicity follows the same tendency, with pristine CNTs increasing hydrophobicity with respect to pure PDMS and functionalized CNTs having the opposite effect, regardless of surface roughness. Note that that the surface with ball milled (BM) CNT has significantly less roughness. This is in keeping with the thermodynamic theory, since it only takes into account the van der Waals and the hydrophobic interactions arising from chemistry of the surface.

Regarding the adhesion energy with *E. coli*, Figure 5.6 indicates that the adhesion is more favourable (more negative) for the p-CNT 0.1% surfaces, with the p-CNT 1%, f-CNT 1% and p-CNT-BM 1% surfaces have slightly less favourable but similar adhesion energy. Finally, the results show that the only two surfaces with positive energy of adhesion (and therefore less favourable *E. coli* adhesion) were PDMS and PDMS/f-CNT 0.1%.

Results and Discussion

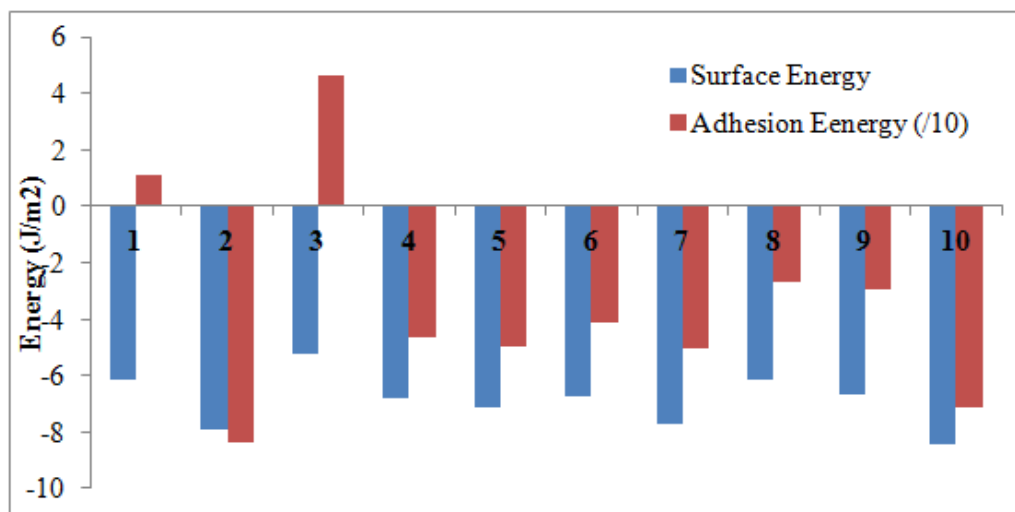


Figure 5.6: Surface free energy and adhesion energy of: 1 - PDMS; 2 - PDMS/p-CNT 0.1%; 3 - PDMS/p-CNT 0.1%; 4 - PDMS/p-CNT 0.1%; 5 - PDMS/p-CNT 1%; 6 - PDMS/f-CNT 1%; 7 - PDMS/p-CNT-BM 1%; 8 - PDMS/f-CNT-BM 1%; 9 - PDMS/p-CNT-THF 1%; 10 - PDMS/f-CNT-THF 1%. Values of adhesion energy were divided by a factor of 10 for better visualization.

Table 5.6: Surface free energy and energy of adhesion with *E. coli* cell of each surface tested, calculated as described in chapter 3.

Sample	$ \Delta G_s^{LW} $	$ \Delta G_s^{AB} $	$ \Delta G_s^{tot} $	$ \Delta G_{ad}^{AB} $	$ \Delta G_{ad}^{LW} $	$ \Delta G_{ad}^{tot} $
PDMS	-2.9	-58.8	-61.7	-2.3	3.4	1.1
PDMS/p-CNT 0.1%	-0.72	-78.1	-78.8	-10.6	2.2	-8.4
PDMS/f-CNT 0.1%	-2.5	-50.0	-52.4	1.5	3.2	4.6
PDMS/p-CNT 1%	-1.2	-70.2	-71.4	-7.2	2.2	-5.0
PDMS/f-CNT 1%	-0.64	-67.0	-677	-5.8	1.6	-4.2
PDMS/p-CNT-BM 1%	-3.2	-73.8	-77.1	-8.6	3.6	-5.0
PDMS/f-CNT-BM 1%	-0.1	-61.5	-61.7	-3.4	0.8	-2.7
PDMS/p-CNT 0.5%	-0.40	-67.46	-67.9	-4.7	-5.9	1.3
PDMS/p-CNT-THF 1%	-1.2	-65.7	-67.0	-3.0	-5.2	2.3
PDMS/f-CNT-THF 1%	-4.3	-80.1	-84.5	-7.1	-11.3	4.2
After 30 minute degradation assay with citrate buffer in dynamic conditions						
PDMS	-2.5	-77.0	-79.4	-10.0	3.2	-6.8
p-CNT/PDMS 0.1%	-6.77	-66.0	-72.8	5.4	5.3	-0.1
f-CNT/PDMS 0.1%	-3.68	-74.5	-78.2	-8.9	3.9	-5.1

5.2.6 UV-Vis Spectroscopy

Degradation assays were performed to monitor the stability of the material under specific conditions over time. In this particular study, degradation assays of the composite coatings were carried

Results and Discussion

out both in citrate buffer, the medium used in PPFC adhesion assays, and synthetic urine. Since these materials were envisioned for biomedical applications as for example in the urinary tract, it would be of interest to study the effect of urine in the coating.

The results of the UV-Vis analysis of the immersion liquids are shown in Figure 5.7. The spectra shown were obtained by performing a baseline correction with the corresponding medium, either citrate buffer or synthetic urine.

The tests with citrate buffer revealed an increasing absorbance in the UV range. Note that UV-Vis spectra of PDMS reported in the literature has also shown a common tendency of absorption in the UV [113], and CNTs have also significant absorption in these wavelengths [125, 126]. Comparing the citrate buffer spectra at days 1, 4 and 8, there is no difference for all the samples, except in the UV region, with the spectra showing the highest and lowest absorbance at days 4 and 8, respectively. But since this trend is observed for all samples, it can be concluded that this is most likely due to the effect of baseline correction, which varied for each day. The more accentuated absorbance in the UV region at day 4 probably results from a higher saturation of the baseline, and not to the presence of any substances, since these are not observable at day 8.

Since the static degradation assays were performed in sterile conditions in a flow chamber, this absorbance pattern is unlikely to be the result of light absorption by contaminants. The results with synthetic urine, on the other hand, show a peak in the near UV zone, which can not be directly related with the present of PDMS or CNTs residues. However, the absorbance properties of the both materials could have been altered by the chemical or physical interactions between matrix and filler.

Unlike the spectra obtained with citrate buffer, urine showed prominent peaks in the UV range, which suggests that urine may have a stronger effect on the chemical stability of the composite coatings. This observation is not surprising since synthetic urine has a rather complex composition, containing several reactive components. It does not seem likely that the driving force of the observed effect is the pH of the solution, since the synthetic urine used had a pH of 6.5 while the citrate buffer had a pH of 5. The ionic force of the medium, on the other hand, is more likely the primary factor causing the interactions with the surfaces and possible degradation.

Relating these results with the CA measurements performed on the degradation assays with the PPFC, which revealed no significant alterations of the contact angles, it seems that the citrate buffer solution has a minimum impact on surface stability after a short period of time, even under non-static flow, and also that it does not cause swelling of the PDMS. This may suggest that, on one hand, the low shear rate used in this assay is not an important parameter in the chemical degradability of the composites, but the exposure time may be more critical. The cross-linking density is also an important parameter influencing the chemical stability of a polymer, and even though a high weight fraction of base polymer to curing agent was used for the preparation of the materials (10:1), a less uniform mixing of the two parts may result in some areas having a lower cross-linking density, and therefore being more susceptible to degradation.

Results and Discussion

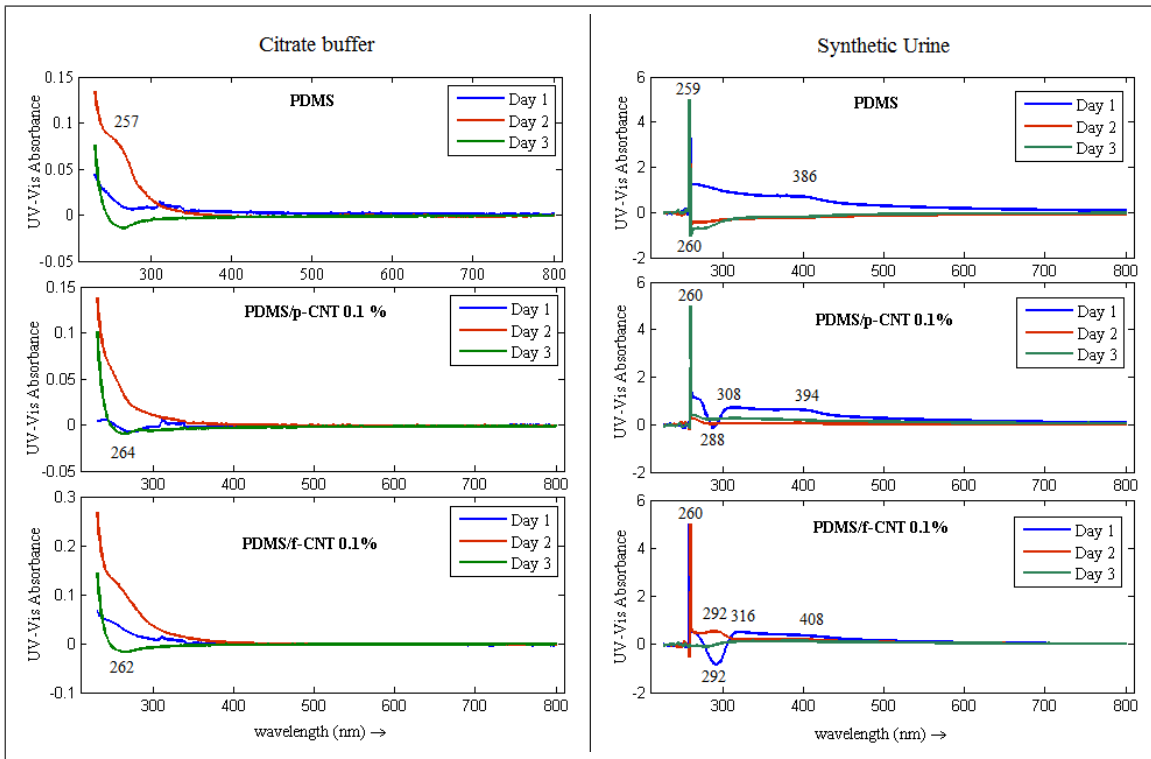


Figure 5.7: UV-Vis spectra of the citrate buffer solution (left side) and synthetic urine (right side) after 1, 4 and 8 days of immersion with the PDMS, PDMS/p-CNT 0.1% and PDMS/f-CNT 0.1% samples.

5.2.7 X-Ray Photoelectron Microscopy (XPS)

XPS analysis was performed to evaluate the chemical composition of the surface of the PDMS, PDMS/p-CNT 0.1%, PDMS/f-CNT 0.1%, PDMS/p-CNT 1%, PDMS/f-CNT 1%, PDMS/p-CNT-BM 1% and PDMS/f-CNT-BM 1% samples. The C-1s, O-1s and Si-2p peaks present in the XPS spectrum of PDMS correspond to the methyl and Si-o groups, respectively.

The results of the XPS analysis, presented in Table 5.7, show that the atomic percentages of the C, O and Si elements at the topmost nanometres of the surface were about 50%, 25% and 25%, respectively, which agrees with the stoichiometry of PDMS chains.

The XPS spectra obtained was similar to what has been previously reported [127, 23, 62]. However, it could be noted that the C-1s, O-1s and Si-2p peaks of the composite spectra did not seem to evidence significant differences in C-C and C-O bondings. Besides, deconvolution of the C-1s and O-1s peaks did not indicate a suggest a tendency of growing C-C content with the introduction of CNTs as well as C-O content in the f-CNTs.

These observations may be justified by the fact that XPS only analyses the up to 3 nanometres inside the surface, which is a very shallow depth. Therefore, this analysis indicated that most of the nanotubes were probably located below this level. Also, note that this technique is very

Results and Discussion

localized, and so may yield results that are not representative of the whole surface if the sample is not perfectly uniform, which was the case.

Table 5.7: Elemental atomic percentages (At%) of carbon, oxygen and nitrogen at the surface of the coatings.

Element (At%)	C-1s	N-1s	O-1s	Si-2p
PDMS	48.90	ND	26.15	24.96
PDMS/p-CNT 0.1%	48.38	ND	26.68	24.94
PDMS/f-CNT 0.1%	48.66	ND	25.96	25.37
PDMS/p-CNT-BM 1%	50.10	ND	25.56	24.34
PDMS/f-CNT-BM 1%	49.35	ND	25.89	24.76
PDMS/p-CNT 1%	49.31	ND	25.81	24.88
PDMS/f-CNT 1%	48.97	ND	26.62	24.41

5.2.8 Scanning Electron Microscopy (SEM)

SEM images showed that PDMS coatings had a rather flat surface, with no visible roughness or irregularities. The PDMS/p-CNT 0.1 % and PDMS/p-CNT 0.1 % coatings also revealed a very flat surface but with some minor protuberances, probably due to CNTs or entrapped bubbles. The PDMS/p-CNT 0.1 % and PDMS/f-CNT 0.1 %, however, presented some CNTs aggregates covered in PDMS protruding out of the surface. These observations agree with the macroscopic observations of the surfaces. Figure 5.8 shows some of the SEM images where the nanotubes were visible, although it should be noted that these images are not representative of the surface, since the majority of the surface area of the samples were devoid of topographical features.

The samples were fractured along the width and images of the cross-sections were also analysed. From the analysis of the cross-sections, the CNTs seemed to have a tendency to deposit on the bottom of the coating, but it would have been expected that the CNTs were closer to the surface and more uniformly distributed along the depth of the coating. PDMS displayed a clean fracture, with not visible deformation of the polymer (Figure 5.9-(a)), the composite coatings all showed rather irregular fractures covered in debris (Figure 5.9-(b)). This suggests that the presence of CNTs within the polymer possibly caused the tensile stress applied during the fracture to nucleate at the spots where the CNTs were bond to PMDS due to their higher stiffness. This may have caused the PDMS chains to deform under the applied load before the CNTs fractured.

Figures 5.8-(a) and -(b) show the cross-section of the PDMS/p-CNT 1% fracture and a close-up, respectively, where a CNT aggregate that has been cut in half can be seen. Note the presence of some nanotubes sticking out of the surface, indicating that the nanotubes in the core of the aggregate fractured in non-specific locations of the tubes, possibly at the defects where the structure is more fragile.

For each sample, ten images of the cross-section were taken and the corresponding thickness measured to obtain the their average thickness. Values are shown in Figure 5.10. These results

Results and Discussion

indicate that the coatings all had an average thickness between 25 and 27 μm , except the PDMS/p-CNT-BM 1% and PDMS/f-CNT-BM 1% coatings which presented a thickness of about 47 μm . This difference can be explained by the fact the former were spin coated during 60 s, while the other two during 30 s. Besides, the higher standard deviations of the measurements agreed more or less well with the observed roughness of each sample, with the PDMS/p-CNT 1% having the largest variation.

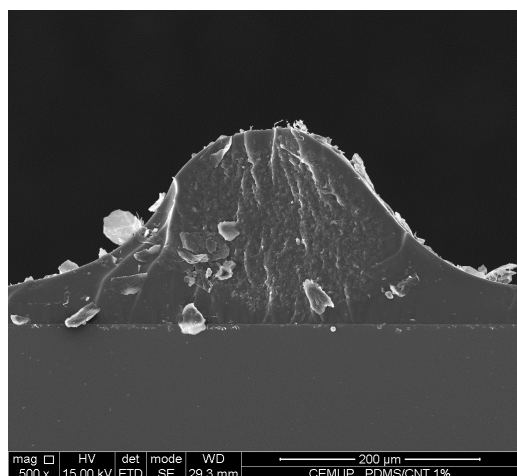
SEM images of the PDMS/p-CNT-THF 1% coating showed a flat surface with no visible roughness at the micro- and nano-scale, although these coatings were more irregular at a macro-scale.

Regarding the double-layer composite coatings, both the PDMS/p-CNT in SDS PDMS/f-CNT in SDS samples seemed to have higher surface roughness, especially at the micro-scale. At some points where the layer of PDMS had ripped it was possible to visualize the underlying mat of deposited CNTs (see Figure 5.9).

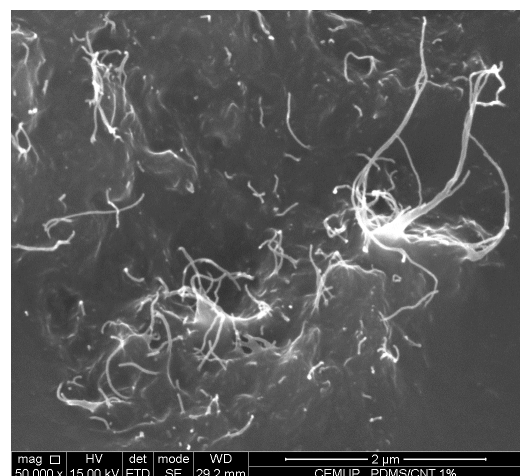
Interestingly, this layer of nanotubes was well embedded in an amorphous mass of sodium and sulphur, as indicated by local EDS analysis, left behind when the volatile component of the SDS evaporated. Despite that, the CNTs seemed to be well dispersed. Interestingly, the PDMS/p-CNT in THF sample showed a surface patterned with sub-micron-sized prominent aggregates, but the PDMS/f-CNT in THF sample did not, presenting a very planar surface with only a few larger aggregates.

The results from the EDS analysis showed that the overall elemental composition of the various surfaces was about 50% C, 25% O and 25% Si, the same as PDMS, as was obtained also from XPS analysis. However, when a more localized analysis was performed to compare two distinct zones, a flat zone and one containing a CNT aggregate underneath revealed a slightly higher content of C, with differences of about 11.7% and 12.3% for a CNT loading of 0.1 wt% and 1 wt%, respectively, with the atomic percentage of C in the global analysis falling midway between these two extreme values. Since EDS has a depth of analysis in the range 1 μm to 3 μm , greater than that of XPS, it is no surprise that it revealed more significant differences.

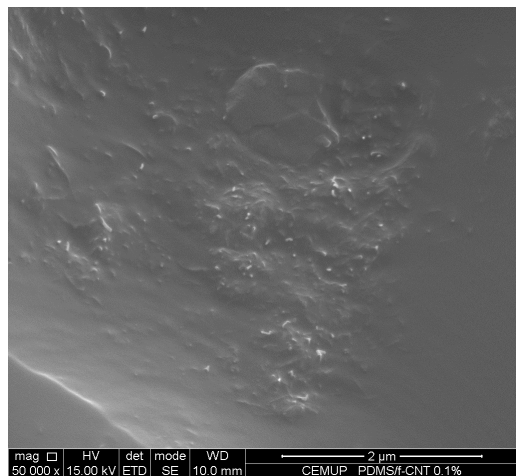
Results and Discussion



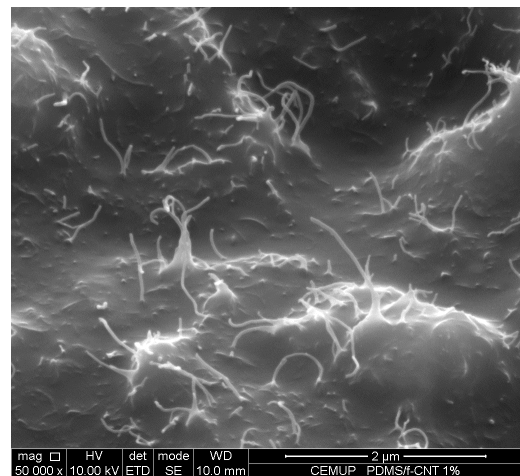
(a) PDMS/p-CNT 1 wt%.



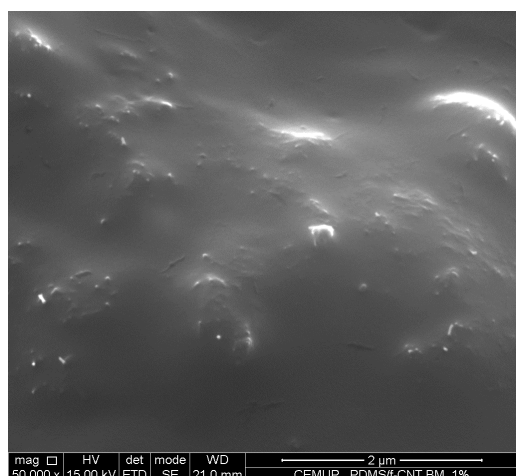
(b) PDMS/p-CNT 1 wt%.



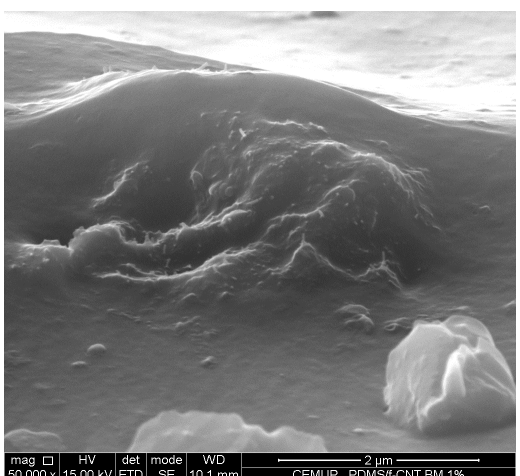
(c) PDMS/f-CNT 0.1 wt%.



(d) PDMS/f-CNT 1 wt%.



(e) PDMS/f-CNT-BM 1 wt%.



(f) PDMS/f-CNT-BM 1 wt%.

Figure 5.8: SEM images of the surfaces of the PDMS/p-CNT 1 wt%, (a) and (b); PDMS/p-CNT 0.1 wt%, (c); PDMS/f-CNT 1 wt%, (d); and (e) PDMS/f-CNT-BM 1 wt%, (e) and (f), coatings.

Results and Discussion

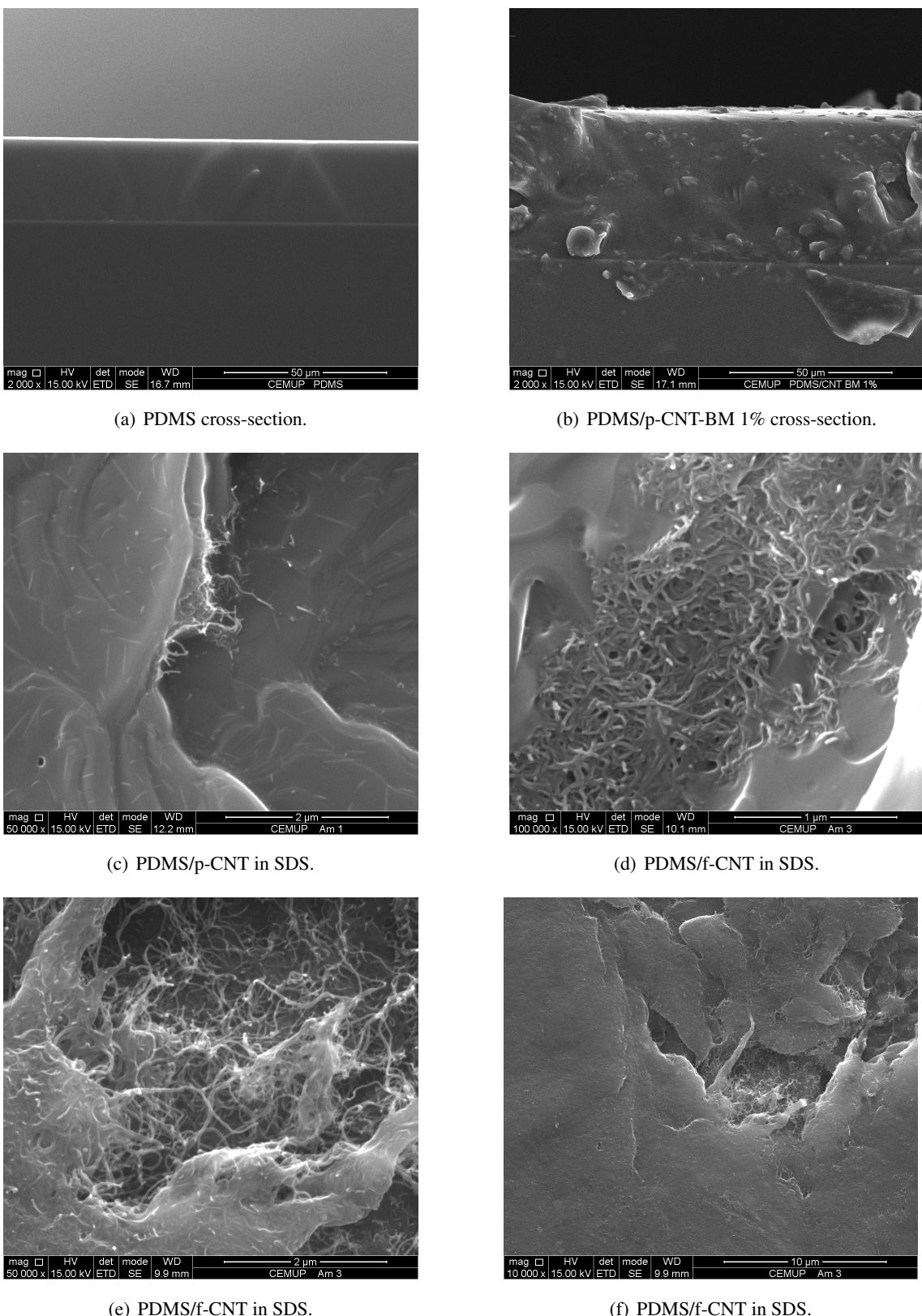
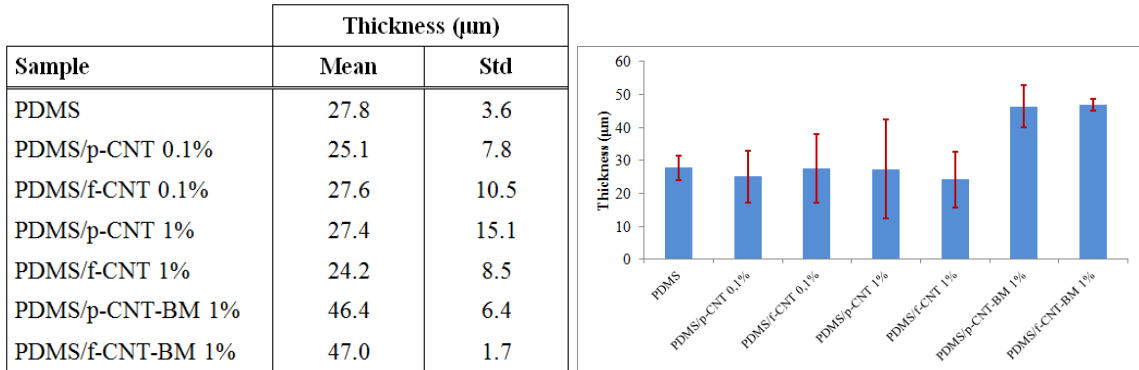


Figure 5.9: SEM images of the PDMS (a) and PDMS/p-CNT-BM 1% (b) cross-sections; PDMS/p-CNT in SDS (c) and PDMS/f-CNT (d) to (f) in SDS surfaces of the coatings (magnification, 2000x; scale).

Results and Discussion



(a) Table with the values of thickness determined for each sample from SEM images (mean and standard deviation (Std)).

(b) Bar chart of the same values.

Figure 5.10: Mean values of thickness of each sample thickness determined from SEM images represented in table (a) and bar chart (b) form.

5.2.9 Atomic Force Microscopy (AFM)

Atomic Force Microscopy (AFM) was used to obtain a 3-dimensional profile of the surface of the analysed samples and characterize their surface topography. Only the PMDS, PDMS/p-CNT 1% and PDMS/f-CNT 1% were analysed, since the others had not presented many topographical features from the SEM images. The profiles of the PDMS/p-CNT 1% and PDMS/f-CNT 1% surfaces are presented in Figure 5.11, showing the topography of CNT agglomerates. The PDMS surface was completely flat.

Note that the aggregates in the two surfaces appeared to have different morphologies, but since this analysis was very localized, no further considerations can be derived.

5.2.10 Conductivity Measurements

Electrical characterization was performed in order to determine the conductance of the different composite samples by taking DC voltage - current (V-I) measurements. The results of the DC conductivity measurements for each sample calculated from the current-voltage curves are shown in Figure 5.12-(a) and -(b).

Results and Discussion

Table 5.8: DC characteristic curves os the different composite coatings measured in a specified voltage interval (-1 to 1 Volt or -100 to 100 Volt).

Sample	Conducatnce (S)
Glass	$0.15 \cdot 10^{-11}$
PDMS	$0.31 \cdot 10^{-11}$
PDMS/p-CNT 0.1 %	$0.12 \cdot 10^{-11}$
PDMS/f-CNT 0.1 %	$0.19 \cdot 10^{-11}$
PDMS/p-CNT 1 %	$0.19 \cdot 10^{-11}$
PDMS/f-CNT 1 %	$0.13 \cdot 10^{-11}$
PDMS/p-CNT-BM 1 %	$0.13 \cdot 10^{-11}$
PDMS/f-CNT-BM 1 %	$0.14 \cdot 10^{-11}$
PDMS/p-CNT-THF 1 %	$0.15 \cdot 10^{-4}$
PDMS/f-CNT-THF 1 %	$0.69 \cdot 10^{-6}$
PDMS/p-CNT in SDS	$0.32 \cdot 10^{-2}$
PDMS/f-CNT in SDS	$0.12 \cdot 10^{-2}$
PDMS/p-CNT in THF	$0.19 \cdot 10^{-3}$
PDMS/f-CNT in THF	$0.81 \cdot 10^{-3}$

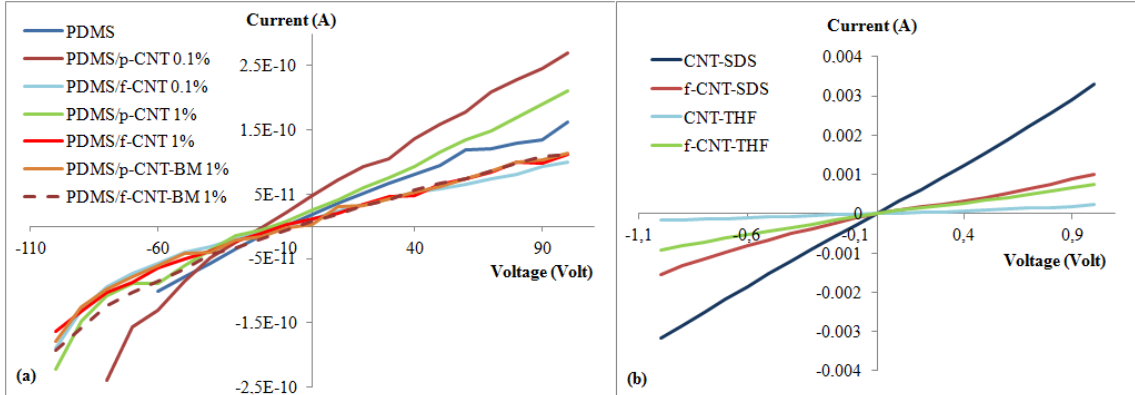


Figure 5.12: (a) Conductance curves of the glass, PDMS, PDMS/p-CNT 0.1%, PDMS/f-CNT 0.1%, PDMS/p-CNT 1%, PDMS/f-CNT 1%, PDMS/p-CNT-BM 1% and PDMS/p-CNT-BM 1% samples measured from -100 Volt to +100 Volt; (b) (a) Conductance curves of the CNT-SDS, f-CNT-SDS, CNT-THF, f-CNT-THF samples measured from -1 Volt to +1 Volt. Values are in Siemans.

In previous studies, these CNTs have already shown to be conductive and to effectively enhance the conductivity of a polymer composite [128].

The results revealed that the composites produced by the bulk mixing process, PDMS/p-CNT 0.1%, PDMS/f-CNT 0.1%, PDMS/p-CNT 1%, PDMS/f-CNT 1%, PDMS/p-CNT-BM 1% and PDMS/f-CNT-BM 1%, did not exhibit any increase in electrical conductivity, as can be seen from

Results and Discussion

the very low conductance values, which were all of the same order of magnitude as that of PDMS. This fact indicates that the CNTs in these samples were not well-enough dispersed to establish a percolative path for the current to flow with the CNT concentrations used.

However, the PDMS/f-CNT-THF and PDMS/p-CNT-THF samples with 1 wt% showed a significant increase in electric conductance by 5- to 7-fold, respectively, which indicates that even at CNT concentrations as low as 1%, there is an enhancement in conduction driven by their better dispersion in PDMS.

The double-coating layers presented the highest conductances, reaching increased values of 9 and 8 orders of magnitude for the coatings produced with SDS and THF, respectively, with values as high as 0.01 S achieved. This suggested that the nanotubes dispersed in SDS then in THF and deposited by solvent evaporation could form electrical contacts, with SDS yielding better results. Moreover, this also indicated that this type of coating shows better performance for practical applications. These results are not surprising since these coatings also have a much higher wt% of CNTS than the others, so an effective conduction path is formed.

Additionally to their higher conductivity, these samples also showed a more linear behaviour, crossing the origin, typical of ohmic conductors, although the measurements were taken in a narrower range of voltage. But the non-linear curves displayed on Figure 5.12-(a) can be explained by the accumulation of charge at the surface of PDMS.

Note that, the values of conductance presented here are an extrinsic properties of the materials, that is, they depend on the cross-sectional area and form factor of the samples. So, these values cannot be directly interpreted as being high or low, but can only be comparable among them, since all samples were measured in the same way. Note also that the PDMS layer covering the nanotubes acts as an insulating layer, hampering the measurements of current flowing through them, which explains why conductances of different orders of magnitude (10^{-2} and 10^{-3} S) were obtained. Thus, thicker top-layers of PDMS yielded lower values of conductance.

Results and Discussion

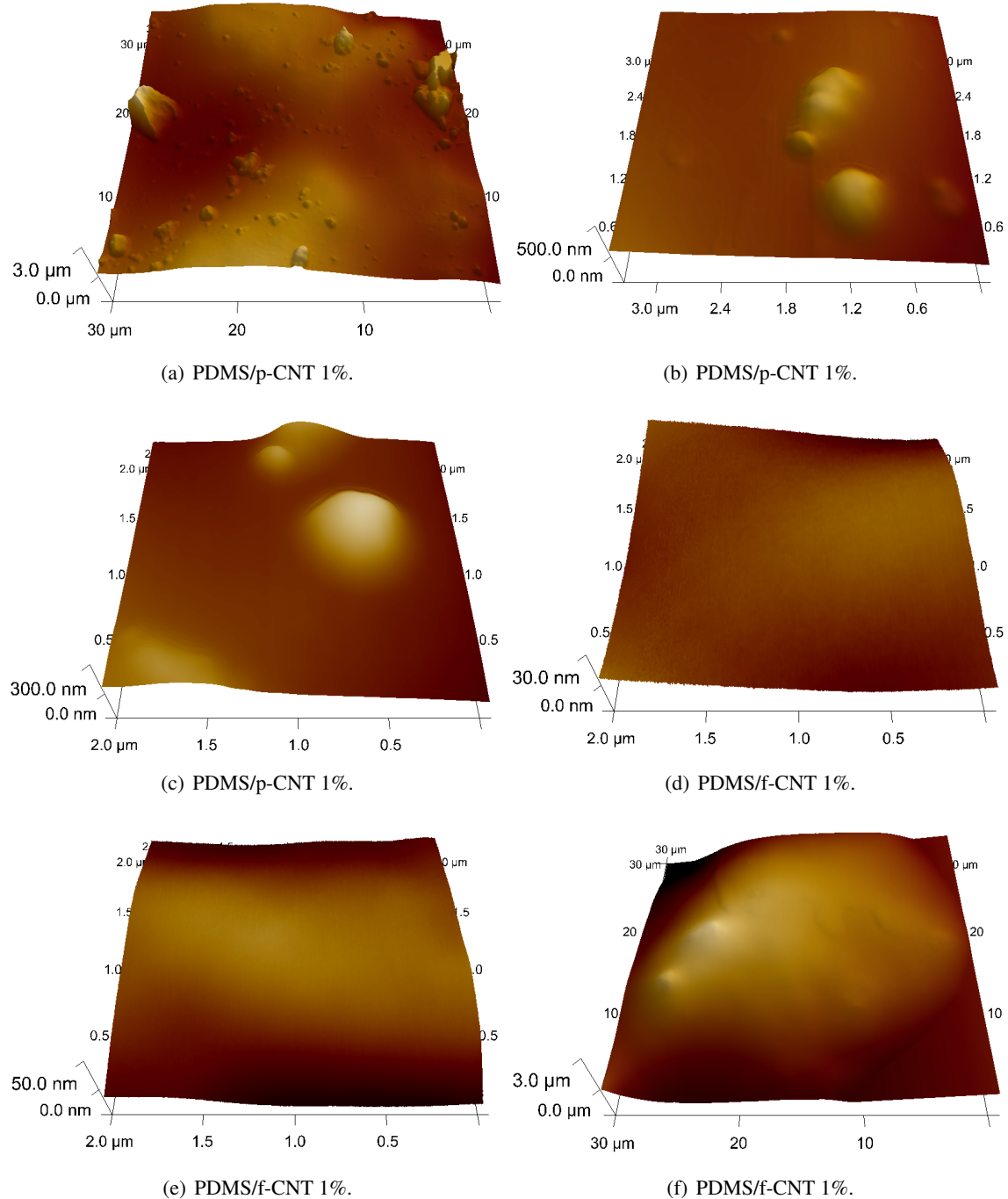


Figure 5.11: AFM images of the PDMS/p-CNT 1% ((a) to (c)) and PDMS/f-CNT 1% ((d) to (f)) coatings showing three different zones with distinct roughness.

Results and Discussion

5.3 Bacterial Adhesion

5.3.1 Kinetic Cell Countings

This section presents the results of the kinetic cell adhesion assays carried out using the method described in section 4.4.3 with the PDMS (control), CNT/PDMS 0.1 wt% and f-CNT/PDMS 0.1 wt% coatings. For each type of coating, 3 independent tests were done and for each repeat 12 non-overlapping subregions of the image were analysed for statistical analysis. The kinetic curves in Figure 5.14 represent the average number of adhered cells for the three repeats over the 12 subregions as a function of time (total run time of 30 minutes with 30 seconds time intervals). These values were corrected to the number of adhered cells or deposited particles at initial time instant for comparison purposes. The number of adhered cells at the final instant were then compared among the different coatings and the results are presented in table 5.9 and in the bar graph of Figure 5.13. Appendix B includes supplementary material of the adhesion assays.

Table 5.9: Values of cell densities calculated from the previous Table and normalized to an area of approximately $4.9 \cdot 10^5 \mu\text{m}^2$ and respective Adhesion rates. Values are in cells $\mu\text{m}^2 \cdot 10^{-5}$ and in $\mu\text{m}^2 \cdot \text{min}^{-1} 10^{-5}$, respectively.

Sample	Test 1	Test 2	Test 3	Mean	Adhesion Rate
PDMS	64	69	72	68 ± 4	2.6 ± 0.1
PDMS/p-CNT 0.1%	54	61	69	62 ± 7	2.2 ± 0.2
PDMS/f-CNT 0.1%	60	73	85	73 ± 13	2.8 ± 0.5

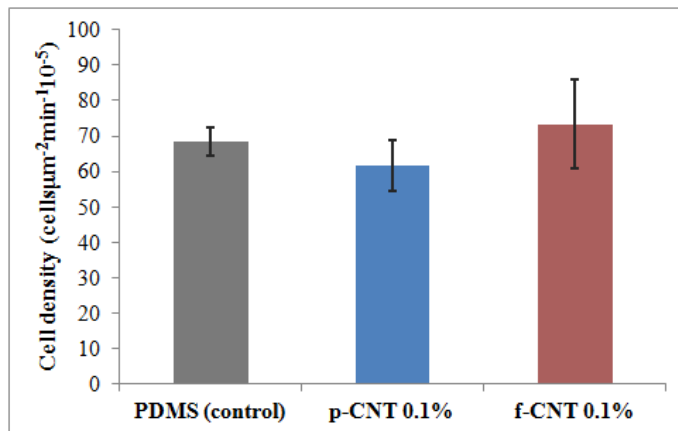


Figure 5.13: Bar chart of the average cell densities in the PDMS (black bar), PDMS/p-CNT 0.1% (blue bar) and PDMS/p-CNT 0.1% (red bar) coatings, obtained with three independent tests. Error bars correspond to standard deviation.

Results and Discussion

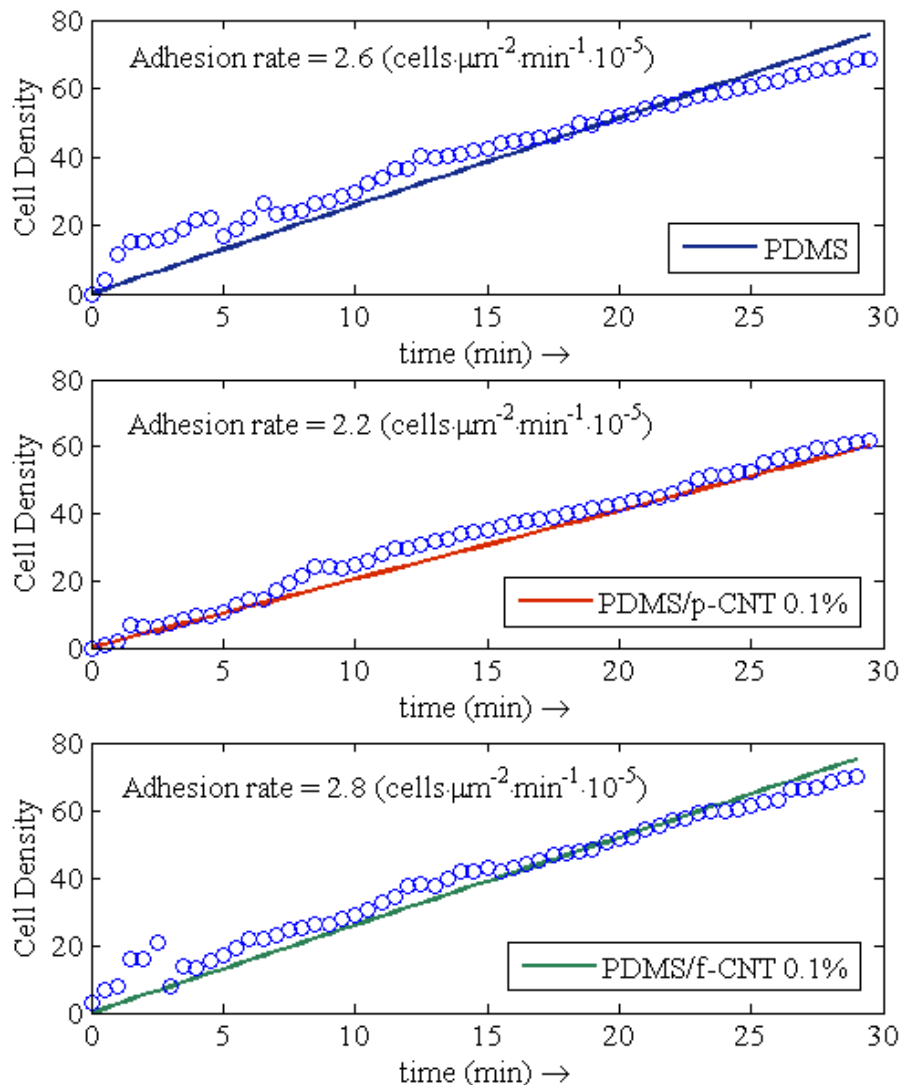


Figure 5.14: Graphic of mean cell adhesion kinetic curves in the three samples: PDMS, p-CNT/PMDS 0.1% and f-CNT/PMDS 0.1%.

The results in Table 5.9 of the on-line adhesion show that although there seems to be a slight difference in the bacterial adhesion among the three samples tested, PDMS, PDMS/p-CNT 0.1 wt% and PDMS/f-CNT 0.1 wt%, but not statistically different (one-way ANOVA test, $p>0.05$).

The initial adhesion rates were well correlated with the corresponding values of cell density, which indicates that there was a steady adhesion tendency along the assays and it was the rate of adhesion that dictated the final number of cells adhered. Furthermore, in Figure 5.14 it can be seen that the adhesion regime was perfectly linear, with no saturation effects.

Results and Discussion

5.3.2 End-point Cell Countings with DAPI staining

The cell countings in these samples were performed with the DAPI staining method described in (section 4.4.4) because it was not possible to determine the cell adhesion kinetic curves through image analysis since the images had too many artefacts and interference from the CNT and darkened background to allow for accurate image segmentation. Example images of the various coatings are presented in Appendix C to illustrate this fact.

The results of the cell countings obtained with this method are summarized in Table 5.10 and shown more explicitly in Figure 5.15. These data show that the highest adhesion was obtained with the PDMS and PDMS/f-CNT-THF 1% coatings, followed by PDMS/f-CNT-BM 1%. In order to evaluate the results obtained with the two methods, the various cell counting values were normalized to the visualized area.

Although there were no statistical differences among the samples (one-way ANOVA test, $p>0.1$), in general, it seemed that there was a tendency for cells to adhere more to p-CNTs than to f-CNTs, which was maintained when the CNT concentration was raised to 1%, both with the BM treated CNTs and with the CNTs dispersed in THF. Moreover, the surfaces containing p-CNTs seemed to show decreased adhesion with increasing CNT content, which may suggest that the concentration of CNTs might be a factor in the inhibition of adhesion. However, regarding the coatings with the f-CNTs, it seems that increasing CNT content promoted slightly less adhesion in the PDMS/f-CNT 1% coating, an effect that is not present in the PDMS/f-CNT-BM 1% and PDMS/f-CNT-THF 1% coatings. The major difference between them is the degree of dispersion of the nanotubes and their structure. Although the differences were not statistically meaningful, considering that the coatings with p-CNTs and f-CNTs at 0.5 and 1 wt% had higher surface roughness it may be possible that this fact is also having a slight impact on cell adhesion.

As for the PDMS/f-CNT-THF 1% sample, although it could not be verified whether or not the CNTs were more close to the surface, they seemed to be better dispersed in the matrix, as could be seen from their uniform opacity and the results of electrical conductivity measurements. So, the slight differences in cell adhesion verified in these samples might suggest that CNT dispersion is another parameter whose influence would be worth investigating further.

An overall comparison of the results is shown in the bar graph of Figure 5.16, where the values of cell density for each surface were normalized to the cell density of the control (PDMS) of the corresponding cell counting method. So, the values shown in this bar chart correspond to percentage of relative adhesion (RA). Letters A and B refer to the groups of values of RA that were statistically different (one-way ANOVA test, $p<0.05$). From these results it can be seen that the two groups with statistically different RA also correspond to the cell densities obtained with the two different methods, also bearing very different between-groups variances, which could have been the cause of that statistical difference.

Results and Discussion

Table 5.10: Cell densities of the end-point adhesion assays of the p-CNT/PDMS 1%, f-CNT/PDMS 1%, p-CNT/PDMS 0.5%, p-BM/PDMS 1% and f-CNT-BM/PDMS 1% coatings with DAPI staining. The results were obtained for two independent tests, Test 1 and Test 2. Values correspond to mean \pm standard deviation of the total cell counting divided by the area of the field of view, $4.7 \cdot 10^3 \mu\text{m}^2$. Values are in cells $\mu\text{m}^{-2} \cdot 10^{-4}$.

Sample	Test 1	Test 2	Test 3	Mean
PDMS	57	47	-	52 ± 7
p-CNT 0.5%	44	37	36	39 ± 4
p-CNT 1%	32	19	38	30 ± 10
f-CNT 1%	30	57	42	43 ± 14
p-CNT-BM 1%	49	32	-	41 ± 12
f-CNT-BM 1%	61	34	-	48 ± 19
p-CNT-THF 1%	28	34	-	31 ± 4
f-CNT-THF 1%	64	40	-	52 ± 17

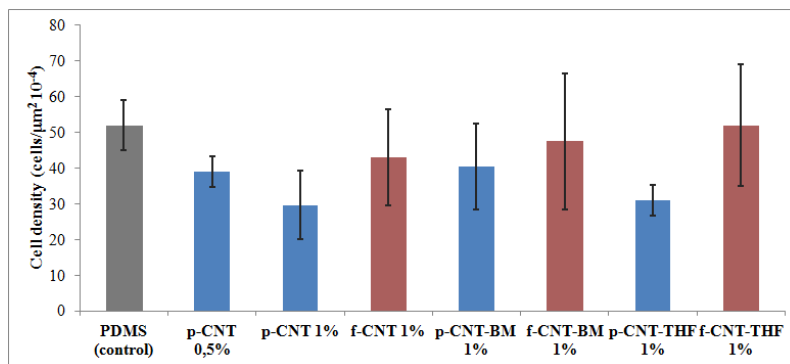


Figure 5.15: Bar graph of end-point cell adhesion countings of the various surfaces containing pristine CNTs (p-CNT, blue bars) and functionalized CNTs (f-CNT, red bars) at 0.5 and 1 wt% with or without ball milling treatments (BM) or dispersed with THF.

Note that, when comparing the cell densities obtained through image analysis of the on-line adhesion assays and the ones obtained with DAPI staining, there is a difference in the values of one order of magnitude. It should be pointed out that One possible reason behind these fact is that DAPI the stained images revealed some artefacts resultant from DAPI residues and other particles lodged at the surface. Moreover, quenching occasionally occurred.

The fact that the results of adhesion energy measurements and of the cell adhesion assays were not very concordant may be partially due to the thermodynamic theory of adhesion used in these work not being the most appropriate methodology to draw significant conclusions about the interactions between *E. coli* and these composite surfaces. This issue had already been pointed out in chapter 3, when the results seems to be in agreement.

Another important remark is that since the p-CNTs and f-CNTs have a point-of-zero charge around 7.0 and 3.0, respectively, as mentioned in section 4.1. So, any CNTs popping out of

Results and Discussion

the surface could be interacting with the citrate buffer, which at a pH of 5, inducing changes of the surface charge density by forming an electrical double-layer. The p-CNTs do not have surface groups, but when they are inside the citrate buffer, which has lower pH, their π electrons will tend to protonate with the water molecules, thus creating a positively charged layer at the interface. However, in an aqueous medium with lower pH than the f-CNTs, the acidic groups, mainly the carboxylic groups tend to be deprotonated resulting in an increase in negative surface charge density [129]. This fact will affect the electrostatic forces at the interface of the coatings and thereby alter their surface energy. The negative charges at the surface thus create repulsive forces acting on the *E. coli* cells, which also have negative net surface charge, resulting in less adhesion. Since *E. coli* cells also have net negative charge, this effect should be considered when CNTs are introduced at the surface. However, from the results obtained, where the coatings with f-CNTs showed more adhesion than the ones with p-CNTs, that effect did not seem to be dominant in the surfaces tested.

Even though cell adhesion tests in combination with contact angle measurements were not conclusive, some important conclusions may be derived. There were in fact slight changes of surface hydrophobicity and roughness with the introduction of the four different types of CNTs (pristine and functionalized, and with or without milling treatment) that might have elicited different cell adhesion responses. Besides, there are possibly two effects influencing cell adhesion: the change in surface hydrophobicity induced by the presence of the CNTs in the bulk of the material, allowing one to tune the surfaces to have more or less adhesion; and the surface roughness and conversely the availability of CNTs at the interface, which might be used to have functionalized CNTs without further increasing the amount of cell adhesion. So, in the end, there might be a combined effect of the two properties that is the driving force for producing CNT composite surfaces with cell adhesion-modulation capacity.

Finally, it is important to note that there are several other factors that influence *E. coli* adhesion on surfaces. For example, *E. coli* has a flagellum which gives it the ability to stick to the surface penetrate into the electric double-layer at the interface [130], influencing their adhesion capacity in a way that is not accounted for in any common theory of adhesion [131]. This emphasizes the fact that cell adhesion is a phenomenon far more complex than what can be evaluated with the present work, but the objective was to gain some insight into the applicability of a framework in the study of carbon nanotube-based composite surfaces.

In order to more deeply assess the cell fouling behaviour on these type of composite coatings, further characterizations and cell adhesion tests would be required. Besides, the present work was only focused on evaluating the initial adhesion, but biofilm formation assays would also be important for the clarification of the effect of the surface properties on the long-term attachment and proliferation mechanism of the cells. For example, it could be the case that even with no significant difference in the number of cells initially adhered, the surface properties could have other effects on the inhibition of cell matrix production that would affect biofilm formation.

Results and Discussion

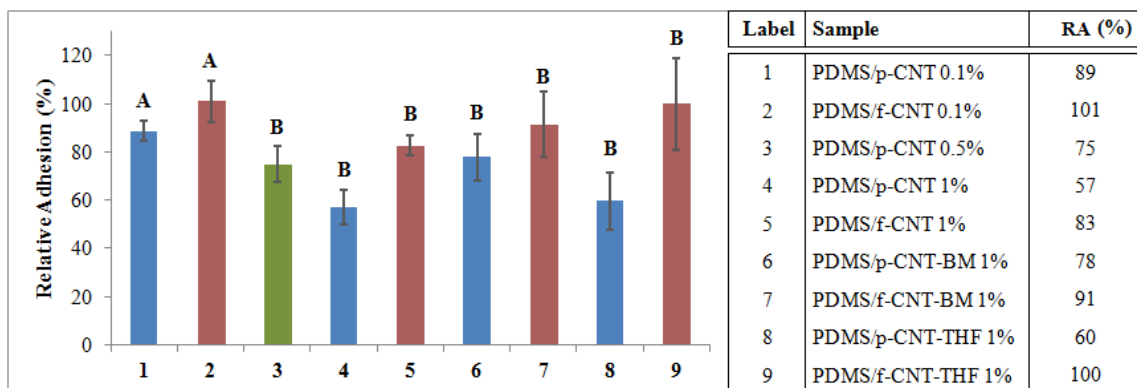


Figure 5.16: Relative adhesion (RA) values for pristine CNTs (p-CNT, blue bars) and functionalized CNTs (f-CNT, red bars) at 0.1 and 1 wt% with or without ball milling treatments (BM) and for p-CNT at 0.5 wt% (green bar). The table on the right side indicates the surfaces corresponding to each numerical label on the bar chart. All surfaces were produced by the bulk mixing method except those produced with solution mixing (CNT/THF). Values were calculated by dividing cell countings obtained for a certain surface by those obtained with PDMS (control). Letters A and B indicate groups of mean values with statistically different RA (one-way ANOVA test, $p>0.05$).

Results and Discussion

Chapter 6

Conclusions and Future Work

Carbon nanotube composite materials with varying nanotube characteristics and using different dispersion methods were prepared and the materials characterized with appropriate techniques. Thermal, structural and chemical properties of CNTs and of the composites were analysed by TG, N₂ isotherms and TPD, respectively. Thin film of the prepared composites were coated onto glass slides using spin coating and spreading methods. The surface hydrophobicity of the fabricated surfaces was estimated through the contact angle method compared among the different coatings.

Bacterial adhesion assays using *Escherichia coli* as model organism were performed in steady state flow conditions using a flow cell with a shear stress of 0.01 Pa for better mimicking the hydrodynamic conditions inside the human body. Both on-line and end point adhesion assays were conducted depending on the optical transparency of the coatings, yielding separate sets of results with independent control tests.

Conductivity measurements were conducted on the coatings to assess whether the surfaces developed in this work presented enough conductivity for sensory and similar applications.

Degradation assays were also performed to test for the chemical stability of the composite coatings in contact with citrate buffer and synthetic urine either in dynamic and static flow conditions.

XPS, SEM, AFM and FTIR analysis were used to evaluate the over efficiency of dispersion of the CNTs inside the polymer matrix and the possible mechanisms influencing the dispersion state of the nanotubes.

The results showed that a good dispersion of CNTs was only possible with mechanical treatment of the nanotubes and aggressive sonication. Microscopy and SEM images showed that even after that CNT aggregates still remained in the bulk of the composites, but with much smaller dimensions.

TG analysis showed an enhancement of the thermal stability of the composites comparing to pure PDMS, suggesting that effective bondings between CNTs and polymer chains were established, but the strength of these bonds depended also on the functionalization of the nanotubes.

Conclusions and Future Work

TPD analysis revealed that the CNTs were successfully functionalized and that different acidic groups were introduced on the surface, which could be observed from the selective and progressive removal of CO and CO₂ content in the different samples. N₂ adsorption isotherms indicated that structural changes were induced by the oxidation and heat treatments and ball milling from the increased surface areas of the nanotubes when compared to the pristine ones.

Contact angle measurements of the 0.1 wt% CNT loading composites suggested that the introduction of CNTs in the polymer matrix had a slight effect on its surface hydrophobicity, with the pristine CNTs increasing its hydrophobic character and the functionalized CNTs decreasing it. All composite surfaces, except the PDMS/f-CNT 1%, showed a theoretical increase in the adhesion energy with *E. coli*.

The bacterial adhesion assays revealed two statistically different groups of samples, those with 0.1 wt% loading of CNTs and the remainder samples, but these two groups correspond to the two different cell counting methods.

Although there were not statistically significant, there was a tendency of a higher number of *E. coli* cell to adhere to the composite coatings with the functionalized CNTs rather than with the pristine CNTs, which might be explained in terms of surface hydrophobicity.. Surprisingly, there was less cell adhesion when the CNT loading was increased from 0.1 to 1 wt%. This may have been partially caused by the increased surface roughness induced by re-aggregation of the CNTs during the spin coating, even though the CA measurements did not show a significant difference in surface hydrophobicity. Since all these samples had similar surface morphologies (yet different from the PDMS/p-CNT 1% and PDMS/f-CNT 1 % surfaces), this seems to suggest that the surface roughness, and having nanotubes closer to the surface, might also have an effect on cell adhesion.

The PDMS/p-CNT-THF 1% and PDMS/f-CNT-THF 1% surfaces also showed the same tendency of decreased cell adhesion with p-CNTs and otherwise with f-CNTs. In these two composites, the difference between both, however, was slightly more accentuated. Note that, since the CNTs were better dispersed in these samples, it may be the case that any possible effect induced by the nanotubes being closer to the interface becomes more dominant. However, it has been suggested in other works that p-CNTs may be more adherent to bacteria then f-CNTs.

It is important to realise that when it comes to adhesion with biological systems there are many parameters to be considered and most theories fail to provide accurate predicts due to the complexity of the biological models used.

Morphological and chemical analysis of the composites with SEM, XPS and FTIR suggested that there was a tendency of CNTs to be deposited on the substrate rather than evenly distributed throughout the depth of the coatings. This observation may indicate that the spin coating procedure used is not well suitable for preparing composite coatings where it is desirable to have the CNTs at the surface. This result also provides an explanation for why no major differences in surface hydrophobicity and cell adhesion were obtained with the introduction of the CNTs in the 0.1 wt% composite surfaces.

Electrical conductivity measurements showed that the introduction of either 0.1 wt% or 1 wt% of CNTs in the PDMS with the bulk mixing method was not sufficient to increase its electrical

Conclusions and Future Work

conductivity. Microscopy and SEM observations confirm this fact, since the images showed that the CNTs were still considerably bundled in small clusters and these aggregates were too separated to establish a percolative path across the matrix. However, the PDMS/p-CNT-THF and PDMS/f-CNT-THF samples showed an increase in electrical conductance by 7 and 5 orders of magnitude, respectively, confirming that a better dispersion of the nanotubes had been achieved with the solution mixing process. The double-layer composite coatings, in turn, showed a remarkable increase in electrical conductance, reaching increases of 9 and 8 orders of magnitude for the ones produced with SDS and THF, respectively. This suggested that the nanotubes were better dispersed in SDS than in THF. This is not surprising since the bottom layer of the coating consisted on CNTs deposited by solvent evaporation, so the nanotubes not only were more uniformly distributed but also the CNT surface densities achieved were higher. It was also noted that electrical measurement were hindered by the insulating PDMS layer which impeded an effective electrical contact between CNTs and measurement equipment.

The degradation assays suggested that the composite coatings remained stable when in contact with a citrate buffer solution both in static and steady-state flow conditions. The results of the degradation with synthetic urine were not conclusive and further tests ought to be conducted to clarify this point.

This work allowed to conclude that there seems to be an effect in both the bulk and surface properties of PDMS with the introduction of CNTs, which showed an overall slight tendency to decrease adhesion of *E. coli* cells. This effect also seemed to be slightly more accentuated with p-CNTs than with f-CNTs. The results with the surfaces containing 0.1 wt% of CNTs were statistically different from the ones obtained with the composites containing 1 wt%, suggesting that the CNT concentration may be an important factor. However, the difference in these two groups of results may have been induced by the implementation of different procedures for the cell countings. The two surfaces with p-CNTs and f-CNTs at 0.1 % were not significantly different from PDMS, possibly indicating that such a low concentration of nanotubes, plus the fact that they were mostly deposited at the bottom of the coating, is not sufficient to induce any relevant cell adhesion response. Although most of the adhesion results not statistically different, the small variations in the results may suggest that the CNTs might have other effects on cell adhesive properties of the surfaces other than their hydrophobicity, there is more than one effect of the nanotubes in the cell adhesion response, such as their textural properties and dispersion degree. Plus, the enhanced electrical behaviour of some of the composites may find interesting applications in the future in the implant industry once the biological interactions with these surfaces are fully understood.

Additionally to the techniques and methods presented in this work, there are still many other possibilities that were not explored due to the limited amount of time available to develop this work. Some of these possible future work is described in this section.

Conclusions and Future Work

In order to define possible applications for the developed materials, a more complete assessment their properties could be done. For instance, Dynamic Mechanical Analysis would be important to evaluate the mechanical stability, respectively, and therefore provide further information regarding the bonding strength between CNTs and PDMS chains and extent of interconnectivity. Another technique useful for such a purpose would be swelling measurements of the composites, since the extent of swelling of PDMS depends on its cross-linking density, and therefore, a variation of swelling with the introduction of CNTs would be indicative of whether or not CNTs were acting as cross-linking agents.

Similarly, the double-layer composites should also be tested for adhesion since these composites were the ones that showed the greatest promise for conductive coatings, although their applications are more limited than the other coatings because of the complexity of their production and anchorage of the CNTs onto the substrate. Obtaining SEM images of these coatings would also be interesting to assess their surface roughness and if the CNTs were more well integrated inside the matrix.

Another important point that would be worth further investigation is the electrical conductivity of the composites. Firstly, the conductivity tests should have been done using silver paint in the electric contacts to enhance the impedance coupling between the samples and the probes, thus minimizing the losses, which was not possible. That fact might have underestimated the values of conductance obtained. On the other hand, in the present work only DC conductivity measurements were performed, but this type of test provides very limited information regarding the conductive behaviour of the materials. Polymeric composite materials by nature exhibit more complex electric responses than the other classes of materials, since polymers are dielectrics and therefore have a complex impedance. Several parameters can be measured using the impedance spectroscopy technique introduced in chapter 2, namely, dielectric constant, complex conductivity and admittance. The determination of these parameters is very important for electronic applications, such as sensors and electrodes.

From the observations of cells attached to the CNTs, it would be interesting to perform Live/Dead assays to evaluate if the nanotubes were having any kind of antimicrobial effect on the cells as described in chapter 2, even though these CNTs were embedded in the surface and not flowing in a suspension.

To better understand the results of cell adhesion obtained, more tests should be conducted with other CNT concentrations, for example, 5 wt % and 10 wt%, and using the f-CNTs with thermal treatment, which were not employed due to a lack of time. As previously stated, the Thermodynamic theory of adhesion is not the most accurate for biological systems since it does not account for electrostatic forces of the medium. So, calculations of the adhesion energy could be done based on the XDLVO theory in order to better correlate the surface energy with the results of bacterial adhesion. Besides, the influence of the surface charge of *E. coli* in citrate buffer could be assessed by measuring its the zeta potential and performing the same adhesion assays with other media. Moreover, testing composites with other CNT loadings for electrical conductivity would also allow determining the percolation threshold, a characteristic of major importance when envisioning

Conclusions and Future Work

conductive composites with minimal filler loading possible. Besides, from the experimental critical exponent of the percolation function also gives an insight into the interactions between matrix and filler and thus the dispersion state of the particles.

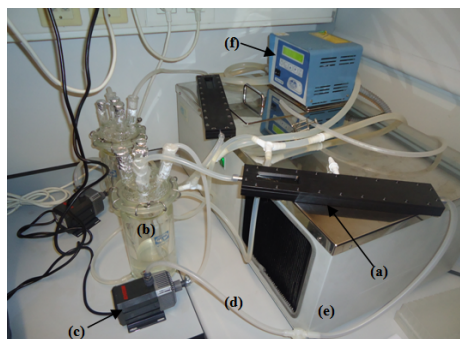
Finally, as previously mentioned in chapter 5, the degradation assays suggested that there might be some extent of degradation with synthetic urine, so it would be advantageous to further investigate this result using other analytical techniques, such as FTIR or chromatography to determine the possible chemical composition of the substances released, as well as testing longer degradation times.

Conclusions and Future Work

Appendix A

Experimental Set-up

Figure A.1 shows photographs of the experimental set-up and equipment used in the cell adhesion assays.



(a) Experimental set-up: (a) flow Cell; (b) reactor; (c) centrifugal pump; (d) tube; (e) variable valve; (f) water bath.



(b) Parallel-plate flow cell.



(c) Reactor.



(d) Centrifugal pump.

Figure A.1: Photographs of the experimental set-up.

Experimental Set-up

Appendix B

Cell Adhesion Assay

This appendix presents the kinetic adhesion curves of the three repeats of the PDMS, PDMS/p-CNT 0.1 % and PDMS/f-CNT 0.1 % surfaces (Figure B.1), as well as some representative microscopy images taken in the cell adhesion assays and used for the cell countings and the kinetic adhesion curves (Figure B.2). DAPI images are also presented (Figure B.3).

Cell Adhesion Assay

B.1 Kinetic Adhesion Curves

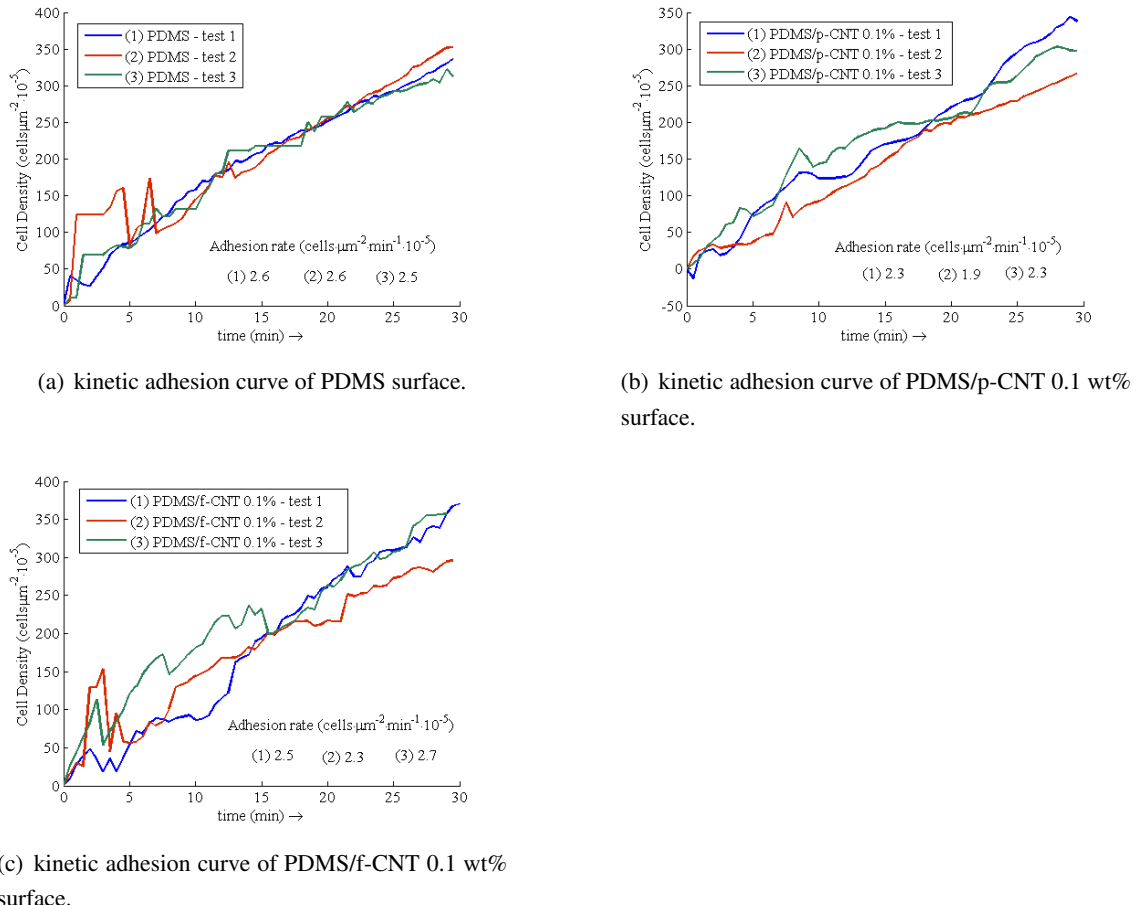


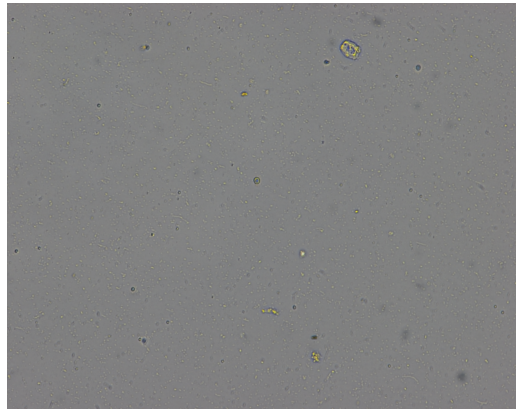
Figure B.1: kinetic adhesion curves obtained with the on-line adhesion assays.

B.2 Microscopy images

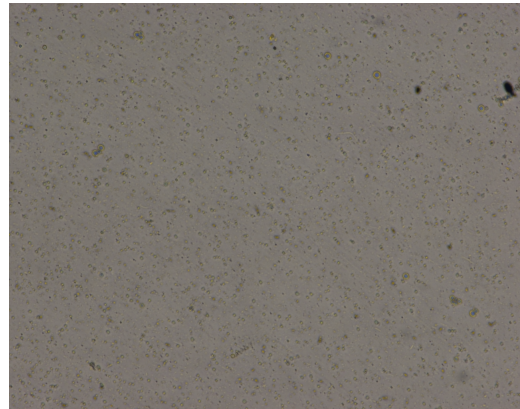
Representative images (Figures B.2 and B.3) of the various different composite coatings after the cell adhesion assays used for the cell countings are presented in this section.

Cell Adhesion Assay

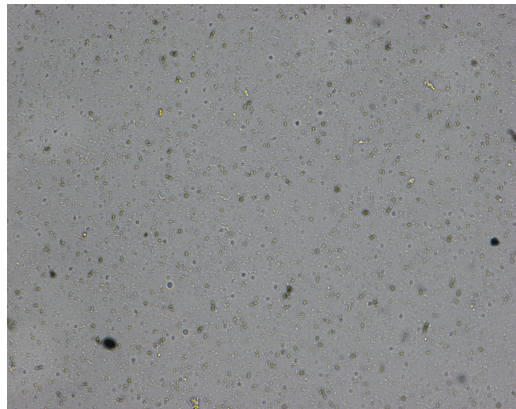
B.2.1 Optical Microscopy



(a) PDMS



(b) PDMS/p-CNT 0.1 wt%



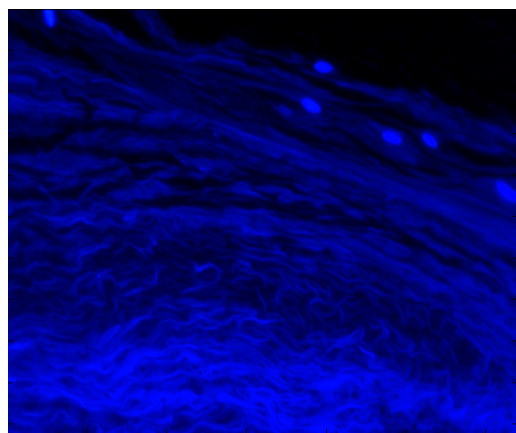
(c) PDMS/f-CNT 0.1 wt%

Figure B.2: Microscopy images of the various composite coating surfaces with adhered *E. Coli* after a 30 minute on-line adhesion assay visualized at the optical microscope (Nikon eclipse V100; magnification, 10x). These images were used for off-line image analysis to determine the number of cells adhered at each surface.

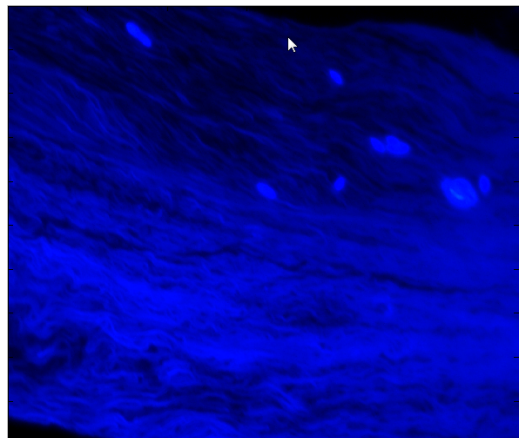
B.2.2 Fluorescence Microscopy

Fluorescence microscopy images of *E. coli* cells at the surface of the PDMS/p-CNT-THF 1% coating.

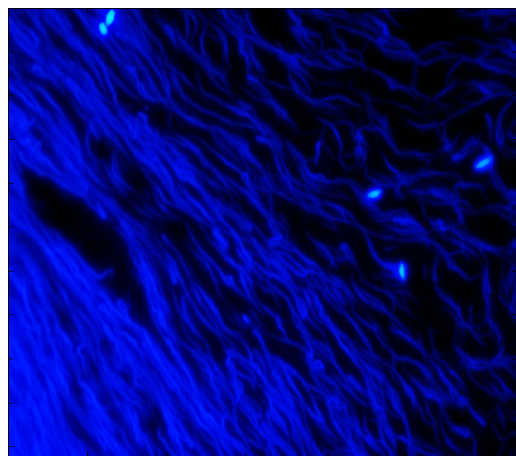
Cell Adhesion Assay



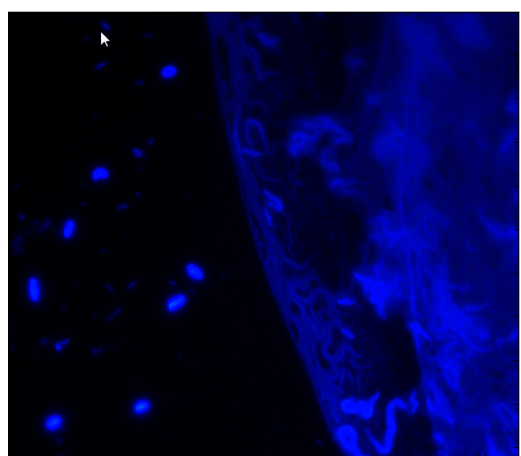
(a) Region 1.



(b) Region 2.



(c) Region 3.



(d) Region 4.

Figure B.3: Fluorescence microscopy images with DAPI staining of the PDMS/p-CNT/THF composite coating surface with adhered *E. coli* after a 30 minute adhesion assay (magnification, 10x).

Appendix C

CNT/PDMS composite coatings

In this appendix contains photographs and optical microscopy images (Nikon Eclipse LV100; magnification, 10x) of the inner structure of the various fabricated CNT/PDMS coatings which allows the visualization of the distribution of the CNTs inside the matrix and their dispersion state.

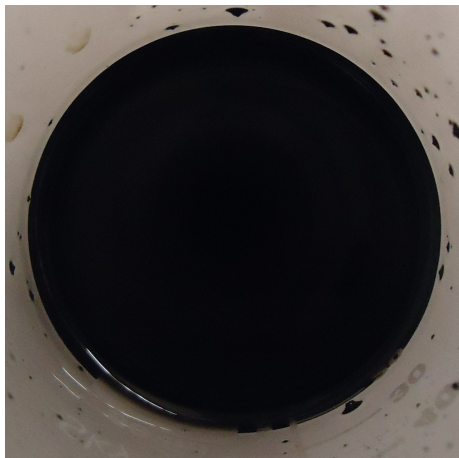
CNT/PDMS composite coatings



(a) PDMS/p-CNT 0.1 wt% composite before shear mixing.



(b) PDMS/p-CNT 0.1 wt% composite before shear mixing.



(c) PDMS/p-CNT 0.1 wt% composite before shear mixing.

Figure C.1: Photographs of the PDMS/p-CNT 0.1 wt% composite in three different processing stages.

CNT/PDMS composite coatings

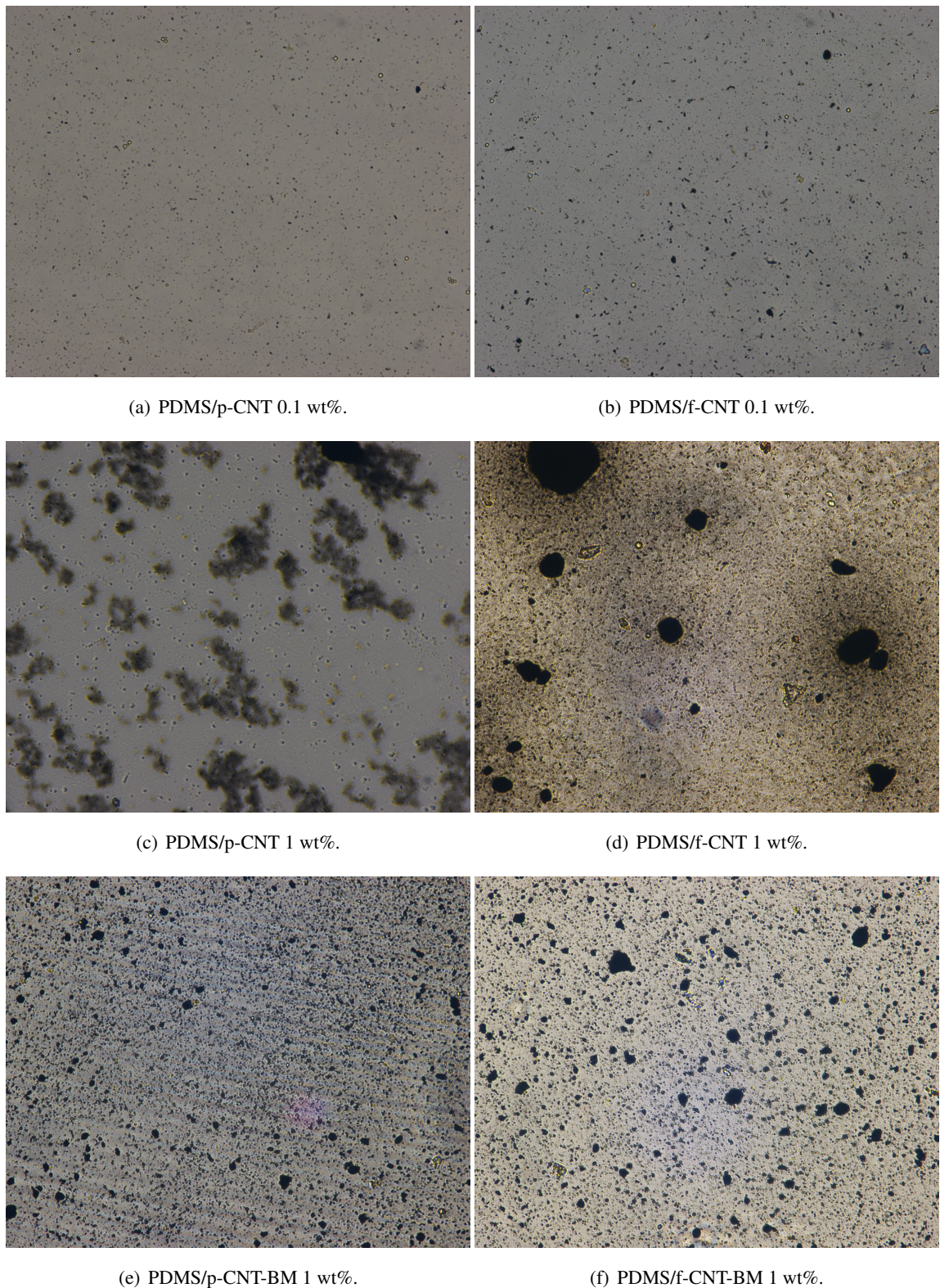


Figure C.2: Microscopy image of the various composite coatings in a bulk focal plane (magnification, 10x).

CNT/PDMS composite coatings

Appendix D

Adhesion Energy Calculations

This appendix includes the values of contact angle (CA) measured directly on the fabricated surface with the sessile drop method (Table D.1) and the intermediate calculations of the surface free energy (table D.3) and energy of adhesion with *E. coli* (Table D.4) determined from the equations of the Thermodynamic theory of adhesion presented in chapter 3. Table D.2 presents the experimental values of the surface tension of the test liquids (water, formamide and 1-bromonaphthalene), reported elsewhere [9].

Table D.1: Contact angles measurements of the different coatings (mean value \pm std error).

Sample	Water	Formamide	1-Bromonaphthalene
PDMS (Control)	$115.8^\circ \pm 1.3^\circ$	$114.7^\circ \pm 1.9^\circ$	$87.6^\circ \pm 1.8^\circ$
PDMS/p-CNT 0.1wt%	$122.0^\circ \pm 0.9^\circ$	$113.6^\circ \pm 1.5^\circ$	$77.2^\circ \pm 0.8^\circ$
PDMS/f-CN 0.1wt%	$111.7^\circ \pm 0.4^\circ$	$110.4^\circ \pm 0.8^\circ$	$86.1^\circ \pm 1.6^\circ$
PDMS/p-CNT 1wt%	$117.0^\circ \pm 0.7^\circ$	$110.4^\circ \pm 0.8^\circ$	$80.4^\circ \pm 0.7^\circ$
PDMS/f-CNT 1wt%	$116.6^\circ \pm 0.6^\circ$	$111.1^\circ \pm 0.5^\circ$	$76.6^\circ \pm 1.5^\circ$
PDMS/p-CNT-BM 1wt%	$121.5^\circ \pm 0.3^\circ$	$115.7^\circ \pm 0.4^\circ$	$88.8^\circ \pm 0.9^\circ$
PDMS/f-CNT-BM 1wt%	$113.6^\circ \pm 0.4^\circ$	$109.1^\circ \pm 0.6^\circ$	$71.3^\circ \pm 1.4^\circ$
PDMS/p-CNT 0.5wt%	$114.6^\circ \pm 0.5^\circ$	$107.8^\circ \pm 1.0^\circ$	$74.5^\circ \pm 0.9^\circ$
PDMS/p-CNT-THF 1wt%	$116.6^\circ \pm 0.3^\circ$	$12.0^\circ \pm 0.5^\circ$	$80.5^\circ \pm 1.7^\circ$
PDMS/f-CNT-THF 1wt%	$125.6^\circ \pm 0.4^\circ$	$118.6^\circ \pm 0.9^\circ$	$92.3^\circ \pm 1.5^\circ$
After 30 minute degradation assay with citrate buffer in dynamic conditions			
Sample	Water	Formamide	1-Bromonaphthalene
PDMS (Control)	$115.4^\circ \pm 3.0^\circ$	$105.0^\circ \pm 2.4^\circ$	$86.1^\circ \pm 1.4^\circ$
PDMS/p-CNT	$121.2^\circ \pm 2.3^\circ$	$119.8^\circ \pm 2.9^\circ$	$98.7^\circ \pm 1.8^\circ$
PDMS/f-CNT	$121.2^\circ \pm 1.9^\circ$	$114.9^\circ \pm 2.9^\circ$	$90.3^\circ \pm 5.0^\circ$

Adhesion Energy Calculations

Table D.2: Surface tension of the liquids used for the CA measurements [9].

Liquid	γ_L^{TOT}	γ_L^{LW}	γ_L^+	γ_L^-
Water	72.8	21.8	25.5	25.5
1-Bromonaphthalene	44.4	44.4	0	0
Formamide	58	39	2.28	39.6

Table D.3: Calculations of surface energies of *E. Coli* in the various coating surfaces (0.1% wt of CNT).

Support	γ_{sb}^{LW}	γ_{sb}^{AB}	γ^{sb}	γ_{bw}^{LW}	γ_{sw}^{LW}	γ_{sw}^{AB}	γ^{sw}
PDMS (Control)	6.912	8.022	14.934	2.046	1.437	29.420	30.857
PDMS/p-CNT 0.1wt%	4,772 9,593	14,366	2,046		0,569	39,604	40,173
PDMS/f-CNT 0.1wt%	6.469	7.337	13.806	2.046	1.239	24.979	26.218
PDMS/p-CNT 1wt%	4.880	8.918	13.799	2.046	0.607	35.229	35.836
PDMS/f-CNT 1wt%	3.983	8.655	12.637	2.046	0.320	33.522	33.841
PDMS/p-CNT-BM 1wt%	7.278	9.179	16.457	2.046	1.606	36.922	38.528
PDMS/f-CNT-BM 1wt%	2.889	8.228	11.116	2.046	0.073	30.753	30.826
After 30 minute degradation assay with citrate buffer in dynamic conditions							
PDMS (Control)	6.450	9.421	15.871	2.046	1.231	38.487	39.718
PDMS/p-CNT 0.1wt%	10.695	8.580	19.275	2.046	3.386	33.038	36.424
PDMS/f-CNT 0.1wt%	7.768	9.234	17.001	2.046	1.841	37.274	39.115

Table D.4: Adhesion Energy of the various coatings with *E. coli*.

Support	γ^{LW}	γ^+	γ^-	γ^{AB}	γ^{tot}
PDMS	12.043	0.000	5.566	0.000	12.043
PDMS/p-CNT 0.1%wt	15.325	0,000	1.273	0.000	15.325
PDMS/f-CNT 0.1%wt	12.645	0.000	6.638	0.000	12.645
PDMS/p-CNT 1%wt	15.1332	0	2.4384	0.0000	15.1332
PDMS/f-CNT 1%wt	16.840	0.000	2.995	0.000	16.840
PDMS/p-CNT-BM 1%wt	11.571	0.000	1.943	0.000	11.571
PDMS/f-CNT-BM 1%wt	19.358	0.000	4.019	0.000	19.358
After 30 minute degradation assay with citrate buffer in dynamic conditions					
PDMS	12.0428	0.000	3.4993	0.000	12.0428
PDMS/p-CNT 0.1%wt	3.6938	13.3894	0.000	0.000	3.6938
PDMS/f-CNT 0.1%wt	14.3495	0.000	5.8106	0.000	14.3495
E. Coli	37.202	0.607	53.079	11.351	48.553
Water (22°C)	21.8	25.5	25.5	51	72.8

Appendix E

Spin Coating Theory

Spin coating is a technique commonly used for the formation of thin layers or films with uniform thickness. Typically, flat substrate (made of a metallic, ceramic or plastic material) is placed in the rotating disk of the spin coater and a small puddle of fluid is dispensed in its centre. Then, the substrate is spun at a predetermined angular speed flowing to allow for the fluid to spread over the entire surface due to the centripetal force. The excess mass is usually expelled off the substrate, leaving an uniform thin film on the surface.

In the spin coating process liquid flows radially under the action of the centrifugal force and the excess is ejected off the edge of the substrate. The film continues to thin until pressure effects cause the film to reach an equilibrium thickness or until solvent evaporation causes its viscosity to reach a solid-like nature [132]. The final film thickness will depend on the nature of the material (volatility, viscosity, drying rate, percent solids, surface tension) and amount of deposited mass, on the rotational speed and acceleration, on the duration of spinning, on the nature of the substrate as well as on the ambient temperature and humidity. Generally, higher spinning speeds and times generate thinner films.

Spinning speed is an important factor since it determines the intensity of the centrifugal shear force applied on the fluid as well as the velocity and characteristic turbulence of the air at the interface. Acceleration is yet another important factor in that it determines in part the strain applied to the fluid and therefore the degree of dispersal over surface. The fluid tends to distort around topographical imperfections and grains present in the substrate and this effect tends to be attenuated at larger accelerations. It is important that air flow turbulence are kept constant during the spin process.

Evaporation phenomena occurring during the spin coating process also pay an important contribution to the final film thickness and properties. As the film moves towards the edges of the substrate its viscosity changes with the distance from the centre, which is also affected by air humidity and variations in air flow above the substrate. This leads to non-uniformly distributed of film thickness, with a pile up of fluid formed at the centre. So, film thickness is largely a balance between the force applied to shear the fluid and the drying rate which affects the viscosity. As the moving fluid dries up, its viscosity increases until the applied radial force can no longer move it

Spin Coating Theory

any further.

Repeatability is an important factor when utilizing spin coating, since there are many parameters influencing the final result. Small variations can cause major differences in the coated films.

Two common methods to dispense the fluid into the spin coater are static dispense and dynamic dispense. Static dispense consists in simply depositing small amounts of material near the centre before spinning. Higher viscosity and larger substrates usually require larger amounts of material to ensure full coverage of the substrate.

Dynamic dispense, on the other hand, consists in dispensing the fluid during the spinning process at low speeds (usually about 500 rpm) and then increasing the speed to thin the fluid layer. Common speeds are in the range 1000 - 6000 rpm and spinning times can go from 10 seconds to some minutes. This procedure facilitates wetting of the substrate surface, which results in less waste of material and better spreading of the film, particularly when the fluid or substrate have poor wetting properties and thus avoids the formation of discontinuities in the film.

As the rotating disk is accelerated, the fluid flows along the substrate in a dynamic process that takes a finite amount of time to stabilize, so the spin coating time should be kept higher than this value.

After the film is spun to the desired thickness, it can be subsequently dried without significantly thinning it by decreasing the speed to about 25%. This helps stabilize the coating when removing it. More complex spin coating procedures may require several steps with different speeds and times.

In general, the final film thickness will be inversely proportional to spin speed and spin time, and proportional to the exhaust volume, that is the evaporated fraction. Film uniformity, in turn, will suffer from higher exhausted volumes. Figure E.1 shows an approximation of the dependence between these parameters. These are merely representative since the process parameters vary greatly depending on the materials and substrates used so there are no fixed rules for spin coat processing.

Some technical problems that can occur in the spin process and cause the formed film to have defects are the presence of air bubbles entrapped in the fluid (Figure E.2-(a)), comets (figure E.2-(b)) central circle (Figure E.2-(c)) due to uneven thickness and uncoated areas (Figure E.2-(d))

According to the spin coating model proposed by Meyerhofer [D. Meyerhofer. J. Appl Phys., 49, 3993 (1978).], the film thinning process can be regarded as having two distinct stages. In the first stage film thins only due to radial outflow, with the solvent evaporation being neglected and the solution concentration assumed to be constant. In this scenario, the evolution of film thickness h with time t can be expressed in terms of the spin coating parameters according to the following relation:

$$\frac{dh}{dt} = -\frac{2\rho w^2 h^3}{3\eta_0} \quad (\text{E.1})$$

where ρ is the fluid density, w is the spin speed and η_0 is the initial solution viscosity.

Spin Coating Theory

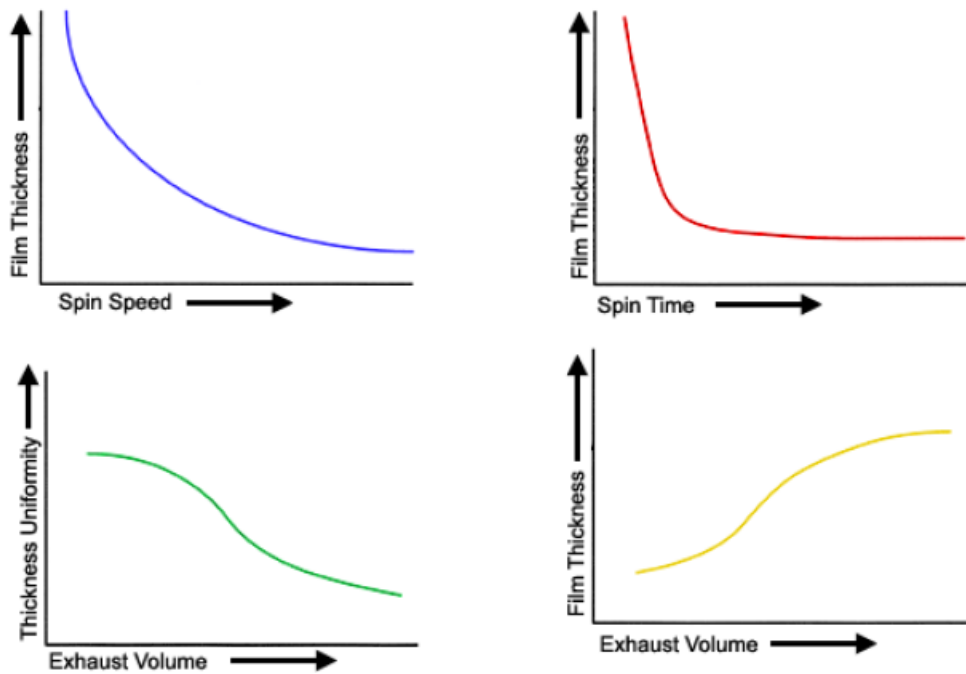


Figure E.1: Graphical representation of the dependence of the final film thickness on three spin coating parameters: spin speed, spin time and exhaust volume and of the film uniformity on exhaust volume. Reprinted from [Spin coat theory].

In the second stage the evaporation rate becomes larger than a certain value E and the fluid becomes immobile and any further thinning of the film is essentially due to solvent evaporation. Bornside *et al.* [D. E. Bornside, C. W. Macosko, and L. E. Scriven, J. Electrochem Soc., 138, 317 (1991)] proposed a mass transfer model to calculate E : [132]

$$E = k(x_l^0 - x_l^\infty) \quad (\text{E.2})$$

where x_l^0 is the initial solvent mass fraction, x_l^∞ is the equilibrium mass fraction and k is the mass transfer coefficient, calculated as:

$$k = \left(\frac{c D_g}{\nu_g^{1/2} \rho} \right) \left(\frac{p_l^0 M_l}{RT} \right) w^{1/2} \quad (\text{E.3})$$

with c being a constant that depends on the Schmidt number of the gas phase; D_g the binary diffusivity of the solvent in the gas phase; ν_g the kinematic viscosity of the gas phase; p_l^0 the vapour pressure of the pure solvent at temperature T ; M_l the solvent molecular weight and R the ideal gas constant. Combining equations E.2 and E.3 gives the thickness at which the film becomes immobile (h_w) [132]:

Spin Coating Theory

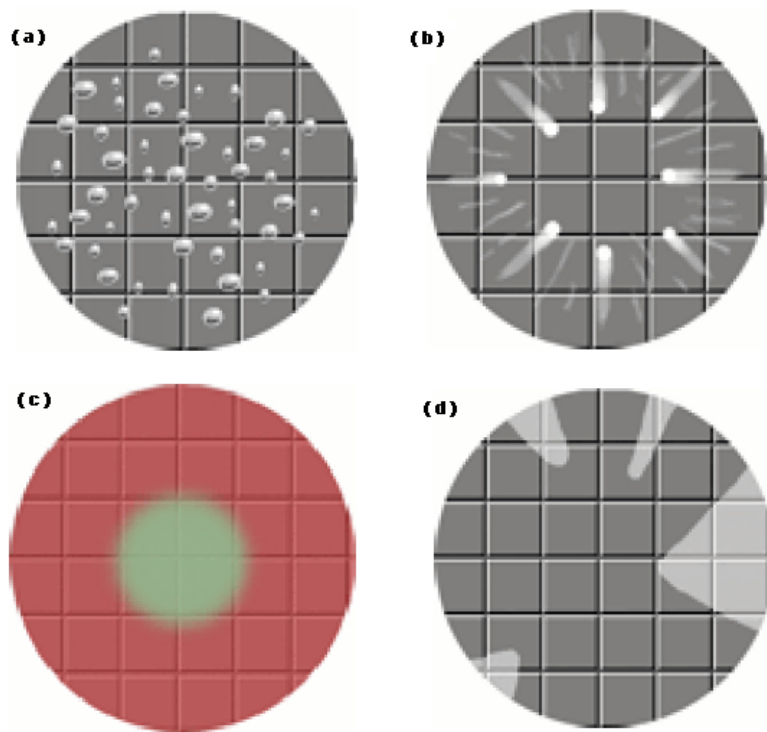


Figure E.2: Schematic representation of some of the issues commonly found in spin coating: (a) bubbles entrapped inside the film; (b) comets caused by particles and impurities deposited on the surface; (c) central circle result from an accumulation of non-dispersed mass; (d) uncoated areas resulting from insufficient dispensed mass or high viscosity. Reprinted from [Spin coat theory].

$$h_w = \left[\left(\frac{3\eta_0}{2\rho w^2} \right) k (x_l^0 - x_l^{\text{inf}}) \right]^{1/3} \quad (\text{E.4})$$

And the final film thickness was then determined to be:

$$h_f = (1 - x_l^0) h_w \quad (\text{E.5})$$

Other more complex models have been proposed that take into consideration the solvent evaporation effects during the first stage and thus alter the film's final thickness.

It has been suggested that spin coating is able to imprint some extent of alignment to the CNTs due to the shear forces generated within the film due to velocity gradients. In the authors prepared a MWCNT/polystyrene composite through solvent casting and spin coating to produce thin films of composite and observed a differential mechanical and electric behaviour of the in the radial and random directions [47]. The velocity gradient as a function of film height and radial distance can be described through the shear stress and viscosity model. This model makes the following assumptions [47]:

1. The fluid is incompressible and non-newtonian:

$$\tau_{rz} = \eta \dot{\gamma} \quad (\text{E.6})$$

2. Gravitational effects are negligible comparing to the centrifugal forces.
3. The system can be considered to be 2π periodic, thus only dependent on the radius.

where τ_{rz} is the radial component of shear stress and $\dot{\gamma}$ the shear rate.

From the classical formula of the centrifugal acceleration $a_c = \omega^2 r$, the centrifugal force acting on a CNT or a bundle is proportional to the radius of rotation, so the CNTs closer to the outer border of the rotating support will be more ejected out of the fluid than the ones near the centre. This results in a less uniform distribution of the CNTs in the coatings. Moreover, the final thickness profile of the coatings is not entirely uniform as can be observed through visual inspection of the films, which present a darkened area in the center due to an excess accumulation of material in this zone.

Spin Coating Theory

Appendix F

Theory of Temperature Programmed Desorption

This appendix gives some insight into the theory of the Temperature Programmed Desorption used for the characterization of the chemical groups at the surfaces of the CNTs prepared by chemical functionalization and heat treatments, as discussed in chapter 4. The calculations of the total desorbed mass were based on the equations presented below.

Temperature Programmed Desorption (TPD) is an experimental technique used to determine the kinetic and thermodynamic parameters of desorption processes or decomposition reactions occurring at the a material's surface. The basic principle is heating a sample under ultra-high vacuum conditions with a temperature program $\beta(t) = dT/dt$, where the temperature is usually a linear function of time, while measuring the partial pressures of the atoms and molecules evolving from the sample by mass spectroscopy, which senses the mass to charge ratio (m/z) of the molecule. TPD gives information on the energy required for each respective molecule to desorb and the relative coverage and activation energies of the desorbing species. As the temperature is increased the molecules adsorbed at the surface, either by chemisorption or physisorption, are successively desorbed with a probability distribution described by the Maxwell-Boltzmann distribution [133].

$$P(a) = \frac{1}{Z_c} e^{-\frac{E}{kT}} \quad (\text{F.1})$$

where

$$Z_c = \int g(E) e^{-\frac{E}{kT}} dE \quad (\text{F.2})$$

The gas pressure p required for equilibrium between adsorption and desorption phenomena is temperature dependent and can be calculated through Clausius-Clapeyron equation. This equation is based on the notion of a surface coverage equilibrium, which is assumed to be a constant ratio ϕ

Theory of Temperature Programmed Desorption

between the number N_{ads} of adsorbed particles and the number N_{surf} of adsorption sites available at the surface, resulting heat the condition for chemical equilibrium between adsorbate and gas phase particles is the equality of the chemical potentials of the particles in both phases: $d\mu_{gas} = d\mu_{ads}$. The *equilibrium heat of adsorption*, q_{eq} is the heat required for a constant pressure ϕ at the surface, and is related to enthalpy according to $q_{eq} = (\frac{\partial}{\partial \phi} \tau)$ and to the pressure according to : $(\partial \ln \frac{p}{\partial T} \phi = q_{eq}/RT^2)$ [134]. Therefore, one gets:

$$q_{eq}(\phi) = \int_0^\phi dH_\tau(\phi') d\phi' \quad (F.3)$$

TPD technique is a common technique for characterizing the oxygen-containing groups on the surface of carbon materials [106] and has been used here to characterize to determine amounts of chemical groups at the surfaces of the various CNTs samples. With the nitric acid functionalization treatment, acidic groups are covalently the appearance of CO and CO₂ peaks in the mass spectrometry spectrum [artigo prof].

The CO and CO₂ signals can be corrected by extracting

$$m_{gas}^{corr} = m_{gas}^{exp} - R \cdot m_{gas} \quad (F.4)$$

$$= m_{gas}^{exp} - R[m_{gas} - m_{gas}^{exp} bl_{gas}] \quad (F.5)$$

Where m_{gas}^{exp} is the experimentally obtained signal of the gas being monitored; m_{gas}^{corr} is the corrected signal; and bl_{gas} is the baseline of the signal.

The amount of released CO, CO-28, in $\mu g^{-1}s^{-1}$ can be determined as:

$$m_{CO} = [m_{CO}^{corr} - bl_{CO}] k_{CO} \left(\frac{1}{V_m} \right) \left(\frac{T^{ref}}{T_{loop}} \right) \left(\frac{1}{m_{sample}} \right) \quad (F.6)$$

where bl_{CO} is te baseline of the os the CO-28 peaks; $T^{[ref]}$ is the reference temperature and is equal to 0°C; V_m is the molar volume of the calibration gas (either CO or CO₂); T_{loop} is the measured temperature inside the loop (35°C); m_{sample} is the mass of the sample and k_{CO-28} is the calibration parameter and is calculated as:

$$k_{CO} = \left(\frac{V_{loop}}{A_{CO}} \right) \quad (F.7)$$

where V_{loop} is the volume inside the calibration loop (64μL) and A_{CO-28} is the integrated area of each peak.

Similarly, the amount of released CO₂ follows the same reasoning:

$$m_{CO_2} = [m_{CO_2}^{corr} - bl_{CO_2}] k_{CO_2} \left(\frac{1}{V_m} \right) \left(\frac{T^{ref}}{T_{loop}} \right) \left(\frac{1}{m_{sample}} \right) \quad (F.8)$$

Theory of Temperature Programmed Desorption

where k_{CO_2} is the calibration constant calculated as:

$$k_{CO_2} = \left(\frac{V_{loop}}{A_{CO_2}} \right) \quad (F.9)$$

The amounts of CO and CO₂ gases released from the samples are determined from the area under the curve of the partial pressure as a function of temperature.

$$A_{peak} = \int Q dT = \int (kP_p - bl) dT \quad (F.10)$$

with k in $\mu L torr^{-1}s^{-1}$. So,

$$Q_{CO} = A_{CO} (\mu mol^{\circ}Cs^{-1}g^{-1}) 60(smin^{-1}) \left(\frac{1}{5} \right) (min/{\circ}C) \quad (F.11)$$

And conversely,

$$Q_{CO_2} = A_{CO_2} (\mu mol^{\circ}Cs^{-1}g^{-1}) 60(smin^{-1}) \left(\frac{1}{5} \right) (min/{\circ}C) \quad (F.12)$$

The percentage of oxygen (%mO) present in the superficial chemical groups emitted from the nanotubes, assuming that all the oxygen gas is released as CO or CO₂ components is then calculated according to:

$$\%m_O = 3 \cdot 16 \cdot 10^{-6} \cdot 100 \quad (F.13)$$

Theory of Temperature Programmed Desorption

References

- [1] Sumio Iijima. Carbon nanotubes: past, present, and future. *Physica B: Condensed Matter*, 323(1–4):1 – 5, 2002. Proceedings of the Tsukuba Symposium on Carbon Nanotube in Commemoration of the 10th Anniversary of its Discovery.
- [2] Erik T Thostenson, Zhifeng Ren, and Tsu-Wei Chou. Advances in the science and technology of carbon nanotubes and their composites: a review. *Composites Science and Technology*, 61(13):1899 – 1912, 2001.
- [3] Pavel Nikolaev Hongjie Dai Pierre Petit Jerome Robert Chunhui Xu Young Hee Lee Seong Gon Kim Andrew G. Rinzler Daniel T. Colbert Gustavo E. Scuseria David Tománek John E. Fischer Richard E. Smalley Andreas Thess, Roland Lee. Crystalline ropes of metallic carbon nanotubes. *Applied Physics Letters*, 26(5274):483–487, 1996.
- [4] Buddy D. Ratner, Allan Hoffman, Frederick J. Schoen, and Jack E. Lemons. *Biomaterials Science, An Introduction to Materials in Medicine*. Elsevier Academic Press, Second edition, 2004.
- [5] Venkata K.K. Upadhyayula and Venkataramana Gadhamshetty. Appreciating the role of carbon nanotube composites in preventing biofouling and promoting biofilms on material surfaces in environmental engineering: A review. *Biotechnology Advances*, 28(6):802 – 816, 2010.
- [6] Hans-Jürgen Butt, Karlheinz Graf, and Michael Kappl. *Contact Angle Phenomena and Wetting*. Wiley-VCH Verlag GmbH & Co. KGaA, 2004.
- [7] Rommel G. Bacabac, Theo H. Smit, Stephen C. Cowin, Jack J.W.A. Van Loon, Frans T.M. Nieuwstadt, Rob Heethaar, and Jenneke Klein-Nulend. Dynamic shear stress in parallel-plate flow chambers. *Journal of Biomechanics*, 38(1):159 – 167, 2005.
- [8] José Luís Figueiredo and Manuel Fernando R. Pereira. The role of surface chemistry in catalysis with carbons. *Catalysis Today*, 150(1–2):2 – 7, 2010. Carbon for Catalysis: CarboCat-III Symposium, Berlin, Germany, 2008.
- [9] Lúcia Chaves. Estudo da cinética de formação de biofilmes em superfícies em contacto com água potável, available at <http://hdl.handle.net/1822/925>. Universidade do Minho, 2004.
- [10] Peter J. F. Harris. *Carbon Nanotubes and Related Structures. New Materials for the twenty-first century*. Cambridge University Press, available at <http://dx.doi.org/10.1017/CBO9780511605819>, Second edition, 1999.

REFERENCES

- [11] Wenrong Yang, Pall Thordarson, J. Justin Gooding, Simon P Ringer, and Filip Braet. Carbon nanotubes for biological and biomedical applications. *Nanotechnology*, 18:412001 – 412013, 2007.
- [12] Zdenko Spitalsky, Dimitrios Tasis, Konstantinos Papagelis, and Costas Galiotis. Carbon nanotube–polymer composites: Chemistry, processing, mechanical and electrical properties. *Progress in Polymer Science*, 35(3):357 – 401, 2010.
- [13] N. Sinha and J. T W Yeow. Carbon nanotubes for biomedical applications. *NanoBioscience, IEEE Transactions on*, 4(2):180–195, 2005.
- [14] Alberto Bianco, Kostas Kostarelos, Charalambos D. Partidos, and Maurizio Prato. Biomedical applications of functionalised carbon nanotubes. *Chem. Commun.*, 0:571–577, 2005.
- [15] Rüdiger Klingeler and Robert B. (Eds.) Sim. *Carbon Nanotubes for Biomedical Applications*. Springer, 2011.
- [16] Ado Jorio, Gene Dresselhaus, Dresselhaus, and Mildred S. *Carbon Nanotubes: Advanced Topics in the Synthesis, Structure, Properties and Applications*. Springer, available at <http://www.springer.com/materials/nanotechnology/book/978-3-540-72864-1>, Second edition, 2008.
- [17] S Iijima, C Brabec, A Maiti, and J Bernholc. Structural flexibility of carbon nanotubes. *JOURNAL OF CHEMICAL PHYSICS*, 104(5):2089–2092, 1996.
- [18] O. Lourie and H. D. Wagner. Evaluation of young’s modulus of carbon nanotubes by micro-raman spectroscopy. *Journal of Materials Research*, 13:2418–2422, 8 1998.
- [19] T.P. Chua, M. Mariatti, A. Azizan, and A.A. Rashid. Effects of surface-functionalized multi-walled carbon nanotubes on the properties of poly(dimethyl siloxane) nanocomposites. *Composites Science and Technology*, 70(4):671 – 677, 2010.
- [20] You Zeng, Pengfei Liu, Jinhong Du, Long Zhao, Pulickel M. Ajayan, and Hui-Ming Cheng. Increasing the electrical conductivity of carbon nanotube/polymer composites by using weak nanotube–polymer interactions. *Carbon*, 48(12):3551 – 3558, 2010.
- [21] B. Chen, M. Gao, J. M. Zuo, S. Qu, B. Liu, and Y. Huang. Binding energy of parallel carbon nanotubes. *Applied Physics Letters*, 83(17):3570–3571, 2003.
- [22] Michael J. O’Connell, Sergei M. Bachilo, Chad B. Huffman, Valerie C. Moore, Michael S. Strano, Erik H. Haroz, Kristy L. Rialon, Peter J. Boul, William H. Noon, Carter Kittrell, Jianpeng Ma, Robert H. Hauge, R. Bruce Weisman, and Richard E. Smalley. Band gap fluorescence from individual single-walled carbon nanotubes. *Science*, 297(5581):593– 596, 2002.
- [23] Jinho Hong, Jeongwoo Lee, Chang Kook Hong, and Sang Eun Shim. Effect of dispersion state of carbon nanotube on the thermal conductivity of poly(dimethyl siloxane) composites. *Current Applied Physics*, 10(1):359 – 363, 2010.
- [24] Xing Chen, Un Chong Tam, Jennifer L. Czapinski, Goo Soo Lee, David Rabuka, Alex Zettl, and Carolyn R. Bertozzi. Interfacing carbon nanotubes with living cells. *Journal of the American Chemical Society*, 128(19):6292–6293, 2006.

REFERENCES

- [25] Aneta Fraczek, Elzbieta Menaszek, Czeslawa Paluszkiewicz, and Marta Blazewicz. Comparative in vivo biocompatibility study of single- and multi-wall carbon nanotubes. *Acta Biomaterialia*, 4(6):1593 – 1602, 2008.
- [26] Jayachandran Venkatesan, Zhong-Ji Qian, BoMi Ryu, Nanjundan Ashok Kumar, and Se-Kwon Kim. Preparation and characterization of carbon nanotube-grafted-chitosan – natural hydroxyapatite composite for bone tissue engineering. *Carbohydrate Polymers*, 83(2):569 – 577, 2011.
- [27] Carbon nanotube applications for tissue engineering. *Biomaterials*, 28(2):344 – 353, 2007. Cellular and Molecular Biology Techniques for Biomaterials Evaluation.
- [28] Ander Abarrategi, María C. Gutiérrez, Carolina Moreno-Vicente, María J. Hortigüela, Viviana Ramos, José L. López-Lacomba, María L. Ferrer, and Francisco del Monte. Multiwall carbon nanotube scaffolds for tissue engineering purposes. *Biomaterials*, 29(1):94 – 102, 2008.
- [29] Li Buay Koh, Isabel Rodriguez, and Subbu S. Venkatraman. A novel nanostructured poly(lactic-co-glycolic-acid)-multi-walled carbon nanotube composite for blood-contacting applications: Thrombogenicity studies. *Acta Biomaterialia*, 5(9):3411 – 3422, 2009.
- [30] Lara Lacerda, Julie Russier, Giorgia Pastorin, M. Antonia Herrero, Enrica Venturelli, Hélène Dumortier, Khuloud T. Al-Jamal, Maurizio Prato, Kostas Kostarelos, and Alberto Bianco. Translocation mechanisms of chemically functionalised carbon nanotubes across plasma membranes. *Biomaterials*, 33(11):3334 – 3343, 2012.
- [31] L. William Luria. The role of medical grade silicones in surgery and its topical applications. *Operative Techniques in Plastic and Reconstructive Surgery*, 9(2):67 – 74, 2002.
- [32] Estelle M. Philips and Derek S. Pugh. *Silicone biomaterials history and chemistry and medical applications of silicones citation*. Elsevier Science, available at www.books.elsevier.com/bioengineering, Second edition, 2004.
- [33] T. S. Radhakrishnan. Thermal degradation of poly(dimethylsilylene) and poly(tetramethyldisilylene-co-styrene). *Journal of Applied Polymer Science*, 99(5):2679–2686, 2006.
- [34] Dow Corning. An overview of polydimethylsiloxane (pdms) fluids in the environment. Health Environment & Regulatory Affairs (HERA), <http://www.dowcorning.com/content/publishedlit/01-1034A-01.pdf>, 1997.
- [35] Eva F.C. Griessbach and R.G. Lehmann. Degradation of polydimethylsiloxane fluids in the environment — a review. *Chemosphere*, 38(6):1461 – 1468, 1999. Degradation Processes in the Environment.
- [36] Tae Ann Kim, Hee Suk Kim, Sang Soo Lee, and Min Park. Single-walled carbon nanotube/silicone rubber composites for compliant electrodes. *Carbon*, 50(2):444 – 449, 2012.
- [37] Song Liu and Xuefeng Guo. Carbon nanomaterials field-effect-transistor-based biosensors. *NPG Asia Materials*, 4:e23, 2012.

REFERENCES

- [38] Won Bong Choi, Eunju Bae, Donghun Kang, Soodoo Chae, Byung ho Cheong, Ju hye Ko, Eungmin Lee, and Wanjun Park. Aligned carbon nanotubes for nanoelectronics. *Nanotechnology*, 15(10):S512, 2004.
- [39] Christofer Hierold, Alain Jungen, Christoph Stampfer, and Thomas Helbling. Nano electromechanical sensors based on carbon nanotubes. *Sensors and Actuators A: Physical*, 136(1):51 – 61, 2007. 25th Anniversary of Sensors and Actuators A: Physical.
- [40] B. Mahar, C. Laslau, R. Yip, and Yu Sun. Development of carbon nanotube-based sensors —: A review. *Sensors Journal, IEEE*, 7(2):266–284, 2007.
- [41] S. T. Knauert, J. F. Douglas, and F. W. Starr. The effect of nanoparticle shape on polymer-nanocomposite rheology and tensile strength. *Journal of Polymer Science B Polymer Physics*, 45:1882–1897, July 2007.
- [42] Taehyung Kim and Hyungsu Kim. Effect of acid-treated carbon nanotube and amine-terminated polydimethylsiloxane on the rheological properties of polydimethylsiloxane/-carbon nanotube composite system. *Korea-Australia Rheology Journal*, 22(3):205 – 210, 2010.
- [43] Linda Vaisman, H. Daniel Wagner, and Gad Marom. The role of surfactants in dispersion of carbon nanotubes. *Advances in Colloid and Interface Science*, 128–130(0):37 – 46, 2006. In Honor of Professor Nissim Garti’s 60th Birthday.
- [44] R. Haggenmueller. Aligned single-wall carbon nanotubes in composites by melt processing methods. *Chemical Physics Letters*, 330:219–225, November 2000.
- [45] Tao Chen Huisheng Peng, Xuemei Sun. Polymer composites with carbon nanotubes in alignment, 2011-08-17.
- [46] L. Jin, C. Bower, and O. Zhou. Alignment of carbon nanotubes in a polymer matrix by mechanical stretching. *Applied Physics Letters*, 73(9):1197–1199, 1998.
- [47] B. Safadi, R. Andrews, and E. A. Grulke. Multiwalled carbon nanotube polymer composites: Synthesis and characterization of thin films. *Journal of Applied Polymer Science*, 84(14):2660–2669, 2002.
- [48] Brian W. Steinert and Derrick R. Dean. Magnetic field alignment and electrical properties of solution cast pet–carbon nanotube composite films. *Polymer*, 50(3):898 – 904, 2009.
- [49] T. Kimura, H. Ago, M. Tobita, S. Ohshima, M. Kyotani, and M. Yumura. Polymer composites of carbon nanotubes aligned by a magnetic field. *Advanced Materials*, 14(19):1380–1383, 2002.
- [50] M. Sagnes, J.-M. Broto, B. Raquet, T. Ondarçuhu, C. Laurent, E. Flahaut, C. Vieu, and F. Carcenac. Alignment and nano-connections of isolated carbon nanotubes. *Microelectronic Engineering*, 67–68(0):683 – 689, 2003.
- [51] Steve Tung, Husein Rokadia, and Wen J. Li. A micro shear stress sensor based on laterally aligned carbon nanotubes. *Sensors and Actuators A: Physical*, 133(2):431 – 438, 2007.
- [52] Xiao-Lin Xie, Yiu-Wing Mai, and Xing-Ping Zhou. Dispersion and alignment of carbon nanotubes in polymer matrix: A review. *Materials Science and Engineering: R: Reports*, 49(4):89 – 112, 2005.

REFERENCES

- [53] D. Qian, E. C. Dickey, R. Andrews, and T. Rantell. Load transfer and deformation mechanisms in carbon nanotube-polystyrene composites. *Applied Physics Letters*, 76(20):2868–2870, 2000.
- [54] Milo S. P. Shaffer and Alan H. Windle. Fabrication and characterization of carbon nanotube/poly(vinyl alcohol) composites. *Advanced Materials*, 11(11):937–941, 1999.
- [55] J. Paul, S. Sindhu, M. H. Nurmawati, and S. Valiyaveettil. Mechanics of pre-stressed polydimethylsiloxane-carbon nanotube composite. *Applied Physics Letters*, 89(18):184101, 2006.
- [56] Taehyung Kim and Kim Hyungsu. Effect of acid-treated carbon nanotube and amine-terminated polydimethylsiloxane on the rheological properties of polydimethylsiloxane-/carbon nanotube composite system. 22(3):205 – 210, September 2010.
- [57] C. H. Hu, C. H. Liu, L. Z. Chen, and S. S. Fan. Semiconductor behaviors of low loading multiwall carbon nanotube/poly(dimethylsiloxane) composites. *Applied Physics Letters*, 95(10):103103, 2009.
- [58] Jung-Bae Lee and Dahl-Young Khang. Electrical and mechanical characterization of stretchable multi-walled carbon nanotubes/polydimethylsiloxane elastomeric composite conductors. *Composites Science and Technology*, 72(11):1257 – 1263, 2012.
- [59] A. Khosla and B.L. Gray. Preparation, characterization and micromolding of multi-walled carbon nanotube polydimethylsiloxane conducting nanocomposite polymer. *Materials Letters*, 63(13–14):1203 – 1206, 2009.
- [60] Il-Seok Park, Kwang J. Kim, Jae-Do Nam, Joonsoo Lee, and Woosoon Yim. Mechanical, dielectric, and magnetic properties of the silicone elastomer with multi-walled carbon nanotubes as a nanofiller. *Polymer Engineering & Science*, 47(9):1396–1405, 2007.
- [61] Alexandre Beigbeder, Philippe Degee, Sheelagh L. Conlan, Robert J. Mutton, Anthony S. Clare, Michala E. Pettitt, Maureen E. Callow, James A. Callow, and Philippe Dubois. Preparation and characterisation of silicone-based coatings filled with carbon nanotubes and natural sepiolite and their application as marine fouling-release coatings. *Biofouling*, 24(4):291–302, 2008. PMID: 18568667.
- [62] L.J. Romasanta, M.A. Lopez-Manchado, and R. Verdejo. The role of carbon nanotubes in both physical and chemical liquid–solid transition of polydimethylsiloxane. *European Polymer Journal*, 49(6):1373 – 1380, 2013.
- [63] Vincenzo Lordi and Nan Yao. Molecular mechanics of binding in carbon-nanotube–polymer composites. *Journal of Materials Research*, 15:2770–2779, 11 2000.
- [64] Matthew Bratcher, Bonnie Gersten, Helen Ji, and Jimmy Mays. Study in the dispersion of carbon nanotubes. *MRS Proceedings*, 706, 0 2001.
- [65] Shengnan Geng, Peng Wang, and Tianhuai Ding. Impedance characteristics and electrical modelling of multi-walled carbon nanotube/silicone rubber composites. *Composites Science and Technology*, 72(1):36 – 40, 2011.
- [66] GUOXING SUN, ZHENGPING LIU, and GUANGMING CHEN. Dispersion of pristine multi-walled carbon nanotubes in common organic solvents. *Nano*, 05(02):103–109, 2010.

REFERENCES

- [67] Yan Yan Huang and Eugene M. Terentjev. Dispersion of carbon nanotubes: Mixing, sonication, stabilization, and composite properties. *Polymers*, 4(1):275–295, 2012.
- [68] Qinghua Zhang, Sanjay Rastogi, Dajun Chen, Dirk Lippits, and Piet J. Lemstra. Low percolation threshold in single-walled carbon nanotube/high density polyethylene composites prepared by melt processing technique. *Carbon*, 44(4):778 – 785, 2006.
- [69] Wen Hui Duan, Quan Wang, and Frank Collins. Dispersion of carbon nanotubes with sds surfactants: a study from a binding energy perspective. *Chem. Sci.*, 2:1407–1413, 2011.
- [70] Li Ju, Wei Zhang, Xuejun Wang, Jundong Hu, and Yuling Zhang. Aggregation kinetics of sdbs-dispersed carbon nanotubes in different aqueous suspensions. *Colloids and Surfaces A: Physicochemical and Engineering Aspects*, 409(0):159 – 166, 2012.
- [71] E. Lizundia, A. Oleaga, A. Salazar, and J.R. Sarasua. Nano- and microstructural effects on thermal properties of poly (l-lactide)/multi-wall carbon nanotube composites. *Polymer*, 53(12):2412 – 2421, 2012.
- [72] Caroline McClory, Tony McNally, Mark Baxendale, Petra Pötschke, Werner Blau, and Manuel Ruether. Electrical and rheological percolation of pmma/mwcnt nanocomposites as a function of {CNT} geometry and functionality. *European Polymer Journal*, 46(5):854 – 868, 2010.
- [73] Inderpreet Singh, P.K. Bhatnagar, P.C. Mathur, Inderpreet Kaur, L.M. Bharadwaj, and Ravindra Pandey. Optical and electrical characterization of conducting polymer-single walled carbon nanotube composite films. *Carbon*, 46(8):1141 – 1144, 2008.
- [74] Wan-Ying Lin, Yeng-Fong Shih, Ching-Hsuan Lin, Chuan-Chen Lee, and Yi-Hsiuan Yu. The preparation of multi-walled carbon nanotube/poly(lactic acid) composites with excellent conductivity. *Journal of the Taiwan Institute of Chemical Engineers*, 44(3):489 – 496, 2013.
- [75] Yuichi Hazama, Naoki Ainoya, Jun Nakamura, and Akiko Natori. Conductivity and dielectric constant of nanotube/polymer composites. *Phys. Rev. B*, 82:045204, Jul 2010.
- [76] Dietrich Stauffer and Amnon Aharony. *Introduction To Percolation Theory*. London: Taylor & Francis, 1985.
- [77] Nikolaos Bonanos, Polycarpos Pissis, and J. Ross Macdonald. *Impedance Spectroscopy of Dielectrics and Electronic Conductors*. John Wiley & Sons, Inc., 2002.
- [78] J.Ross Macdonald. Impedance spectroscopy. *Annals of Biomedical Engineering*, 20(3):289–305, 1992.
- [79] Chuanlai Xu Yingyue Zhu, Libing Wang. *Carbon Nanotubes - Growth and Applications*. 2011.
- [80] Donghui Zhang, Madhuvanthi A. Kandadai, Jiri Cech, Siegmar Roth, and Seamus A. Curran. Poly(l-lactide) (plla)/multiwalled carbon nanotube (mwcnt) composite: Characterization and biocompatibility evaluation. *The Journal of Physical Chemistry B*, 110(26):12910–12915, 2006.

REFERENCES

- [81] Elby Titus Jose Gracio L. Syam Sundar, Ranjit Hawaldar and Manoj Kumar Singh. *Integrated Biomimetic Carbon Nanotube Composites for Biomedical Applications*. Biomedical Engineering - Technical Applications in Medicine, 2012.
- [82] Cheng Zhu Liao, Kai Li, Hoi Man Wong, Wing Yin Tong, Kelvin Wai Kwok Yeung, and Sie Chin Tjong. Novel polypropylene biocomposites reinforced with carbon nanotubes and hydroxyapatite nanorods for bone replacements. *Materials Science and Engineering: C*, 33(3):1380 – 1388, 2013.
- [83] Monica Mattioli-Belmonte, Giovanni Vozzi, Yudan Whulanza, Maurizia Seggiani, Valentina Fantauzzi, Giovanna Orsini, and Arti Ahluwalia. Tuning polycaprolactone–carbon nanotube composites for bone tissue engineering scaffolds. *Materials Science and Engineering: C*, 32(2):152 – 159, 2012.
- [84] Superb K. Misra, Tahera I. Ansari, Sabeel P. Valappil, Dirk Mohn, Sheryl E. Philip, Wendelin J. Stark, Ipsita Roy, Jonathan C. Knowles, Vehid Salih, and Aldo R. Boccaccini. Poly(3-hydroxybutyrate) multifunctional composite scaffolds for tissue engineering applications. *Biomaterials*, 31(10):2806 – 2815, 2010.
- [85] Rebecca A. MacDonald, Brendan F. Laurenzi, Gunaranjan Viswanathan, Pulickel M. Ajayan, and Jan P. Stegemann. Collagen–carbon nanotube composite materials as scaffolds in tissue engineering. *Journal of Biomedical Materials Research Part A*, 74A(3):489–496, 2005.
- [86] Brock Marrs. Improving the performance of medical implants with carbon nanotubes. UK Center for Applied Energy Research, available at http://www.caer.uky.edu/energeia/PDF/vol19_35.pdf, 2008.
- [87] David A. Stout, Bikramjit Basu, and Thomas J. Webster. Poly(lactic–co–glycolic acid): Carbon nanofiber composites for myocardial tissue engineering applications. *Acta Biomaterialia*, 7(8):3101 – 3112, 2011.
- [88] j. Meng, H. Kong, H. Y. Song, L. Song, C. Y. Wang, and S. S. Xie. Improving the blood compatibility of polyurethane using carbon nanotubes as fillers and its applications to cardiovascular surgery. Wiley InterScience, available at 10.1002/jbm.a.30315, 2004.
- [89] Kerry J. Gilmore, Simon E. Moulton, and Gordon G. Wallace. Incorporation of carbon nanotubes into the biomedical polymer poly(styrene-b-isobutylene-b-styrene). *Carbon*, 45(2):402 – 410, 2007.
- [90] Tsukasa Akasaka and Fumio Watari. Capture of bacteria by flexible carbon nanotubes. *Acta Biomaterialia*, 5(2):607 – 612, 2009.
- [91] Seoktae Kang, Mathieu Pinault, Lisa D. Pfefferle, and Menachem Elimelech. Single-walled carbon nanotubes exhibit strong antimicrobial activity. *Langmuir*, 23(17):8670–8673, 2007.
- [92] L. Renea Arias and Liju Yang. Inactivation of bacterial pathogens by carbon nanotubes in suspensions. *Langmuir*, 25(5):3003–3012, 2009.
- [93] Yu-Fu Young, Hui-Ju Lee, Yi-Shan Shen, Shih-Hao Tseng, Chi-Young Lee, Nyan-Hwa Tai, and Hwan-You Chang. Toxicity mechanism of carbon nanotubes on escherichia coli. *Materials Chemistry and Physics*, 134(1):279 – 286, 2012.

REFERENCES

- [94] Shaobin Liu, Andrew Keong Ng, Rong Xu, Jun Wei, Cher Ming Tan, Yanhui Yang, and Yuan Chen. Antibacterial action of dispersed single-walled carbon nanotubes on escherichia coli and bacillus subtilis investigated by atomic force microscopy. *Nanoscale*, 2:2744–2750, 2010.
- [95] Tsukasa Akasaka, Atsuro Yokoyama, Makoto Matsuoka, Takeshi Hashimoto, Shigeaki Abe, Motohiro Uo, and Fumio Watari. Adhesion of human osteoblast-like cells (saos-2) to carbon nanotube sheets. *Bio-Medical Materials And Engineering*, 19(2-3):147 – 153, 2009.
- [96] Lone Tang, Saju Pillai, Niels Peter Revsbech, Andreas Schramm, Claus Bischoff, and Rikke Louise Meyer. Biofilm retention on surfaces with variable roughness and hydrophobicity. *Biofouling*, 27(1):111–121, 2011. PMID: 21181571.
- [97] S. Giljean, M. Bigerelle, K. Anselme, and H. Haidara. New insights on contact angle/roughness dependence on high surface energy materials. *Applied Surface Science*, 257(22):9631 – 9638, 2011.
- [98] C.N.C Lam, R Wu, D Li, M.L Hair, and A.W Neumann. Study of the advancing and receding contact angles: liquid sorption as a cause of contact angle hysteresis. *Advances in Colloid and Interface Science*, 96(1–3):169 – 191, 2002. A Collection of Papers in Honour of Nikolay Churaev on the Occasion of his 80th Birthday.
- [99] Malcolm E. Schroder. Work of adhesion of a sessile drop to a clean surface. *Journal of Colloid and Interface Science*, 213(2):602 – 605, 1999.
- [100] Hua Wang, Maysam Sodagari, Yajie Chen, Xin He, Bi min Zhang Newby, and Lu-Kwang Ju. Initial bacterial attachment in slow flowing systems: Effects of cell and substrate surface properties. *Colloids and Surfaces B: Biointerfaces*, 87(2):415 – 422, 2011.
- [101] Rolf Bos, Henny C. van der Mei, and Henk J. Busscher. Physico-chemistry of initial microbial adhesive interactions – its mechanisms and methods for study. *FEMS Microbiology Reviews*, 23(2):179–230, 1999.
- [102] Malte Hermansson. The {DLVO} theory in microbial adhesion. *Colloids and Surfaces B: Biointerfaces*, 14(1–4):105 – 119, 1999.
- [103] Hua Wang, Maysam Sodagari, Lu-Kwang Ju, and Bi min Zhang Newby. Effects of shear on initial bacterial attachment in slow flowing systems. *Colloids and Surfaces B: Biointerfaces*, 109(0):32 – 39, 2013.
- [104] M. Salta, J. A. Wharton, P. Stoodley, S. P. Dennington, L. R. Goodes, S. Werwinski, U. Mart, R. J. K. Wood, and K. R. Stokes. Designing biomimetic antifouling surfaces. *Royal Society of London Philosophical Transactions Series A*, 368:4729–4754, September 2010.
- [105] A quantitative method to study co-adhesion of microorganisms in a parallel plate flow chamber. ii: Analysis of the kinetics of co-adhesion. *Journal of Microbiological Methods*, 23(2):169 – 182, 1995.
- [106] Alexandra G. Gonçalves, José L. Figueiredo, José J.M. Órfão, and Manuel F.R. Pereira. Influence of the surface chemistry of multi-walled carbon nanotubes on their activity as ozonation catalysts. *Carbon*, 48(15):4369 – 4381, 2010.

REFERENCES

- [107] Olívia Salomé G. P. Soares, José J. M. Órfão, and Manuel Fernando R. Pereira. Pd-cu and pt-cu catalysts supported on carbon nanotubes for nitrate reduction in water. *Industrial & Engineering Chemistry Research*, 49(16):7183–7192, 2010.
- [108] Emer Lahiff, Chang Y. Ryu, Seamus Curran, Andrew I. Minett, Werner J. Blau, and Pulickel M. Ajayan. Selective positioning and density control of nanotubes within a polymer thin film. *Nano Letters*, 3(10):1333–1337, 2003.
- [109] Emer Lahiff, Rory Leahy, Jonathan N. Coleman, and Werner J. Blau. Physical properties of novel free-standing polymer–nanotube thin films. *Carbon*, 44(8):1525 – 1529, 2006.
- [110] F. Lemos J. L. Figueiredo, F. Ramôa Ribeiro ; colab. J. J. M. Órfão. *Catálise Heterogénea*. Fundação Calouste Gulbenkian, 1989.
- [111] Charles M. Ernest. *Compositional Analysis by Thermogravimetry*. ASTM, available at www.books.elsevier.com/bioengineering, 1988.
- [112] M. P. Sepé. Thermal analysis of polymers. *rafra Review Reports*, 8(11):1–121, 1997.
- [113] Dengke Cai, Andreas Neyer, Rüdiger Kuckuk, and H. Michael Heise. Raman, mid-infrared, near-infrared and ultraviolet–visible spectroscopy of {PDMS} silicone rubber for characterization of polymer optical waveguide materials. *Journal of Molecular Structure*, 976(1–3):274 – 281, 2010. A Collection of Invited Papers in Honour of Professor Austin Barnes on the Occasion of His 65th Birthday and His Retirement as Editor of Journal of Molecular Structure.
- [114] Joana M.R. Moreira, Luciana C. Gomes, José D.P. Araújo, João M. Miranda, Manuel Simões, Luís F. Melo, and Filipe J. Mergulhão. The effect of glucose concentration and shaking conditions on escherichia coli biofilm formation in microtiter plates. *Chemical Engineering Science*, 94(0):192 – 199, 2013.
- [115] J.S. Teodósio, M. Simões, L.F. Melo, and F.J. Mergulhão. Flow cell hydrodynamics and their effects on e. coli biofilm formation under different nutrient conditions and turbulent flow. *Biofouling*, 27(1):1–11, 2011. PMID: 21082456.
- [116] P. Aprikian, G. Interlandi, B. A. Kidd, I. Le Trong, V. Tchesnokova, and O. Yakovenko. The bacterial fimbrial tip acts as a mechanical force sensor. *PLoS biology*, 9(5):274 – 1 – 15, 2011.
- [117] Rafael C. Gonzalez, Richard E. Woods, and Steven L. Eddins. *Digital Image Processing Using MATLAB*. Prentice-Hall, Inc., Upper Saddle River, NJ, USA, 2003.
- [118] William K. Pratt. *Digital Image Processing: PIKS Inside*. John Wiley & Sons, Inc., New York, NY, USA, 3rd edition, 2001.
- [119] Gleb Tcheslavski. Morphological image processing: Gray-scale morphology. Lamar University, available at <http://www.ee.lamar.edu/gleb/dip/10-3%20-%20Morphological%20Image%20Processing.pdf>, 2010.
- [120] Jessamine Ng Lee, Cheolmin Park, and George M. Whitesides. Solvent compatibility of poly(dimethylsiloxane)-based microfluidic devices. *Analytical Chemistry*, 75(23):6544–6554, 2003.

REFERENCES

- [121] Samu Hemmilä, Juan V. Cauich-Rodríguez, Joose Kreutzer, and Pasi Kallio. Rapid, simple, and cost-effective treatments to achieve long-term hydrophilic {PDMS} surfaces. *Applied Surface Science*, 258(24):9864 – 9875, 2012.
- [122] L. Stobinski, B. Lesiak, L. Kövér, J. Tóth, S. Biniak, G. Trykowski, and J. Judek. Multi-wall carbon nanotubes purification and oxidation by nitric acid studied by the {FTIR} and electron spectroscopy methods. *Journal of Alloys and Compounds*, 501(1):77 – 84, 2010.
- [123] A. Solhy, B.F. Machado, J. Beausoleil, Y. Kihn, F. Gonçalves, M.F.R. Pereira, J.J.M. Órfao, J.L. Figueiredo, J.L. Faria, and P. Serp. {MWCNT} activation and its influence on the catalytic performance of pt/mwcnt catalysts for selective hydrogenation. *Carbon*, 46(9):1194 – 1207, 2008.
- [124] Francis M. Mirabella. *Internal Reflection Spectroscopy: Theory and Applications*. Taylor & Francis Group, 1993.
- [125] A.G. Ryabenko, T.V. Dorofeeva, and G.I. Zvereva. Uv-vis-nir spectroscopy study of sensitivity of single-wall carbon nanotubes to chemical processing and van-der-waals swnt/swnt interaction. verification of the {SWNT} content measurements by absorption spectroscopy. *Carbon*, 42(8–9):1523 – 1535, 2004.
- [126] Edson C. Botelho, Elilton R. Edwards, Birgit Bittmann, and Thomas Burkhardt. Dispersing carbon nanotubes in phenolic resin using an aqueous solution. *Journal of the Brazilian Chemical Society*, 22:2040 – 2047, 11 2011.
- [127] Zhiyun Zhang, Jianchun Wang, Qin Tu, Nan Nie, Jun Sha, Wenming Liu, Rui Liu, Yanrong Zhang, and Jinyi Wang. Surface modification of {PDMS} by surface-initiated atom transfer radical polymerization of water-soluble dendronized {PEG} methacrylate. *Colloids and Surfaces B: Biointerfaces*, 88(1):85 – 92, 2011.
- [128] Ana Catarina Lopes, Marco P. Silva, Renato Gonçalves, Manuel F. R. Pereira, Gabriela Botelho, António M. Fonseca, Senenxtu Lanceros-Mendez, and Isabel C. Neves. Enhancement of the dielectric constant and thermal properties of α -poly(vinylidene fluoride)/zeolite nanocomposites. *The Journal of Physical Chemistry C*, 114(34):14446–14452, 2010.
- [129] Ljubisa R. Radovic. *Chemistry & Physics of Carbon Vol. 27*. Taylor & Francis Group, 2000.
- [130] Jacinta C. Conrad. Physics of bacterial near-surface motility using flagella and type {IV} pili: implications for biofilm formation. *Research in Microbiology*, 163(9–10):619 – 629, 2012. <ce:title>Microbial devices for cell-cell and cell-surface interactions</ce:title>.
- [131] Malte Hermansson. The {DLVO} theory in microbial adhesion. *Colloids and Surfaces B: Biointerfaces*, 14(1–4):105 – 119, 1999.
- [132] David B. Hall, Patrick Underhill, and John M. Torkelson. Spin coating of thin and ultrathin polymer films. *Polymer Engineering & Science*, 38(12):2039–2045, 1998.
- [133] Nicholas J. Clark. Design of a temperature programmed desorption system for the measurement of the desorption kinetics of molecules from surfaces, 2009.
- [134] Sven L.M. Schroeder and Michael Gottfried. Temperature-programmed desorption (tpd) thermal desorption spectroscopy (tds). Freie Universität Berlin, available at <http://www.chemie.fu-berlin.de/~pcprakt/tds.pdf>, 2002.